

**ACOUSTIC WAVE PROPAGATION AND NON-INTRUSIVE  
VELOCITY MEASUREMENTS IN HIGHLY  
CONCENTRATED SUSPENSIONS**

by

**Christopher Mark Atkinson**

B.Sc. Chemical Engineering, University of Natal (1983)

M.S.M.E., West Virginia University (1987)

Submitted to the Department of Mechanical Engineering in  
Partial Fulfillment of the Requirements for the Degree of

**DOCTOR OF SCIENCE**

at the

**MASSACHUSETTS INSTITUTE OF TECHNOLOGY**

June, 1991

© Christopher M. Atkinson, 1991. All rights reserved.

The author hereby grants to MIT permission to reproduce and to  
distribute copies of this thesis document in whole or in part.

**Signature redacted**

Signature of Author \_\_\_\_\_

Department of Mechanical Engineering

**Signature redacted**

April, 1991

Certified by \_\_\_\_\_

Professor Harri K. Kytömaa

Thesis Supervisor

**Signature redacted**

Accepted by \_\_\_\_\_

Professor Ain A. Sonin, Chairman

Graduate Committee, Department of Mechanical Engineering  
MASSACHUSETTS INSTITUTE  
OF TECHNOLOGY

JUN 12 1991

LIBRARIES  
ARCHIVES

# Acoustic Wave Propagation and Non-Intrusive Velocity Measurements in Highly Concentrated Suspensions

by

Christopher Mark Atkinson

Submitted to the Department of Mechanical Engineering  
on April 10, 1991 in partial fulfillment of the  
requirements for the Degree of Doctor of Science

## Abstract

Acoustic wave propagation as a technique for interrogating two-phase mixtures has the advantages of being non-intrusive, it has a very high frequency response and is able to penetrate typically opaque highly concentrated mixtures. There exists, however, an inherent compromise in the choice of the frequency of the ultrasound between maximizing spatial resolution and ensuring adequate beam penetration. To this end, the propagation of sound in solid-liquid mixtures has been investigated experimentally and analytically for a range of frequencies and concentrations of the dispersed phase. The attenuation of acoustic waves in a suspension of monodisperse spheres in a viscous fluid has been found to be a non-monotonic function of solids' fraction: for example, there is a maximum in attenuation at a solids' fraction of about 30% for a system of 1 mm silica beads in water. It has been found previously that the acoustic phase speed has a minimum at intermediate concentrations, but this behavior is shown here to be a function of  $ka$ , where the wavenumber  $k = \frac{2\pi}{\lambda}$ , and  $\lambda$  and  $a$  are the wavelength and particle radius respectively, and the dynamic particle Reynolds number  $R = \frac{a}{\delta}$ , where  $\delta$  is the unsteady boundary layer thickness. A two component model that includes viscous, inertial and history effects between the two phases has been developed and it is shown to predict accurately sound speed and attenuation in suspensions for three to four orders of magnitude of  $ka$ . The attenuation of an acoustic wave propagating in a solid-liquid mixture at high frequencies is shown to be proportional to  $(ka)^{3/4}$  for  $\lambda \geq a$  and to be strongly dependent on the suspension microstructure — at 500 kHz in a suspension of 1.0 mm silica particles in

water at the maximum packing concentration, the intensity of an acoustic wave decreases by a factor of  $1/e$  in a distance of approximately 500 particle diameters and thus results in a useful range of penetration of tens of centimeters. The viscous attenuation model is also shown to predict the dynamic permeability of a porous medium made up of monodisperse spheres — the frequency dependence of the permeability has been postulated as a good measure of the geometry of the interstitial pores of such a medium.

The acoustic intensity field produced by a circular disc transducer in a two phase medium at  $ka \sim 1$  is shown to be in excellent agreement with the Rayleigh theory, following the substitution of a modified complex wavenumber which takes into account the attenuation behavior of the medium. This theory allows for the prediction of the transducer beam geometry in an arbitrary attenuating two phase mixture for a wide range of frequencies and solids' fractions. The limitations of ultrasonic wave propagation as a non-intrusive diagnostic technique in terms of spatial resolution, and the advantages of focussed transducers are discussed — with the latter, focal regions of the order of 10 particle diameters on each side are possible. Finally, velocity measurements obtained in highly concentrated particulate suspensions, using an ultrasonic Doppler velocimeter in a sedimenting particulate bed and a Dynamic Shear Cell, are presented. Results of the reflection, scattering and refraction characteristics of highly concentrated solid-liquid mixtures are presented, and their implication for non-intrusive diagnostic instrumentation discussed.

Thesis Supervisor: Dr. Harri K. Kytömaa

Title: Esther and Harold E. Edgerton Assistant Professor  
of Mechanical Engineering.

## TABLE OF CONTENTS

	Acknowledgements . . . . .	7
	Nomenclature . . . . .	8
<b>1</b>	<b>Introduction . . . . .</b>	<b>11</b>
1.1	Background . . . . .	11
1.2	Objectives of this work . . . . .	16
1.3	Thesis structure . . . . .	17
<b>2</b>	<b>Acoustic Wave Propagation in Suspensions — Experiments</b>	<b>18</b>
2.1	The Theory of Linear Acoustics - A Review . . . . .	18
2.2	Acoustic Wave Propagation in an Attenuating Medium . . . . .	19
2.3	Ultrasonic Wave Propagation — Experimental Procedure . . . . .	21
2.3.1	Experimental apparatus . . . . .	21
2.3.2	Transducers . . . . .	22
2.3.3	Transducer alignment . . . . .	22
2.3.4	Transducer operation . . . . .	23
2.4	Experimental Results . . . . .	24
2.4.1	Acoustic field in degassed water . . . . .	24
2.4.2	Acoustic field in packed beds . . . . .	25
2.4.3	Phase velocity in packed beds of glass beads and water . . . . .	26
2.4.4	Comparison with Rayleigh theory . . . . .	27
2.4.5	Attenuation in packed beds . . . . .	28
2.4.6	Experimental error analysis . . . . .	30
2.5	Fluidized Bed Acoustic Experiments . . . . .	30
2.5.1	Sound speed variation with concentration . . . . .	32
2.5.2	Variation of attenuation with concentration . . . . .	32

2.6	The Design of Ultrasonic Instrumentation and the Limitations of the Technique . . . . .	34
2.7	Discussion . . . . .	36
<b>3</b>	<b>Acoustic Wave Propagation in Suspensions — Theory . .</b>	<b>61</b>
3.1	Introduction . . . . .	61
3.2	Measurement of acoustic phase speed and attenuation . . .	63
3.3	Governing equations . . . . .	64
3.3.1	The interaction between the phases . . . . .	66
3.3.2	Drag on an isolated sphere . . . . .	67
3.3.3	The added mass term and its dependence on concentration . . . . .	69
3.3.4	The momentum interaction force . . . . .	70
3.3.5	Linearized equations . . . . .	72
3.4	Dispersion Relation . . . . .	74
3.5	Results . . . . .	75
3.5.1	Sound speed . . . . .	75
3.5.2	Attenuation . . . . .	77
3.6	Discussion . . . . .	78
<b>4</b>	<b>Dynamic Permeability in Porous Media — A Dynamic Drag Approach . . . . .</b>	<b>90</b>
4.1	Introduction . . . . .	90
4.2	Background . . . . .	91
4.3	Governing Equations . . . . .	93
4.3.1	Momentum equation . . . . .	93
4.3.2	The solid-liquid interaction force . . . . .	94
4.3.3	Drag on an isolated sphere . . . . .	94
4.3.4	The added mass term and its dependence on	

	concentration . . . . .	96
4.3.5	The extension of the single particle result to an assembly of particles . . . . .	98
4.4	Dynamic permeability . . . . .	100
4.4.1	General solution . . . . .	100
4.4.2	High frequency permeability . . . . .	102
4.5	Discussion: Comparison to existing models . . . . .	103
<b>5</b>	<b>Ultrasonic Doppler Velocimetry . . . . .</b>	<b>110</b>
5.1	Introduction . . . . .	110
5.2	Theory . . . . .	113
5.2.1	Acoustic reflection, refraction and scattering . . . . .	113
5.2.2	The Doppler frequency shift . . . . .	116
5.3	Experimental Procedure . . . . .	119
5.3.1	The prototype ultrasonic Doppler velocimeter . . . . .	119
5.3.2	Device refinements . . . . .	121
5.3.3	Frequency resolution and signal processing considerations	121
5.4	Experimental Results . . . . .	124
5.4.1	Interface reflection . . . . .	124
5.4.2	Surface velocity measurements . . . . .	125
5.4.3	Scattering and interior velocity measurements . . . . .	126
5.5	Discussion . . . . .	127
<b>6</b>	<b>Conclusions . . . . .</b>	<b>141</b>
	<b>Appendix: Steady and Unsteady Velocity Measurements . . . . .</b>	<b>146</b>
	<b>References . . . . .</b>	<b>150</b>

## ACKNOWLEDGEMENTS

I would like to acknowledge the help, support and guidance of my advisor, Harri Kytömaa, throughout the last four years — Harri, we finally made it. Without the assistance and support of the other members of the Fluid Mechanics Laboratory, past and present, I doubt that I would now be writing this acknowledgement. In particular, Steve Brown, Andy Shapiro, Andrew Poutiatine, Ed Rubesch and Dick Fenner deserve a resounding vote of thanks for all their help and friendship. Thanks are due to Caiti Crawford, Joseph Gomes and Wilson Hu for their help at various stages of the experimental work. Thanks, Leslie.

This thesis is dedicated to Bev and her uncomplaining good-naturedness, love and tolerance — I have asked more of you in the last four years than I should have done. Thanks are not enough.

Finally, this thesis is also dedicated to the memory of my late father, Peter J. Atkinson, who urged me not to be an engineer, as he was, but to be an accountant because, as he used to say, they play plenty of golf and get paid for it. He instilled in me a love for things mechanical and a healthy skepticism. One of my main regrets is that Jeffrey will not hear the same advice from him.

## NOMENCLATURE

$a$	particle radius
$A$	transducer area
$A$	coefficient defined in Equation (3.30)
$B$	coefficient defined in Equation (3.31)
$c$	sound speed
$C$	added mass coefficient
$d$	pore size
$D$	density ratio
$e$	2.71828...
$f$	frequency
$F$	phase interaction force
$G$	parameter defined in Equation (3.35)
$h$	particle separation distance
$H(\omega)$	frequency response transfer function
$i$	$\sqrt{-1}$
$\Im$	imaginary part
$k$	dynamic permeability
$\mathbf{k}$	wavenumber (complex)
$L$	penetration depth or distance
$\mathbf{M}$	perturbation matrix defined in Equation (3.29)
$n$	number density of particles
$n$	refractive index
$N$	number of points
$p$	acoustic pressure
$P$	fluid pressure
$r_H$	hydraulic radius
$R$	radius
$R$	Reynolds number
$\Re$	real part
$s$	distance from transducer face

$S$	distance from center of transducer face
$t$	time
$T$	period
$u$	fluid velocity
$U$	velocity
$v$	velocity
$V$	signal amplitude
$x$	distance
$\mathbf{x}$	position vector
$z$	axial distance
$Z$	acoustic impedance

### Subscripts

$c$	characteristic
$D$	drag
$D$	Doppler
dec	deconvoluted
eff	effective
eq	equivalent
f	fluid
i	incident
l	liquid
max	maximum
min	minimum
0	ambient or static
p	particle
r	refracted
rel	relative
res	resolution
R	receiver
s	solid
s	sound

trans	transmitted
T	transmitter

### Superscripts

$l$	perturbation
0	ambient or undisturbed
$\sim$	dimensionless

### Greek Symbols

$\alpha$	attenuation parameter
$\alpha$	tortuosity
$\beta$	conductivity ratio
$\delta$	boundary layer thickness
$\eta$	normalized solids' fraction
$\kappa$	bulk modulus
$\kappa$	extinction coefficient
$\lambda$	wavelength
$\Lambda$	pore length scale
$\mu$	viscosity
$\nabla$	gradient
$\nu$	solids' volume fraction
$\omega$	frequency
$\phi$	velocity potential
$\pi$	3.14159...
$\psi$	phase
$\rho$	density
$\tau$	time period

# CHAPTER 1

## INTRODUCTION

### 1.1 Background

Multiphase flows, that is those flows in which two or more different physical phases (gaseous, liquid or solid) of the same or several different components co-exist, are encountered in a wide range of chemical and physical processes. Highly concentrated solid-liquid flows, a subset of these multiphase flows, are found in the pipeline transport of mineral and coal slurries, the flow of drilling muds in oil-fields, the flow of pastes in the food and pharmaceutical preparation industries, the flow of concrete in construction applications, sediment transport in rivers and ocean currents, catalytic reactors such as Fischer-Tropsch hydrogenators, composite manufacture and polymer melts, fibrous and filamentaceous broths in bioreactors and fermentors and in paper-making applications, and in solid-fuel handling in rocket propulsion applications (amongst many others).

Flows of such mixtures are often susceptible to blockages and bridging at high solids' loadings, and are typically difficult to monitor and control. At very high solids' concentrations, small variations in pipe geometry or mixture velocity can lead to concentration perturbations that may grow in amplitude, to ultimately cause the mixture to pack or sediment locally. Once this occurs, blockages in the flow system can occur leading to catastrophic damage to pumping equipment. Furthermore, once a flowing slurry or suspension comes to a stop, there is a strong hysteretic effect inasmuch as very high liquid velocities and pumping pressures are then required to resuspend the dispersed phase after sedimentation. These problems have motivated the development of non-intrusive diagnostic

techniques to describe the internal mechanics of these flows and to monitor their behavior. Instrumentation for these flows is necessary for the measurement of the velocity of the flowing mixture (in its simplest form, such measurement may be a flow/no-flow indication), and for the measurement of the concentration of the dispersed or solid phase. Most available instrumentation is intrusive, that is to say that it intrudes into the flow, and thus has the potential to disturb the flow locally. This is somewhat self-defeating as most intrusive instrumentation relies on very local variations or fluctuations in mixture properties as a measurement strategy. Such measurements thus typically interfere with the flow that they are attempting to measure or monitor and raise questions as to their fidelity or accuracy or representability. In addition, abrasion in these flows can lead to problems with instrument longevity and reliability. Non-intrusive instrumentation on the other hand usually relies on some implicit averaging, inasmuch as the flow is usually monitored across some length of the flow geometry or across a pipe cross section. This type of measurement thus implies inaccuracies associated with spatial averaging and less than optimum spatial resolution, but without interfering with the flow under measurement.

The most common and useful measurements in highly concentrated solid-liquid flows are particle and liquid velocity (and hence flowrate), and the concentration of the dispersed phase. The velocity of the moving mixture might be inferred non-intrusively from the pressure drop down a known length of piping or around a bend or through a fitting, or it might be measured at a point using intrusive conductance or resistivity probes such as those described by Shook *et al.*, 1982, or Hsu *et al.*, 1989, which operate on the principle that the resistance or capacitance measured locally in the flowing mixture varies with the local particle concentration and with the passage of discrete solid particles. A more

sophisticated non-intrusive measurement is the relatively recent method of laser Doppler anemometry (LDA) with refractive-index matching. In this laboratory technique, the test liquid and solid particles are chosen with matching (or very nearly so) indices of refraction to allow the light beams to penetrate deep into the mixture to the measuring volume without prohibitively high signal attenuation. This technique has been shown to be effective in slurries with solids' loadings of up to about 50% by volume, (Kadambi, Bhunia and Dybbs, 1988). Gamma ray, X-ray and microwave radiation have also been used in highly concentrated slurry applications (Goldstein, 1983), but the extremely high capital costs and safety concerns associated with the use of these techniques means that their widespread use in industrial and laboratory applications is not feasible.

A remarkably underutilized method of non-intrusive measurement, on the other hand, is acoustic or ultrasonic wave propagation. Ultrasound (typically in the range of tens of kilohertz to several megahertz) has several distinct advantages over other methods of measurement in the investigation of highly concentrated mixtures. It is truly non-intrusive, it has an inherently high frequency response, and can thus be used for the measurement of dynamic or transient phenomena; it can penetrate highly concentrated and optically opaque (and hence physically realistic) mixtures, and it operates at sufficiently high frequencies and hence short wavelengths to afford good spatial resolution. In addition, acoustic instrumentation is comparatively inexpensive to procure and maintain, and robust in its operation.

High frequency acoustic wave propagation has been used for some time in the measurement of predominantly single phase flowrates in such diverse areas as *in vivo* blood flow measurement and water pipeline flow monitoring. Indeed invasive and non-invasive ultrasonic cardiography and angiography are now widely

practiced medical diagnostic techniques (Marcus *et al.*, 1991). These methods typically utilize ultrasound in the range 5-20 MHz and measure Doppler-shifted signals scattered off the platelets in flowing blood.

**Table 1:** Relative Performance of various Non-intrusive Instrumentation Techniques for Highly Concentrated Solid-Liquid Flows.

Representative Performance	X-rays	Visible lasers	Electrical techniques	Acoustic techniques
Wavelengths	$\sim \text{\AA}$	$\sim \mu\text{m}$	—	$\sim \text{mm}$
Source Coherence	no	yes	—	yes
Scattering cross section	medium	large	—	small
Absorption	small	large	—	small
Penetration at high solids' loading	good	poor	—	good
Spatial resolution	poor	good	poor	fair
Tomography	yes	unnecessary	yes	yes
Velocity measurement	no	yes	possible	yes
Fractional Doppler Shift	—	small	—	large
Signal to noise ratio	high	high	fair	fair

(after Penner *et al.*, 1984).

In industrial pipeline applications, several proprietary devices are available that measure fluid velocities in predominantly single phase systems, such as water pipelines (*cf.* Controlotron Corporation, Nusonics, Polysonics and Texas Nuclear); these devices, typically operated at frequencies around 1 MHz (and above), require a low concentration of scatterers such as bubbles or small particles in the flow and are also considered suitable for measurements in suspensions

with low solids' loading, such as those encountered in sewage lines. These devices infer fluid velocity by measuring the Doppler shift in ultrasound scattered off small particles (solids or bubbles) that are assumed to move at the fluid velocity. Ultrasonic Doppler anemometry has also been used in medium concentration two phase mixtures in experimental settings (for a brief review of industrial applications see Lynnworth, 1989). For example, Hilgert and Hofmann (1986) have investigated bubble rise velocities in bubble columns, while intensive testing of Doppler instruments for use in measuring coal slurries has been undertaken in the recent past at Argonne National Laboratories (Karplus and Raptis, 1979; Raptis and Lau, 1981; Raptis, 1984). Beltran *et al.*, 1989, describe the use of such instrumentation for the measurement of slurry velocity in a copper ore grinding circuit up to about 10% by volume concentration.

Acoustic wave propagation as a non-intrusive technique has certainly not been used to its full potential in highly concentrated mixtures, due mainly to the difficulties posed by signal attenuation due to beam spreading, viscous losses, scattering and other mechanisms. There exists an inherent compromise in the selection of operating frequency for an acoustic device between the need to minimize the wavelength for better spatial resolution, while maximizing the wavelength for better penetration of such mixtures. This thesis describes, in part, an experimental investigation of the acoustic characteristics of solid-liquid mixtures. A systematic study of the effect on acoustic propagation of operating frequency, particle concentration, particle properties such as size, density and solid stiffness, and liquid properties such as density and viscosity was carried out. A theoretical model for the acoustic wave speed and attenuation in a two phase mixture of varying solids' concentration, incorporating particle and fluid properties, was developed and compared to the experimental results. Based on the experimental

and analytical findings, the distinct advantages of acoustics as a method of interrogating these mixtures were delineated, and the limitations of the technique discussed. An ultrasonic Doppler flowmeter, capable of measurements of velocities in systems of up to maximum packing concentration, was developed for use in sedimenting and packed mixtures, and shown to be able to measure velocities at considerably higher concentrations than those previously reported.

## 1.2 Objectives of this work

The objectives of this work were to study acoustic wave propagation in highly concentrated mixtures of elastic solid particles in Newtonian fluids, with a view to the development of non-intrusive diagnostic instrumentation for highly concentrated multiphase flows. Specifically, the aims of this work were:

1) to investigate experimentally the intensity field produced by ultrasonic transducers in multiphase systems and to extend the classical Rayleigh theory to predict beam geometry effects in such mixtures for  $\lambda \geq a$ ,

2) to measure linear acoustic wave propagation in mixtures and suspensions, in terms of attenuation and sound speed,

3) to investigate theoretically the frequency and concentration dependence of attenuation and sound speed in highly concentrated mixtures,

and

4) to show the application of non-intrusive measurements in multiphase systems by determining the velocity of particles in a highly concentrated solid-liquid mixture.

### 1.3 Thesis structure

Chapter 2 describes the theory for determining the acoustical intensity field produced by ultrasonic transducers, and shows experimental results of the acoustical beam geometry obtained in single and two phase systems. Experimental results of the sound speed and attenuation in both packed beds and in fluidized beds for a range of solids' concentrations and ultrasonic frequencies are then described. Chapter 3 details the viscous attenuation and sound speed that are derived from a two component model and shows the agreement between predictions and experimental results. As an extension of this model, the dynamic response of a fluid saturating a porous medium of spheres has been modelled. The prediction of the dynamic permeability of a porous medium made up of spheres via a dynamic drag approach is described in Chapter 4. The development of an ultrasonic Doppler velocimeter for use in measuring particle velocities at high mixture concentrations and an analysis of acoustic wave reflection, refraction and scattering in highly concentrated solid-liquid mixtures is described in Chapter 5. Finally, the conclusions and recommendations of this study are detailed in Chapter 6.

**CHAPTER 2**  
**ACOUSTIC WAVE PROPAGATION IN SUSPENSIONS**  
**— EXPERIMENTS**

**2.1 The Theory of Linear Acoustics - A Review**

The experimental study utilizes a flat, unfocussed ultrasonic transducer; it is therefore appropriate to first outline the characteristics of the acoustic field emanating from such a transducer in a pure fluid. A more complete review of the classical theory may be found elsewhere (see, for example, Morse and Ingard, 1978). If a circular planar piston transducer is induced to vibrate, it will cause sound to be radiated into the medium in which it is immersed. All points on the face of the piston act as monopoles oscillating in phase with one another. Away from the piston face, the monopole fields interfere both constructively and destructively. By linear superposition, the velocity potential  $\phi(\mathbf{x}, t)$  at any point in the fluid is given by the Rayleigh integral (Morse and Ingard, 1978):

$$\phi(\mathbf{x}, t) = \int_A u \frac{e^{-iks}}{2\pi s} dA, \quad (2.1)$$

where  $\mathbf{x}$  is the position vector of the target point,  $u$  is the velocity distribution across the face of the transducer,  $s$  is the distance from each point on the face of the transducer to the target,  $k = 2\pi/\lambda$  is the wavenumber,  $\lambda$  is the acoustic wavelength and  $A$  is the area of the emitting surface, as indicated in Figure 2.1. The velocity,  $\mathbf{u}$ , of the fluid at any point is given by  $\mathbf{u} = \nabla\phi$ , where  $\phi$  is the velocity potential. The acoustical pressure deviation from the undisturbed datum,  $p_0$ , is given by  $p' = i\rho_0\omega\phi$ , where  $\rho_0$  is the datum fluid density (Temkin, 1981). The Rayleigh integral has been simplified and evaluated in approximate analytical

forms by numerous investigators (*cf.* Adach and Chivers, 1990; Goodsitt, Madsen and Zagzebski, 1982; Harris, 1981). Here it is integrated numerically and the radially symmetric intensity profile, normalized with respect to the maximum value, is shown in Figure 2.2 for the case  $kR = 40$ , where  $R$  is the transducer radius (the profile shown is actually one-half of the radially symmetric profile). The acoustic field has the following characteristics. The amplitude goes through a number of local maxima and minima in the near-field or Fresnel region while far from the piston face, the amplitude decays monotonically (as  $\frac{1}{\sqrt{r}}$ ). In the intermediate region between the near and far fields, the intensity of the sound wave goes through a final maximum at the point of natural focus of the transducer. The distance from the transducer face to this point is referred to as the natural focal length, in reference to the (analytically) similar case in geometrical optics. In the far-field, the transducer beam intensity is a maximum along its axis and falls off with increasing radial distance from the center axis. The Rayleigh integral is sufficiently general to describe the acoustic field due to a transducer of any geometry oscillating with an arbitrary velocity distribution, as was demonstrated for a focussed transducer by O'Neil (1949).

## 2.2 Acoustic Wave Propagation in an Attenuating Medium

In an attenuating medium, the wavenumber of a propagating acoustic wave,  $\mathbf{k}$ , is generally complex and involves the angular frequency of oscillation,  $\omega$ , the sound speed,  $c$ , and the frequency dependent attenuation parameter,  $\alpha(\omega)$ , which is unique to the medium concerned,

$$\mathbf{k} = \frac{\omega}{c} - i\alpha(\omega) = k - i\alpha(\omega). \quad (2.2)$$

Several theories exist that relate  $\alpha(\omega)$  to fluid and particle properties, the particle concentration and the frequency of excitation, and a comprehensive review of these theories for the attenuation of sound in suspensions has been given by Harker and Temple (1988). The acoustic field for a linearly attenuating medium can be readily computed with the Rayleigh integral, with the substitution of a modified wavenumber to take into account differences in sound speed and attenuation. With reference to Figure 2.1, for all points sufficiently far from the emitting surface such that  $S \gg R$ , where  $S$  is the distance from the center of the transducer face, it follows that  $s \simeq S$ . For these conditions, the purely geometrical effect of the integration over the transducer face may be uncoupled from the attenuation term to give the resultant velocity potential as

$$\phi(\mathbf{x}) \simeq e^{-\alpha S} \int_A u \frac{e^{-iks}}{2\pi s} dA \quad (2.3)$$

The condition  $S \gg R$  is not particularly restrictive when it is considered that the transition to the far-field of an unfocussed transducer typically occurs at a distance of several times the transducer radius, and that intensity measurements are typically performed in the far-field. Thus by measuring the velocity potential distribution in an attenuating medium, the attenuation parameter for that fluid can be calculated.

Considering a non-homogeneous multiphase system consisting of discrete solid particles suspended in a fluid, for the case in which the wavelength of the sound is much larger than the particle radius, or  $\lambda \gg a$ , the behavior of the medium is known to become attenuative and to assume the above representation with a modified wave speed (Allegra and Hawley, 1972, and Waterman and Truell, 1961). The validity of this representation and the functional dependence of the attenuation parameter  $\alpha$  with respect to  $\lambda$  for the case  $\lambda \leq a$  is further

investigated in this study.

## **2.3 Ultrasonic Wave Propagation — Experimental Procedure**

### **2.3.1 Experimental Apparatus**

Experiments were performed to measure the intensity field of an unfocused circular disc transducer in single phase and multiphase systems. In particular, acoustic velocity, attenuation and beam geometry were measured. These experiments were conducted in a water bath of 30 cm width, 60 cm length and 25 cm height. The transmitting transducer was attached to a housing with three degrees of linear motion provided by an x-y stage which itself was placed on a movable rail. The transducer could thus be moved axially and radially with respect to the receiver in a controlled and measureable fashion (Figure 2.3). The receiving transducer was mounted on a 3 mm aluminum plate in a rigid mounting in the water bath. The transmitter which was typically operated in a tone-burst mode, was driven by a frequency generator (Wavetek Model 166) via a 100 W RF amplifier (Amplifier Research AR15). The frequency generator was triggered internally to emit bursts of 10-20 sinewaves in the frequency range 100 kHz to 1.0 MHz. The receiver was connected to an ultrasonic amplifier (Panametrics 5052PR) with variable gain in the range 0 dB to 60 dB, and the amplified signal was then filtered (Krohn-Hite 3320) at a cut-off frequency of twice the emitted frequency in each experiment. The transmitted and received signals were displayed simultaneously on a digital oscilloscope from which the requisite information could be measured. The magnitudes of the transmitted and received signals were compared to evaluate the attenuation and beam geometry features,

and the delay time between the transmitted and the received signals was measured to give the sound speed. Thus the sound speed was evaluated from the time of flight of a tone burst between the transmitter and receiver, with the measurement in pure degassed water (having a well-defined sound speed) used as a calibration. The signal intensity was measured at the same peak on both the transmitted and received waveforms (typically the fourth or fifth peak after the initial transients) to maintain consistency between experiments.

### 2.3.2 Transducers

The transmitting transducer used was a flat unfocussed and highly damped, broadband immersion transducer of radius  $R = 9.5$  mm, and nominal natural frequency 1.0 MHz (Panametrics, V302). The intensity fields generated by the unfocussed transmitter were measured by a 1.0 mm diameter bilaminar polyvinylidene fluoromer (pvdf) hydrophone. The receiver was custom made from a small section of pvdf film (Pennwalt Corp.). The active area of the transducer was coated with a dot of silicon rubber sealant corresponding to the final area of the receiver, and the excess metallized surface on the pvdf sheet was removed with acetone and an *aqua regia* solvent. The piezoelectric polymer pvdf has several distinct advantages in its use for acoustic receivers, including the fact that transducers may be tailor-made to virtually any dimension, and such hydrophones have a very flat frequency response in the range from DC to several MHz. The receiver used in these experiments was chosen for its small size and hence the local nature of its reception characteristics. The frequency response of the transmitter-receiver system was measured under controlled conditions in pure water for each separate experiment to allow effects associated with the medium, such as attenuation and

beam geometry to be separated from the system characteristics. The system response is shown in Figure 2.10 — the attenuation in pure water is considered to be negligible to the attenuation in the two phase mixtures, and so the pure water curve is taken to be the system frequency response. All measurements of amplitude were made relative to the (unattenuated) water curve, with an additional correction for beam geometry effects as discussed in Section 2.4.5.

### **2.3.3 Transducer Alignment**

The acoustic intensity field produced by a transducer varies greatly with position, and consequently accurate positioning of the transmitting and receiving transducers is critical. Initial coaxial alignment is achieved in an iterative fashion. The receiver is positioned at roughly the distance known to correspond to the focal length of the transmitter at the particular frequency of operation, and is then traversed axially and laterally in small increments until the maximum is detected. The transmitter is then moved back and forth along the axis and at each axial position, it is translated radially to ensure that the two are indeed aligned coaxially. This procedure is conducted prior to all measurements.

### **2.3.4 Transducer Operation**

Often ultrasonic instruments are operated in a pulsed mode, in which the transducer is excited by a pulse of relatively high amplitude and short duration. The transducer then rings down for some period of time (the length of which depends on the degree of mechanical and electrical damping inherent in the unit) at its natural or preferred frequency of operation. In contrast, in the present experiments the transducer was excited by a tone burst or wave packet

of adjustable frequency and amplitude. The length of the tone burst is limited to remain less than the time of arrival of the first echo reflected by boundaries in the system and the repetition rate or the time between successive bursts is adjusted to be longer than the time required for all extraneous reverberations to die away. A burst duration of 10-20 full waves at a repetition rate of about 1 kHz was found to be satisfactory. To avoid nonlinear effects, the amplitude of the emitted signals were kept low. In these experiments, the maximum pressure excursion measured was of the order of 0.15 kPa (or three orders of magnitude less than the ambient), and the typical value was somewhat less than this. At these pressure amplitudes and frequencies, cavitation, which could corrupt the measurements, does not occur.

## **2.4 Experimental Results**

### **2.4.1 Acoustic field in degassed water**

It has previously been shown that commercial flat transducers create acoustic fields that are very close to those predicted theoretically (Adach and Chivers, 1990). Prior to making measurements for the purpose of characterizing the ultrasonic properties of concentrated solid-liquid mixtures, the acoustic field in degassed water was measured as a verification of satisfactory operation of the ultrasonic transducer. This was done in terms of an axial and three radial traverses. The location of the natural focus of a transducer is a near linear function of the reduced transducer radius. The axial distribution for the 9.5 mm radius, 1 MHz transducer has a measured natural focus at 58.4 mm as shown in Figure 2.4 while the corresponding calculated value is 52 mm. This discrepancy is probably the

consequence of the uncertainty in the effective radius of the active piezo-electric ceramic element, which can also be the source of the minor and typical error in the axial intensity decay. The radial profiles in intensity were measured at 58.4, 89.4 and 151.4 mm. These are shown in normalized form in Figure 2.5, and they agree relatively well with the result of the Rayleigh integral particularly at the greater axial distance. The measurements show qualitative agreement with the off-peak oscillations in predicted intensity. Based on the measurements shown and many others it is found that the measured fields consistently show good predictability in the far field and a lesser agreement in the Fresnel region.

#### **2.4.2 Acoustic field in packed beds**

The properties of packed beds were characterized by means of similar acoustic field measurements for various fixed dimensions of the test cell. The active transducer was positioned directly against the acoustically transparent window of the container that held the packed mixture of 1.0 mm nominal diameter glass beads in water (the actual average diameter of the beads was 1.034 mm, with a standard deviation of 0.100 mm). Radial beam traverses were made for each axial separation between the transmitter and receiver (50, 75 and 100 mm), and are shown in Figure 2.6 for a frequency of 0.30 MHz. To calculate the amplitude of the corresponding non-attenuating acoustic fields (*i.e.*, the acoustic field due solely to geometric effects) for the purpose of comparison, the medium sonic velocity is required. To this end, the acoustic phase velocity was measured for the packed bed as a function of frequency.

### 2.4.3 Phase velocity in packed beds of glass beads and water

The phase velocity was derived from the measurement of the time of flight between the transmitter and the receiver. The measurement was calibrated by first measuring the transit time in pure degassed water, and comparing this value to that calculated using accepted values of the sonic velocity in water (Del Grosso and Mader, 1972). The residence time of the tone burst in the transducer housings, established using this baseline, was then subtracted from subsequent readings. In the packed bed of glass spheres and water, the phase speed shown in Figure 2.7 displays a gentle, monotonic decrease as a function of frequency, with no evidence of scale effects when  $ka$  becomes of order one or greater. It is not understood whether this decrease is physical or whether it is an experimental artifact, but it is clear that this result directly disagrees with the truncated theoretical representation of the “multiple scattering” model (Anson and Chivers, 1989) which shows great fluctuations of sonic velocity with  $ka$ . Further it is interesting to note that only one wave speed was detected in these settled bed experiments. Plona (1980) has shown that porous media of finite solids’ stiffness may display three types of wave, a slow compressional, a shear and a fast compressional wave in order of ascending speed. The present results show a complete absence of the fast compressional wave which could either be the result of the method of emission favoring only one wave mode, or that the stiffness of the solids’ matrix is minimal in these experiments. As is shown below in the fluidized bed experiments, the absence in detectable difference between the sound speed in the settled and incipiently fluidized states leads the authors to believe that the settled beds are effectively cohesionless.

#### 2.4.4 Comparison with Rayleigh theory

The acoustic field in a non-attenuating medium can be fully represented by the wave speed and the transducer geometry alone. The radial beam profiles corresponding to the above packed bed conditions were computed and are shown together with the data in Figure 2.6. In this figure, both the calculated and measured curves are normalized with their respective peak values. Although the dimensional magnitudes of these maxima differ, the geometrical similarity between the theoretical curves and the data is striking, particularly near the axis, and the Rayleigh theory is well able to represent beam width. It is hypothesized that the decay of beam amplitude, which the unattenuated theory fails to capture, may be described by the attenuated version of the Rayleigh integral (Equation 2.1). Using this representation, numerical values of the attenuation parameter,  $\alpha$ , could then be derived from measurements. It should be noted that the far field intensity decays due to both geometrical spreading and due to the presence of solids. Typically the inverse square geometrical attenuation effect has not been taken into account in previous investigations (Machado *et al.*, 1983) which leads to an overestimation of the attenuation due to scattering. The purpose of the present measurements is to extend the investigation of the effect of wavelength down to  $ka \approx 1$ , and to include the effect of solids' concentration (discussed in Section 2.5.2) on the attenuation in mixtures. To address the former, further traverses for  $f = 0.8$  MHz ( $ka = 1.5$ ) were obtained. These are shown in Figure 2.8, with the corresponding unattenuated Rayleigh result based on the measured mixture phase speed. The agreement persists even for high values of  $ka$ . The non-focussed transducer is seen to have a radial beam width of approximately 25 mm at 50 mm in the two phase mixture. The measured radial profiles produced by a focussed transducer (Panametrics, V314) at 70 mm in a packed bed of 1.0

mm silica beads at 0.545 MHz and 0.700 MHz are compared with the theoretical profiles predicted by the Rayleigh theory in Figure 2.9. The transducer is focussed by the addition of an acoustically matched plastic spherically concave lens, and has a natural focus of about 40 mm in water at 0.5 MHz. The theory was found to match the behavior of the transducer, of nominal radius 12.7 mm and 3.2 mm lens depth, using a theoretical radius of 13.3 mm and 1.2 mm depth (this specifies the shape of the surface where monopoles in phase are distributed). The focussed transducer is seen to have a radial beamwidth of approximately 10 mm at 70 mm, or somewhat less than half of that of the non-focussed transducer.

The Rayleigh integral is seen to be quite general in its form and to be able to predict the intensity field for both focussed and non-focussed transducers. It appears, therefore, that for this specific application, an equivalent single phase characterization of the two component mixture is appropriate. Such a representation is adopted here and is utilized to represent all measured mixture attenuation values in this study.

#### 2.4.5 Attenuation in packed beds

Since the attenuation in pure water is found to be negligible compared to the attenuation in the packed mixture, it is convenient to present the attenuation,  $\alpha$ , relative to degassed water measurements. In quantifying attenuation, the following factors were recognized to affect the amplitude of the received signal:

- a) the frequency response  $H(\omega)$  of the transmitter-receiver combination,
- b) the position of the measuring location relative to the natural focus, and
- c) the signal loss due to the presence of solids.

The received axial signal amplitude ( $V_{water}$ ) through degassed water at a fixed separation,  $L$ , between transmitter and receiver can therefore be presented

as

$$V_{water} = V_{trans}H(\omega) \int_A u \frac{e^{-i(\omega/c_{water})L}}{2\pi L} dA, \quad (2.4)$$

while the corresponding amplitude received through the mixture is

$$V_{mixt} = V_{trans}H(\omega)e^{-\alpha L} \int_A u \frac{e^{-i(\omega/c_{mixt})L}}{2\pi L} dA. \quad (2.5)$$

Dividing (5) by (4), an expression emerges for the attenuation parameter:

$$\alpha \simeq \frac{1}{L} [\ln V_{water} - \ln V_{mixt}] + \ln \left[ \frac{\cos(\omega/c_{mixt})L}{\cos(\omega/c_{water})L} \right]. \quad (2.6)$$

This form was used to evaluate  $\alpha$  from experiments performed in the constant dimension test section for  $L = 50, 75$  and  $100$  mm. The trigonometric correction factor in Equation 2.6 accounts for the relative axial position of the receiver with respect to the natural focus, and it is named the geometrical factor. At the axial distances considered, namely  $L = 50, 75$  and  $100$  mm, the magnitude of this factor is small with a maximum deviation of the order of 20%. However all measurements were adjusted to take this correction into account. The experiments consist of measuring the received signal for a full range of excitation frequencies. Typical unreduced data for these tests are shown in Figure 2.10 for both water and settled beds. The degassed water curve contains the combined transmitter-receiver frequency characteristics with a maximum at 0.9 MHz, which is consistent with the nominal transmitter natural frequency of 1 MHz, and the high receiver natural frequency. The mixture signal amplitudes show little deviation from the water values at low frequencies, but they typically begin to deviate from the water curve at a frequency of approximately 0.4 MHz ( $ka = 0.75$ ). These resulting attenuation parameter values are presented

in Figure 2.11 in dimensionless form ( $\alpha a$ ) as a function of the reduced frequency  $ka$ . The log-log presentation of the data exhibits two distinct regions. At low frequencies, the attenuation parameter appears to depend approximately linearly on frequency, while the change in slope indicates an apparently quadratic dependence on frequency for  $ka > 0.75$  (this result is consistent with the results of Salin and Schön, 1981, for attenuation in porous media). Further tests were carried out to verify these findings and to characterize the effect of solids' fraction using a similar apparatus with the additional ability of fluidizing the mixture to lower solids' concentrations.

#### 2.4.6 Experimental error analysis

Typically, the accuracy to which the received and transmitted signal amplitudes could be measured was to within approximately  $\pm 1\text{mV}$ . At the low and high solids' fraction limits, this would correspond to as much as 5% of the total measured amplitude, while being as low as 1-2% at the intermediate concentrations (corresponding to the minimum attenuation). This indicates that the error in the attenuation as calculated in Equation 2.6 is no more than about 10% at the high and low concentration limits, and as low as 2-4% at  $\nu = 0.30$ . The error in the sound speed measurements was minor — the typical time of flight durations were 50-100  $\mu\text{s}$ , measured with an accuracy of about 1.0  $\mu\text{s}$ . This would indicate a relative error of no more than 2% in the sound speed estimation.

### 2.5 Fluidized Bed Acoustic Experiments

In order to obtain attenuation and wave speed behavior of acoustic propagation in systems of varying concentration, experiments were conducted in a

fluidized bed. Here the concentration of the solid-liquid mixture could be varied by adjusting the upwards velocity of liquid through a bed of particles initially supported on a porous plate. An ultrasonic transducer transmitter-receiver pair was mounted horizontally on the vertically aligned 100 mm tube (Figure 2.16). Liquid-solid fluidized beds are kinematically quite stable with small local fluctuations of solids' fraction, due to the discrete nature of solid-liquid systems (Foscolo and Gibilaro, 1985). Although such fluctuations are present, the period of oscillation of the acoustic wave propagation used ( $T = \frac{1}{\omega} = \frac{1}{2\pi f}$ ) is very much smaller than the characteristic time scale of acceleration of the individual particles ( $T_p = \frac{a^2 \rho_p}{18 \mu_l}$ ), so that the particles may be considered to be frozen in space, particularly for tone bursts of short duration. At intermediate concentrations, that is to say at solids' fractions between those corresponding to infinite dilution and maximum packing, there is some instability in these fluidized beds and this can lead to ambiguity in the interpretation of the acoustic wave attenuation, for example. This instability, which is related to particle inertia, is more pronounced for larger solid to liquid density ratios, and is most significant in the concentrations below about 50% by volume. Spatial variations in concentration along the line of measurement, coupled with the non-linear behavior of attenuation with concentration, can further complicate the interpretation of attenuation results.

In these experiments 1.0 mm glass beads were fluidized in water, and the typical frequencies of the sound used were in the range 100 kHz to 1.0 MHz ( $ka = 0.2 \sim 2$ ). The apparent concentration of the solids in the fluidized bed was determined from the height of the upper surface of the bed and was assumed to be fairly constant across the bed height.

### 2.5.1 Sound speed variation with concentration

The variation of the speed of sound with solids' fraction is shown in Figure 2.12. It has the anticipated behavior at the two extremes of concentration: at very low concentrations, the sound speed is roughly that in water under the same conditions, it increases monotonically as a function of concentration and at the maximum packing limit, the sound speed is the same as that in the packed bed case. For comparison, the phenomenological model of Urick (1947) (described in Section 3.2) that is based on the effective bulk modulus and density of the mixture is also shown in this figure. In contrast to the experimental results, the theory predicts that the sound speed has a minimum at intermediate concentrations of the order of 20% by volume. It should be noted, however, that the theory corresponds to the long wavelength limit, namely  $ka \rightarrow 0$ , while the experimental results are for  $ka \sim 1$ . As was found in the settled bed experiments, there is a dependence (albeit rather weak) of sound speed on frequency. Consequently, the simple although rather robust theoretical representation of Urick (which does not contain any mechanism to describe frequency dependence) contains the relevant ingredients to give a reasonable first order approximation to the sound propagation velocity. (An analytical study of the variation of the sound speed with frequency is given in Chapter 3).

### 2.5.2 Variation of attenuation with concentration

The variation of  $\alpha$  with respect to frequency, described in Section (2.4.5), showed a monotonic increase and two distinct regions of dependence. At low frequencies,  $ka < 0.75$ , the attenuation grows approximately linearly with frequency, while the relationship apparently becomes quadratic for  $ka > 0.75$ . As

an extension of this, the dependence of the attenuation parameter on frequency was evaluated for various values of the solids' fraction. The picture that emerges is complex and to help its interpretation, the attenuation parameter is plotted as a function of concentration with frequency as a parameter in Figure 2.13 from which the following traits can be distinguished. At low concentrations ( $< 20\%$ ) the attenuation increases with both frequency and concentration such that the slope of attenuation vs.  $\nu$  increases with the frequency. Indeed, by linear superposition of losses due to individual scatterers, one would expect that the increase would be monotonic with concentration. In practice this signifies that penetration becomes poor with higher solids' loading, particularly at higher frequencies. This has long been known, for example, as the reason why commercially available ultrasonic Doppler velocimeters fail at higher solids' contents. As the concentration is increased above 20% while maintaining a constant frequency, the attenuation behaves in a dramatic and counterintuitive fashion by first leveling off and then decreasing at higher concentrations. This phenomenon is particularly marked at high frequencies of operation. For example, at an operating frequency of 0.8 MHz ( $ka = 1.5$ ), the attenuation in 62% solids (1 mm) is the same as in a mixture with 6% solids, while the peak attenuation coefficient  $\alpha$  assumes twice the 62% value at a concentration of 25%. For the present system of 1 mm glass beads and water, the non-monotonic character of the attenuation parameter is most prominent at frequencies above 0.4 MHz, ( $ka = 0.75$ ). This behavior has previously been observed by Urick (1947, 1948) and Hampton (1967) in their experiments with kaolinite suspensions (mean diameter of 2.26 and 0.83  $\mu\text{m}$  respectively according to Gibson and Toksöz, 1989), and their data are included in Figure 2.14 for comparison. It can be noted that the attenuation in these colloidal suspensions is high relative to the present results for the same range of

frequencies. But when these attenuation data are appropriately rendered dimensionless with particle radius ( $\alpha a$ ), they are indeed found to scale approximately linearly with reduced frequency ( $ka$ ) with one another and with the new data presented. This reinforces the assertion that the correct scaling for two phase mixtures is the parameter  $ka$ , and that experiments at similar values of the non-dimensional wavenumber may be compared directly, for mixtures with the same material properties.

## 2.6 The Design of Ultrasonic Instrumentation and the Limitations of the Technique

It is clear from the results of the attenuation at high concentration presented above that it is possible to design an instrument to investigate such mixtures. The parameters that must be taken into consideration in the design of an ultrasonic instrument are

- i) the solids' fraction,  $\nu$ , in the mixture
- ii) the particle size, or more particularly the parameter,  $ka$ ,
- iii) the particle properties (density and compressibility),
- iv) the fluid properties (density, compressibility and viscosity), and
- v) the physical dimensions of the system to be interrogated.

The sound speed,  $c$ , in a particular solid-liquid mixture is determined by the solid and liquid densities and compressibilities, as well as the solids' fraction,  $\nu$ . At a particular frequency of operation, the sound speed fixes the wavelength of the transmitted sound which in turn, with the dimensions of the transmitting transducer, determines the spatial resolution of the ultrasonic measurement. The depth of penetration of the ultrasound is dictated by the attenuation, which varies

with the frequency of sound and the dispersed phase concentration, as well as with the fluid viscosity (an effect not experimentally considered here).

It has been shown that the solids' fraction of the mixture does not represent a significant limitation to the use of ultrasound as a diagnostic technique (particularly as the attenuation at maximum packing is far from its maximum value, which has been shown to occur at around  $\nu \sim 30\%$ ), while the frequency of operation may well be a limiting factor, due to the apparently quadratic increase in attenuation with frequency for  $ka > 0.75$  (Figure 2.11). The most significant limiting consideration in the use of ultrasound for the non-intrusive measurement of highly concentrated suspensions lies in the tradeoff between the spatial resolution of the transmitting transducer (as determined by  $kR = \frac{2\pi R}{\lambda} = \frac{2\pi fR}{c}$ , where  $R$  is the transducer radius) and the depth of penetration of the signal,  $L$ . Good spatial resolution implies a relatively short wavelength, or alternatively a large value of  $kR$  (and hence  $ka$ ). This, in turn, implies high attenuation and a relatively short depth of penetration,  $L$ . For the system and the range of parameters studied, a simple expression (to be motivated in Chapter 3) can be used to represent the attenuation parameter  $\alpha$  for values of  $ka < 1$ , which is the range of practical interest as attenuation becomes prohibitive at shorter wavelengths:

$$\alpha a \simeq (ka)^{\frac{3}{4}} g(\nu). \quad (2.7)$$

The function  $g(\nu)$  describes the nonmonotonic effect of concentration, and it is plotted in Figure 2.15 for the data of the present study and those of Hampton (1967) and Urick (1948). The comparison with the data of Hampton and Urick, while far from perfect, is significant when one considers that the data spans one order of magnitude in frequency (from 100 kHz to 1 MHz) and three orders of magnitude in particle size (from 1  $\mu\text{m}$  to 1 mm). This function is expected to depend on the material properties of the specific constituents (such as bulk

modulus, density, viscosity and particle shape), the effects of which remain to be addressed. Spatial resolution is limited by the size of the natural focal region of typical circular disc transducers. To decrease the focal region, focussed transducers may be used. The addition of an external focussing lens on a piston transducer has the effect of reducing the dimensions of the focal region and increasing the maximum intensity at the focus. With regard to the temporal resolution of acoustic measurements, the frequency response of an ultrasonic system such as the one described presents little or no limitation as phenomena of very short duration can in theory be measured.

## 2.7 Discussion

The propagation of ultrasound in solid-liquid mixtures was investigated experimentally for a range of frequencies at concentrations spanning the range from infinite dilution to maximum packing, in fluidized beds showing minor instabilities, particularly at solids' fractions below about 50% by volume. The measured attenuation has been shown to depend approximately linearly on  $ka$  for  $ka < 0.75$  and apparently quadratically for  $ka > 0.75$ . As a consequence, because the attenuation coefficient,  $\alpha$ , becomes prohibitively large for  $ka > 1$ , it is appropriate to operate at  $ka \leq 1$ . This ensures an optimum wavelength,  $\lambda \sim 2\pi a$ , for the operation of acoustic instrumentation. In contrast, however, the attenuation at a fixed frequency for  $ka < 0.75$  displayed a maximum at a solids' fraction of about 30% for 1 mm silica beads in water, with the attenuation at very high concentrations considerably less than the maximum. The attenuation results presented, correctly scaled, are consistent with the data of Urlick (1947) and Hampton (1967), and extend the range of available data by three orders of magnitude in  $\alpha a$  and  $ka$ . Furthermore, the experiments conducted with silica

beads in water reflect the range of  $ka$  and the materials encountered in sediment transport, slurry handling and many other mining and engineering applications. The intensity field produced by a circular disc transducer in a two phase medium at  $ka \simeq 1$  shows excellent agreement with the Rayleigh integral with the substitution of a modified wavenumber and attenuation parameter, which allows for the prediction of the transducer beam geometry in two phase mixtures for a wide range of frequencies and solids' fractions. This agreement is best in the transducer far field. Errors in the measurement of acoustic attenuation in these experiments are typically related to the reproducibility of experiments; that is to say that experimental uncertainty is dominated by variations between successive experiments. In these experiments, the variation in  $\alpha$  was of the order of 5 - 10%, while the variation in  $c$  was about 5% at worst due to concentration fluctuations about the mean during the experiments.

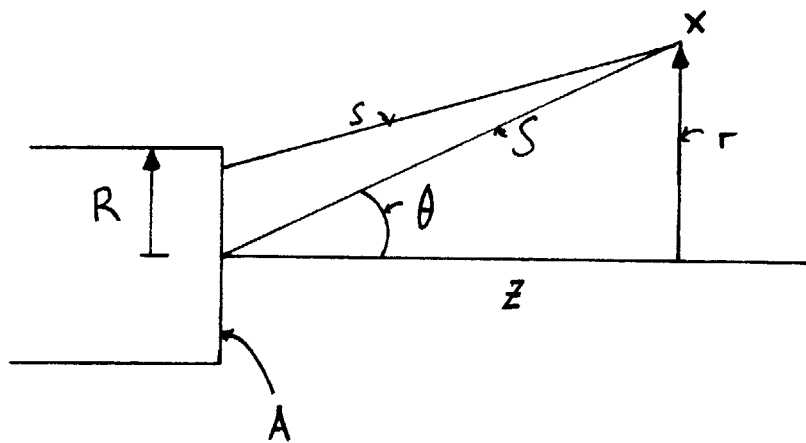


**Figure 2.1** The geometry of the intensity field due to a plane piston transducer. The circular disc transducer area is  $A$  and its radius is  $R$ , the location of the target point is  $x$  at an axial distance of  $z$  and a radial distance of  $r$ , the distance from each point on the surface of the transducer to the target point is  $s$  and the distance from the center of the transducer face to the target is  $S$  at an angle  $\theta$  to the axis.

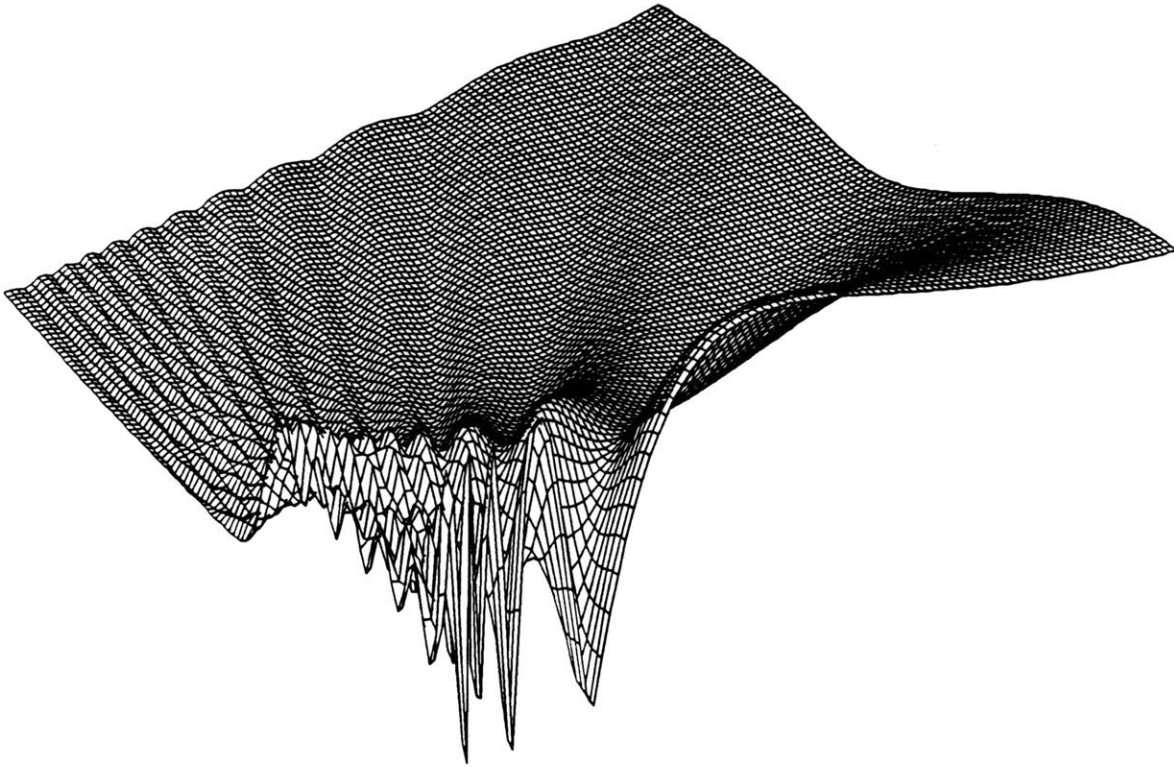


**Figure 2.2** One half of the radially symmetrical intensity profile for a plane piston transducer, calculated using the Rayleigh integral (Equation 2.1), with  $kR = 40$ . In this isometric view, the axial direction, which has a total length of 10 times the transducer radius, is angled to the right. The radial direction is to the left in this square domain. The intensity goes through several maxima in the near field, and then decreases as  $\frac{1}{z^2}$  in the far field, as well as falling off sharply in the radial direction.

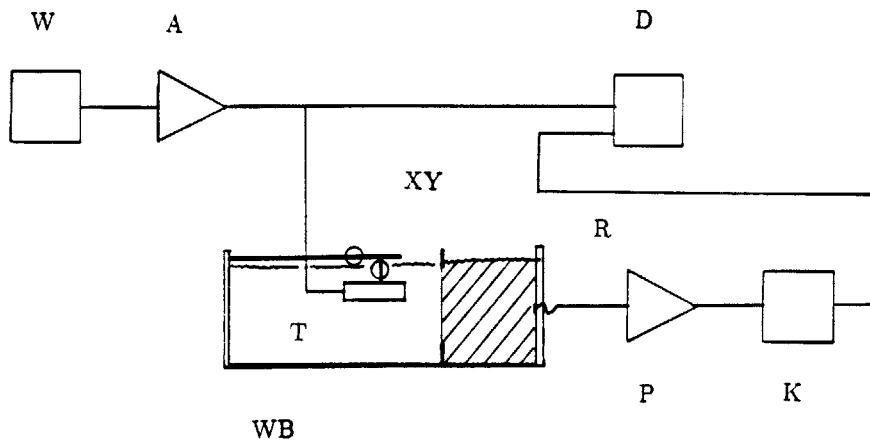


**Figure 2.3** Experimental apparatus for the measurement of sound speed and attenuation in single phase and packed bed mixtures. WB: 60 cm by 30 cm by 25 cm acrylic water bath, T: transmitting transducer, XY: xy travelling stage, R: pvdf receiving transducer, W: frequency generator, A: RF amplifier, P: receiver amplifier, K: low pass filter, D: digital oscilloscope. The test medium is separated from the rest of the water bath by a 10  $\mu\text{m}$  acoustically transparent polythene film.

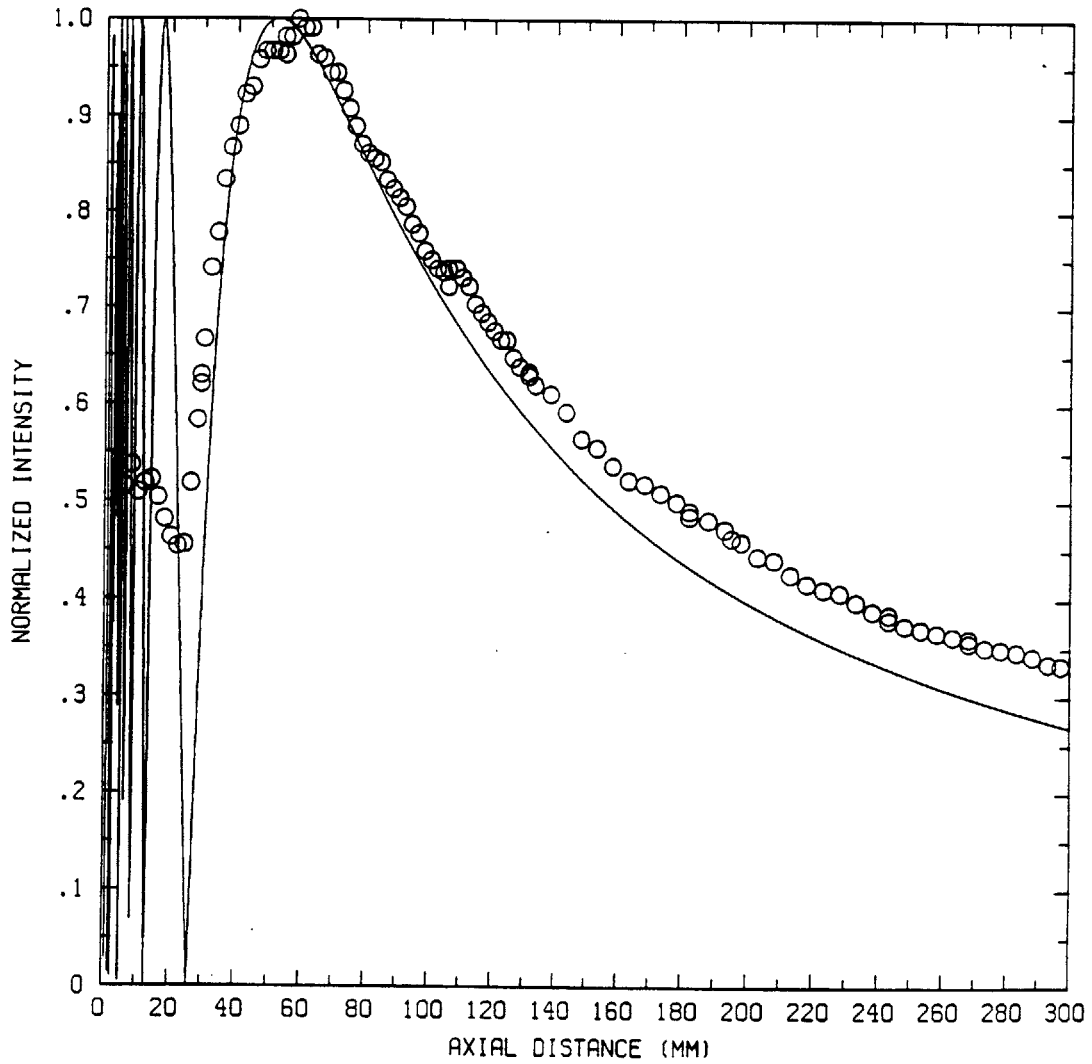


**Figure 2.4** Axial intensity profile for a 9.5 mm radius, 1 MHz non-focussed transducer in water. The intensity is normalized with respect to the maximum value at the point of natural focus. The theoretical curve is calculated using the Rayleigh integral (Equation 2.1).

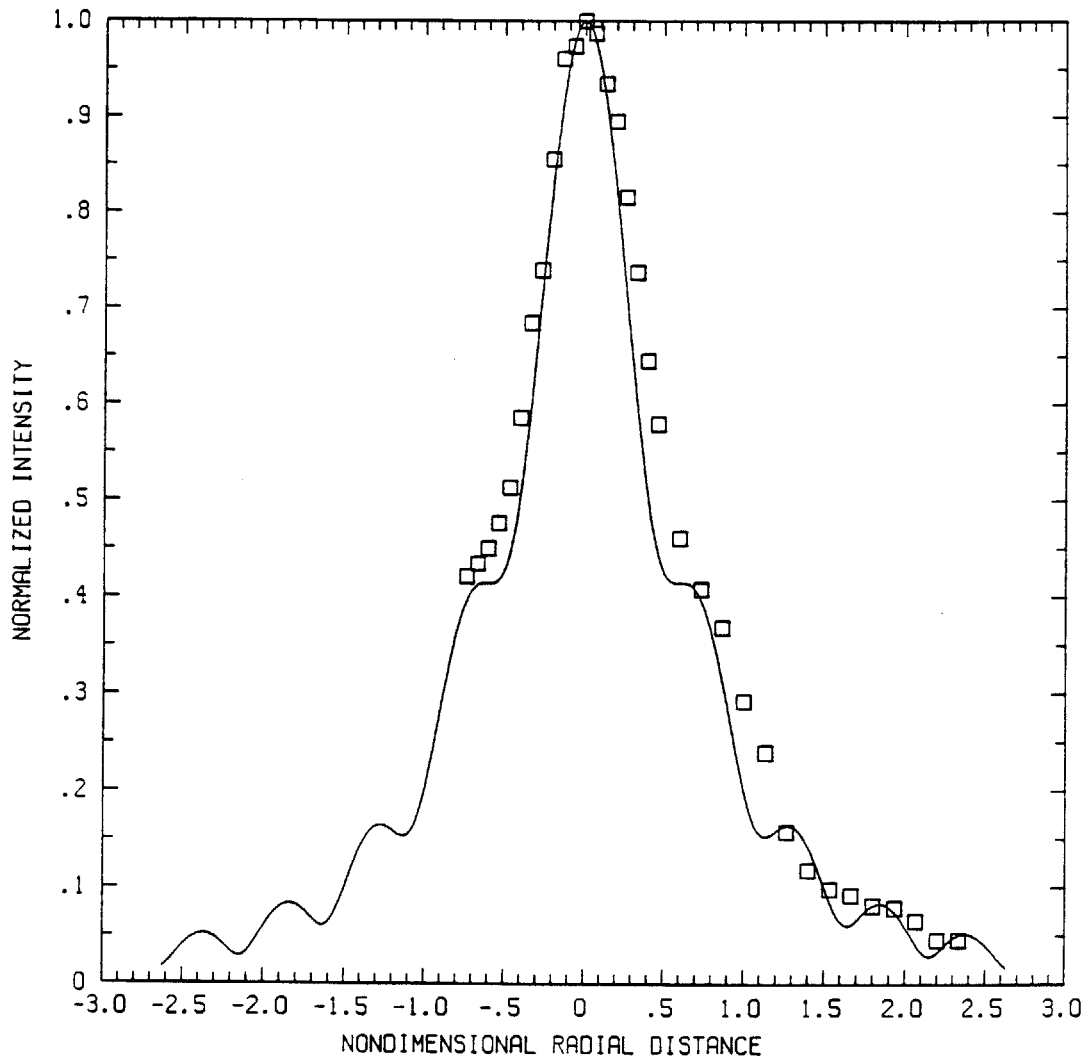


**Figure 2.5a** Radial intensity profile for a 9.5 mm non-focussed transducer, operating at 0.95 MHz in water, at 58.4 mm. The intensity is normalized with respect to the maximum (axial) value while the radial distance is non-dimensionalized with respect to the transducer radius,  $R$ .

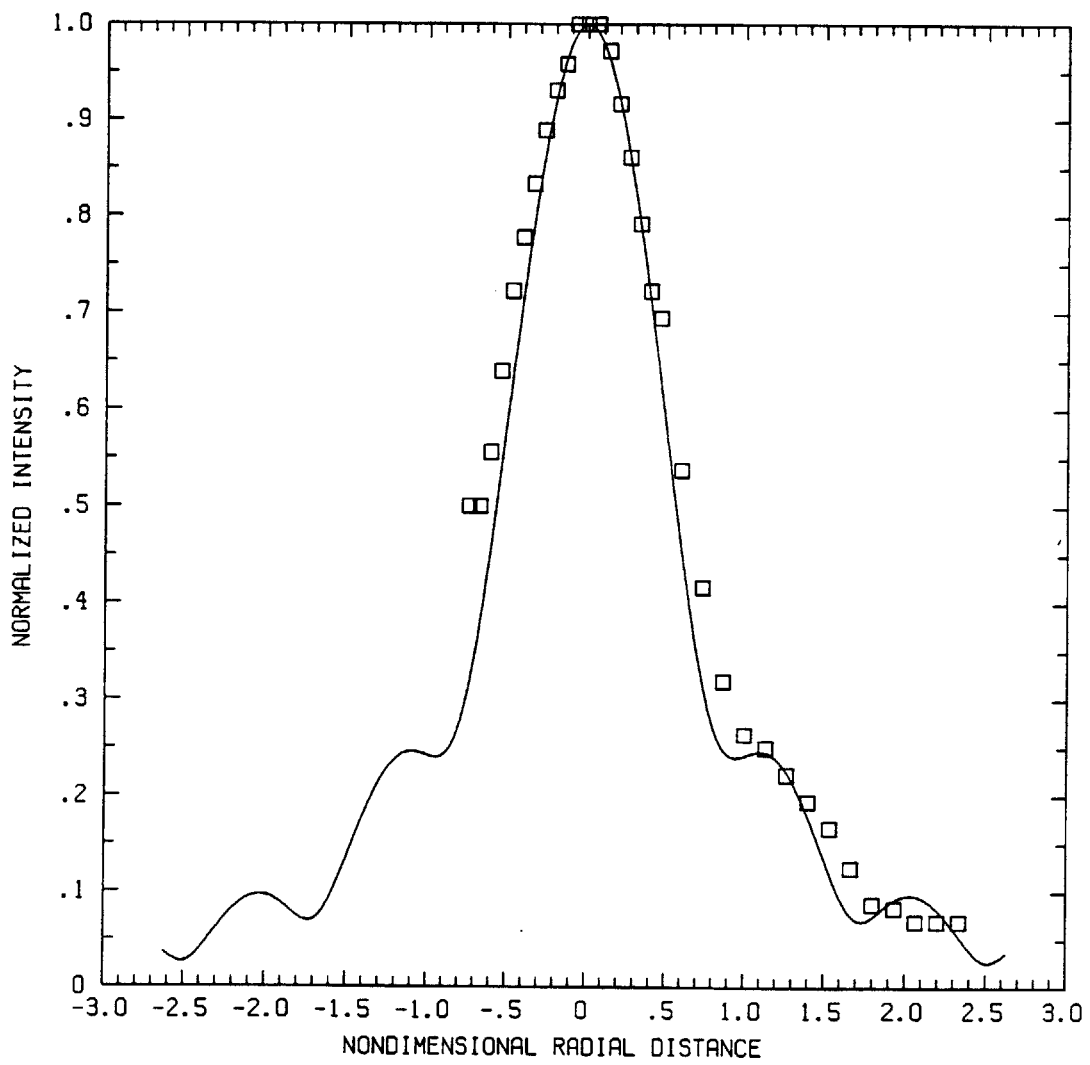


**Figure 2.5b** Radial intensity profile (as in Figure 2.5a) at 89.4 mm.

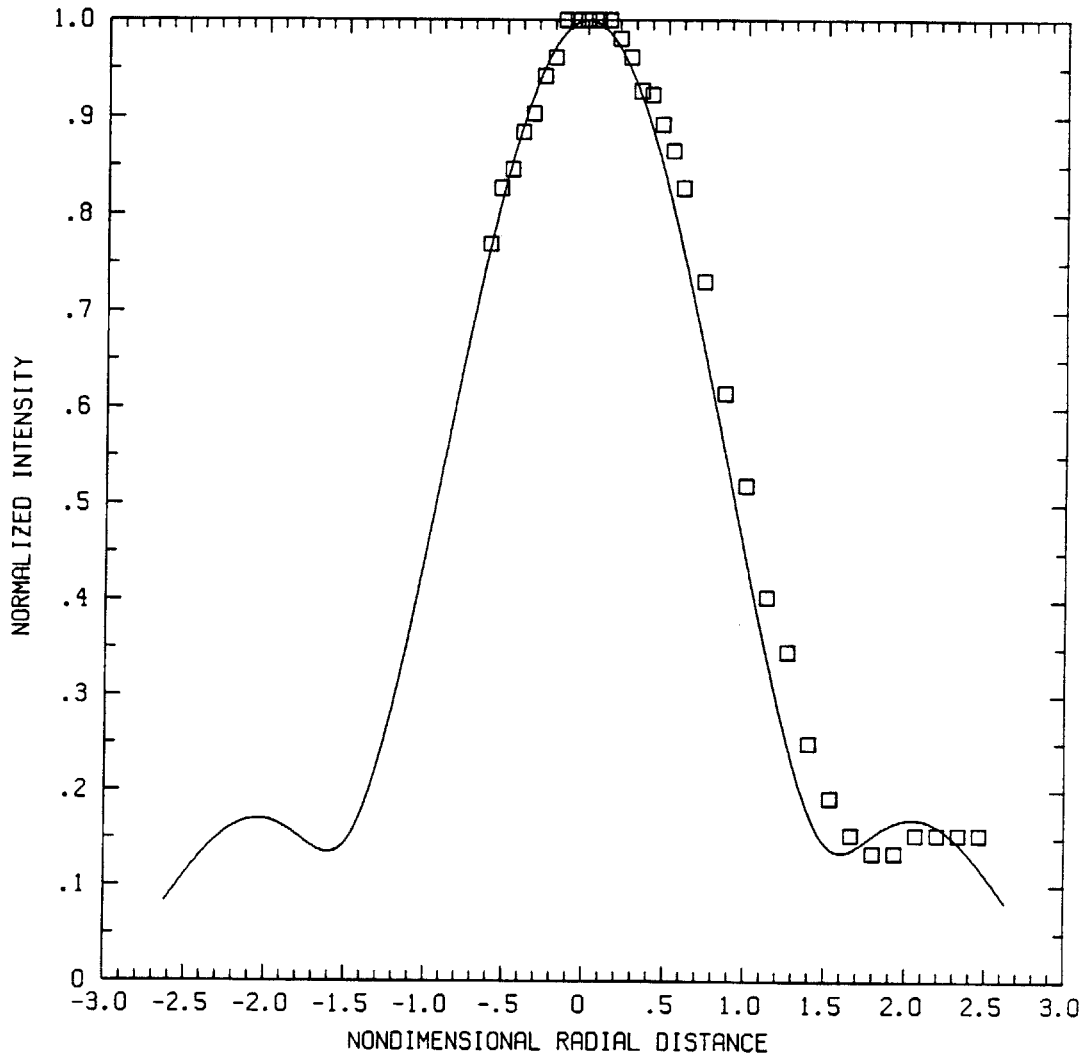
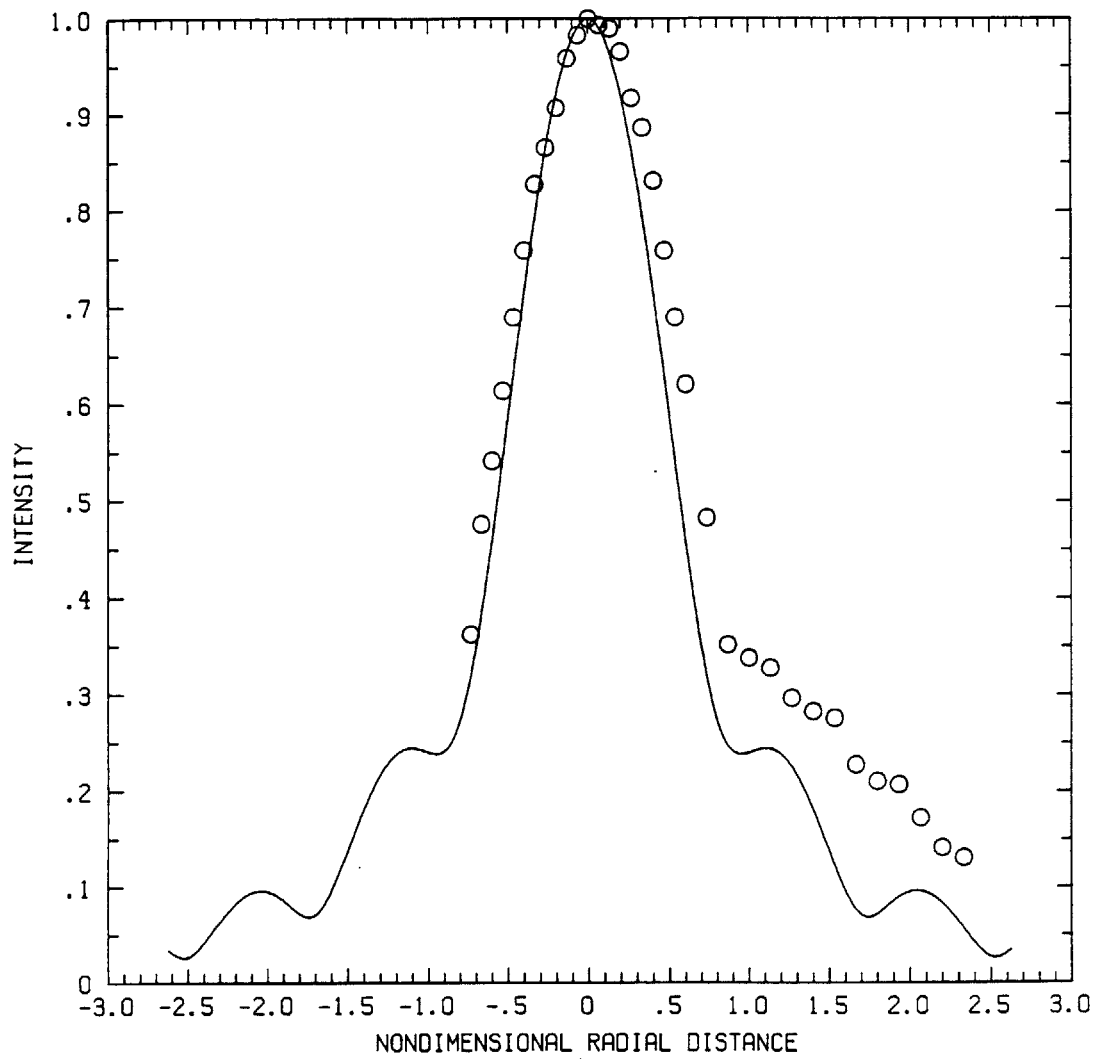
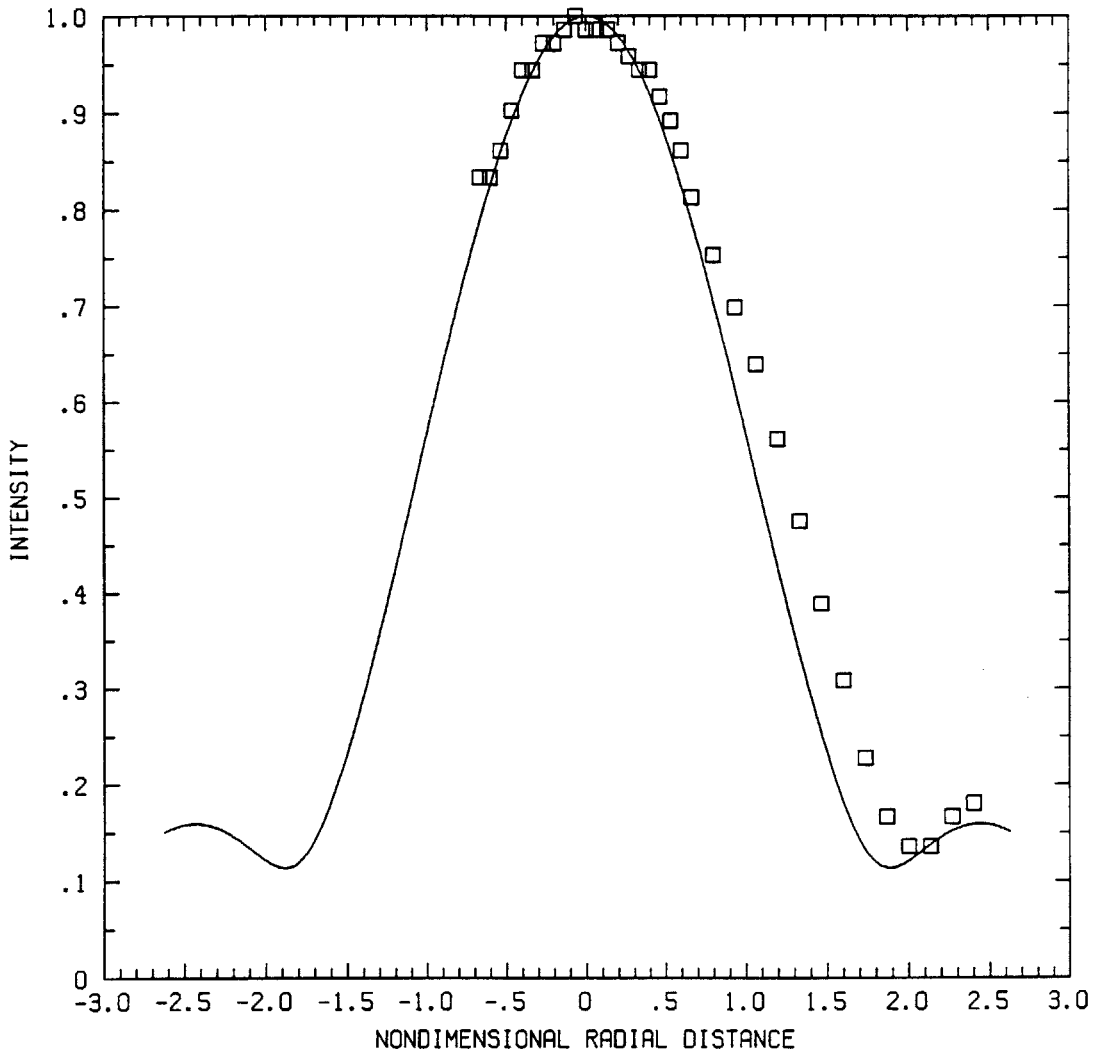


Figure 2.5c Radial intensity profile (as in Figure 2.5a) at 151.4 mm.



**Figure 2.6a** Radial intensity profile for a 9.5 mm transducer, operating at 0.30 MHz in a packed bed of 1.0 mm glass beads in water ( $ka \approx 0.55$ ), at 50 mm. The radial distance is non-dimensionalized with respect to the transducer radius.



**Figure 2.6b** Radial intensity profile (as in Figure 2.6a) at 75 mm.

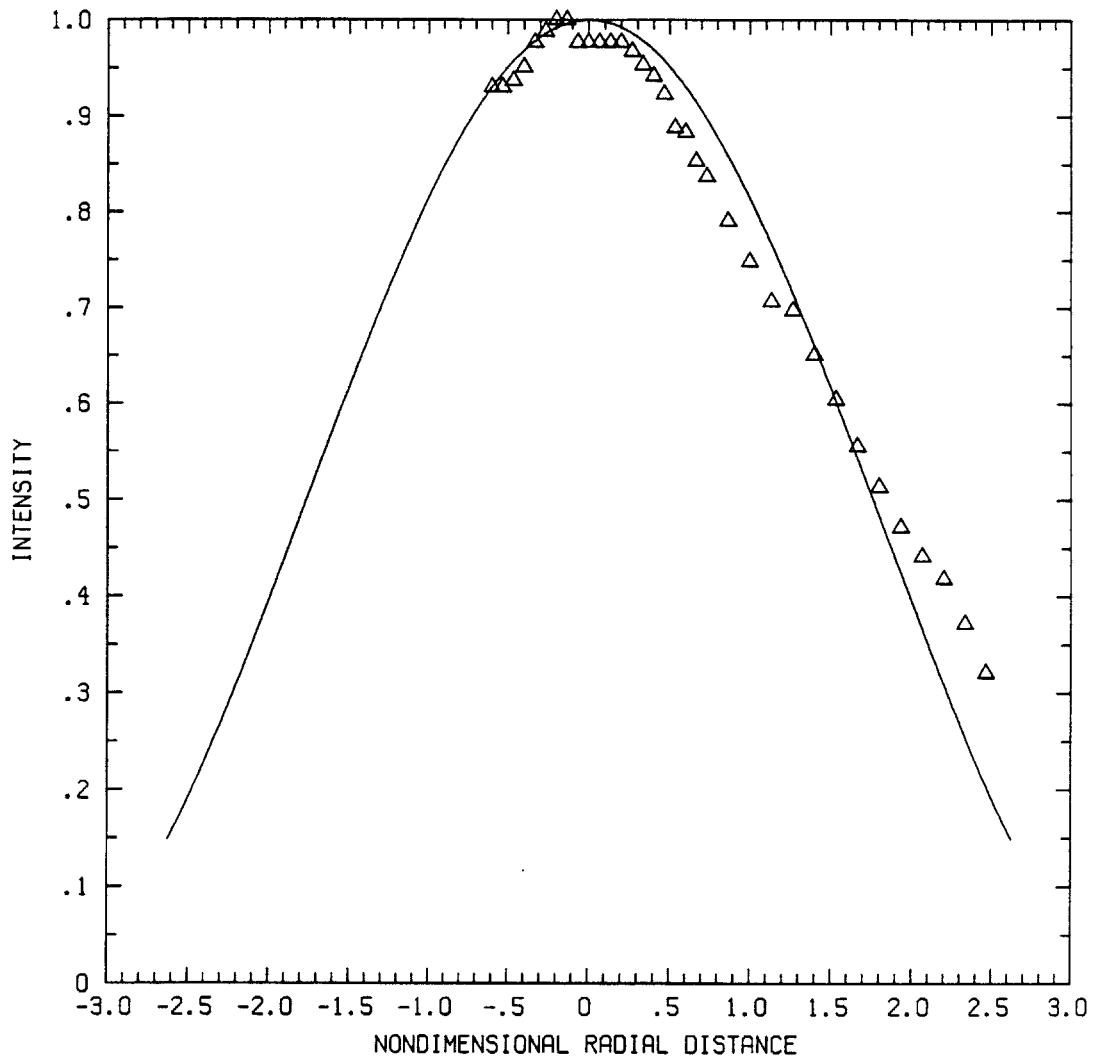
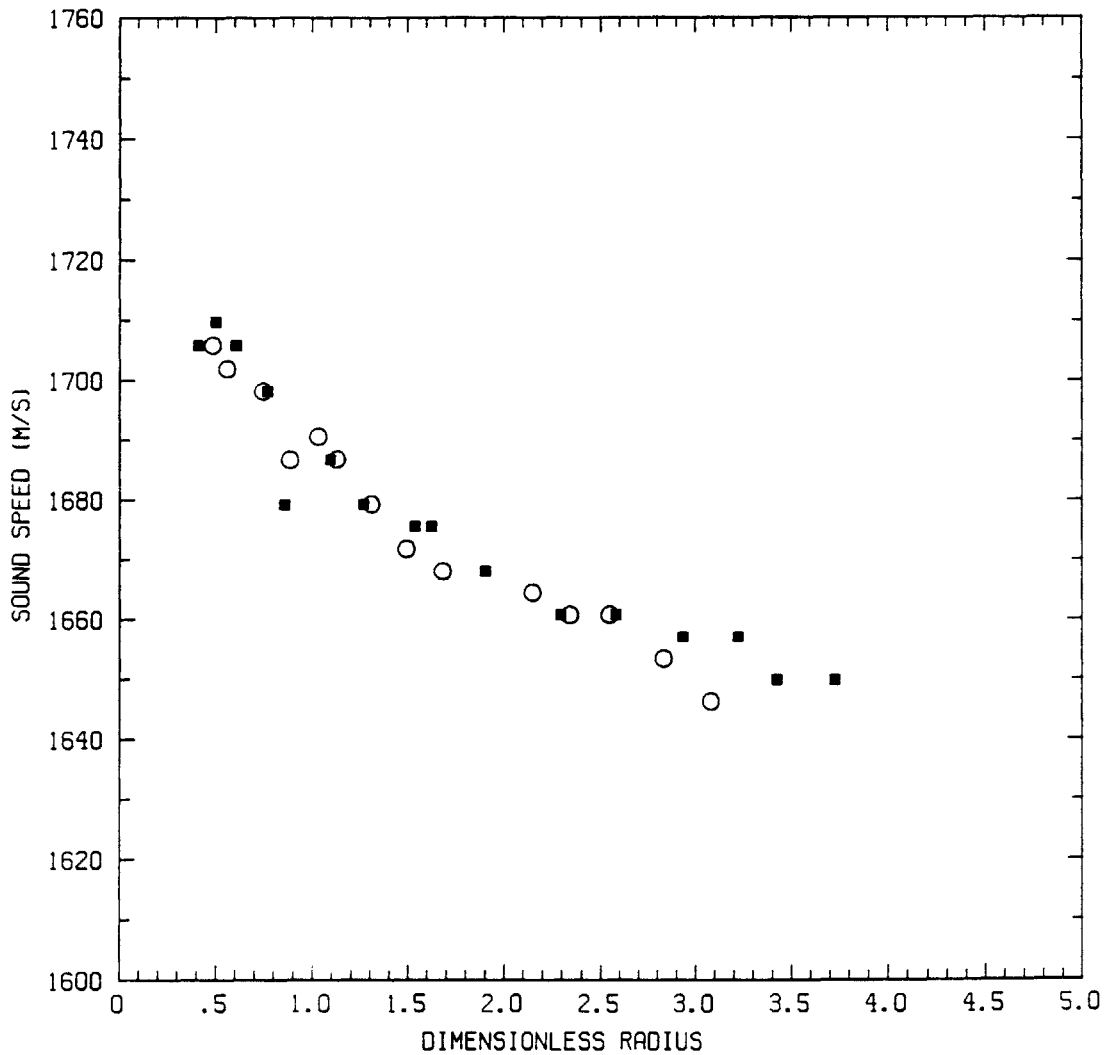
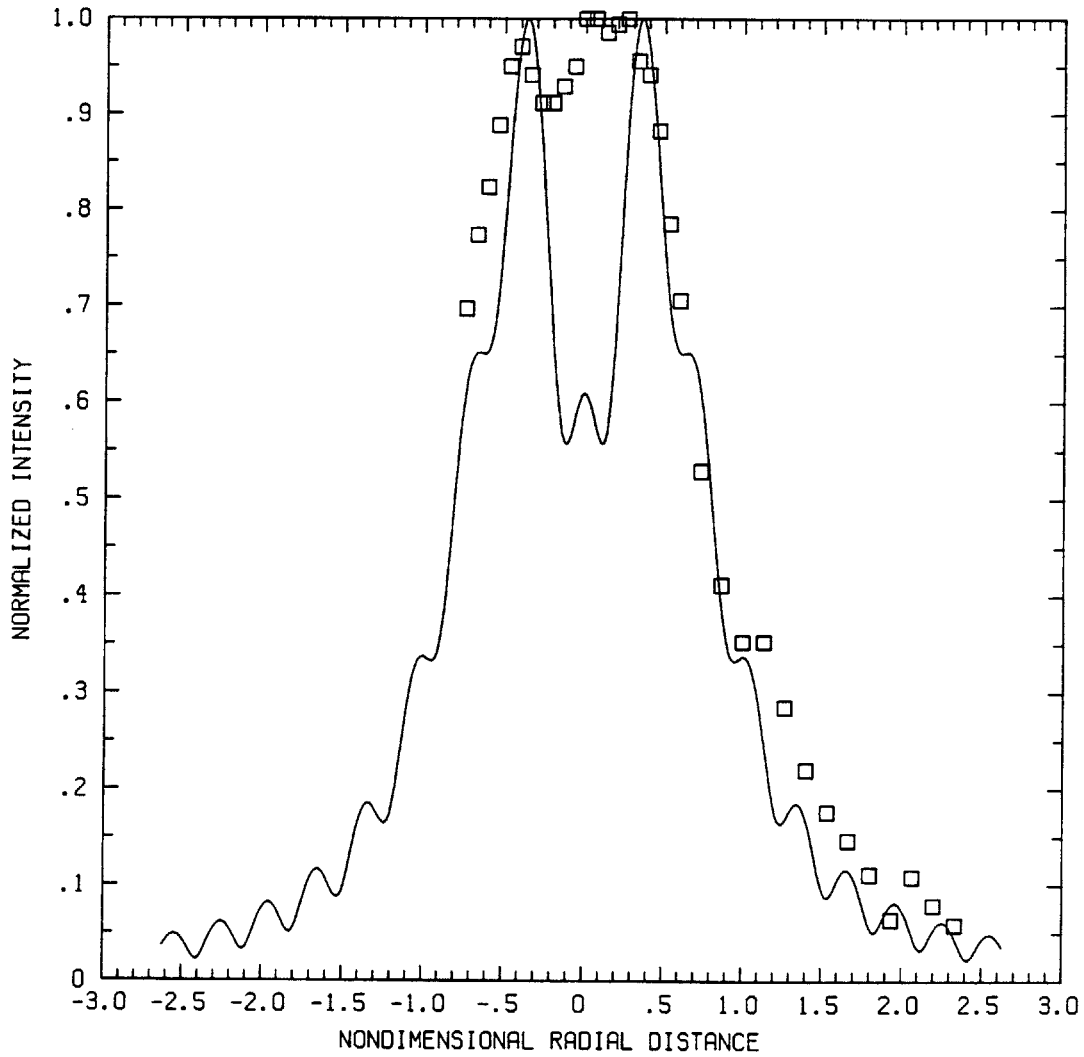


Figure 2.6c Radial intensity profile (as in Figure 2.6a) at 100 mm.



**Figure 2.7** Phase speed of sound in a packed bed of 1.0 mm glass beads in water as a function of  $ka$ , showing a minor monotonic decrease at higher frequencies. Two separate tests are shown on this plot. The sound speed decrease which may be an experimental artifact, is shown to give an indication of the expected experimental error.



**Figure 2.8a** Radial intensity profile for a 9.5 mm transducer, operating at 0.80 MHz in a packed bed of 1.0 mm glass beads in water ( $ka \approx 1.5$ ), at 25 mm. The agreement of the experimental data with the Rayleigh theory persists for higher values of  $ka$ .

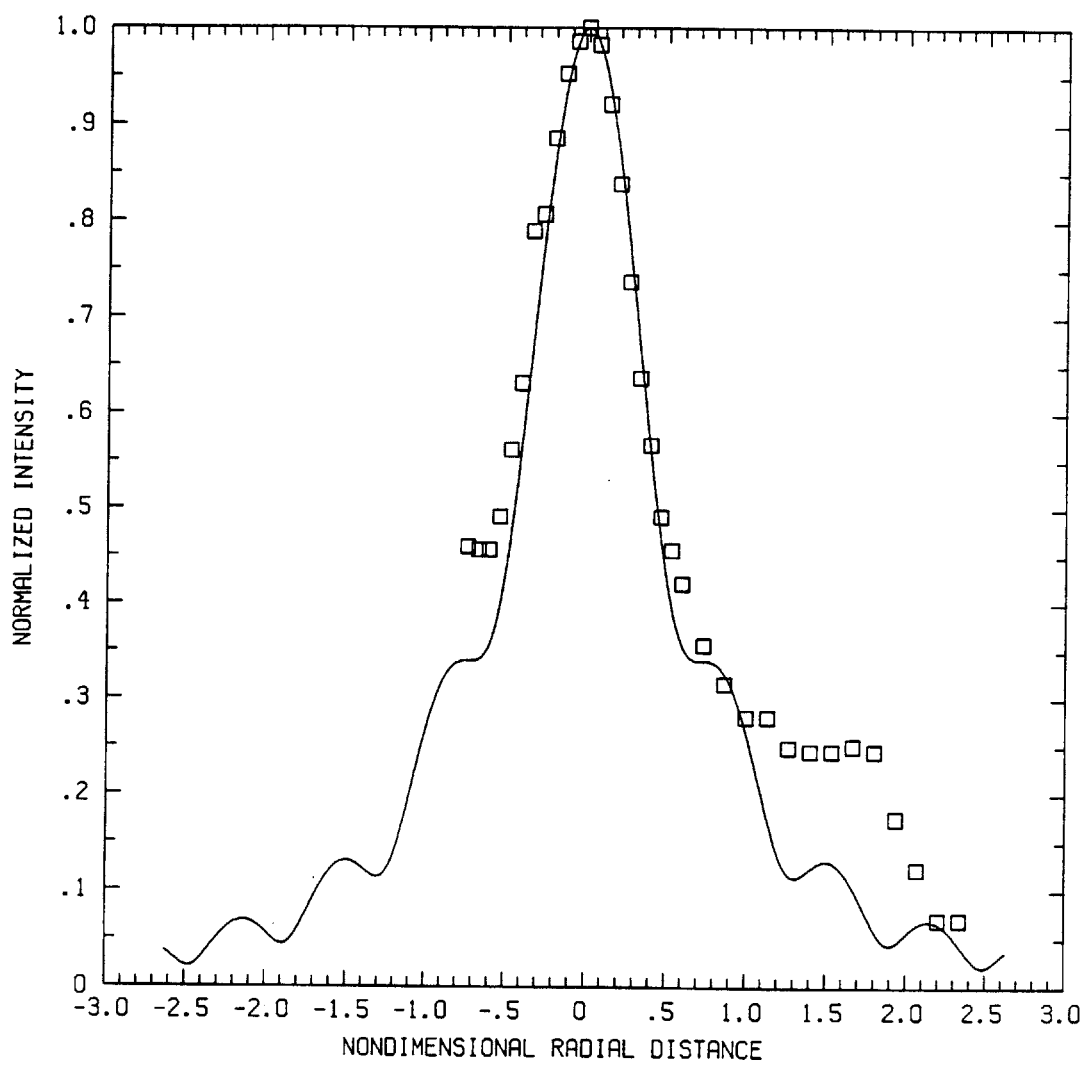


Figure 2.8b Radial intensity profile (as in Figure 2.8a) at 50 mm.

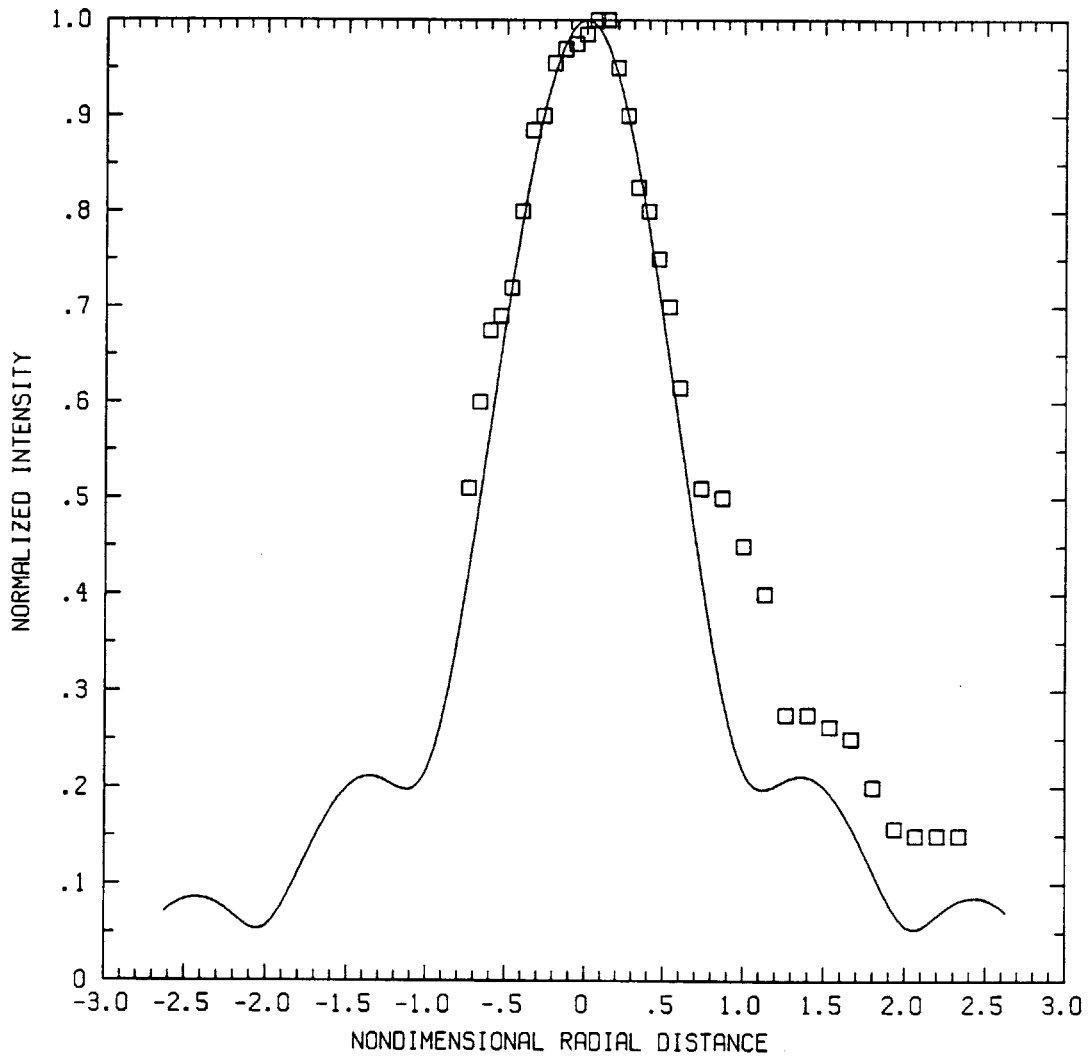
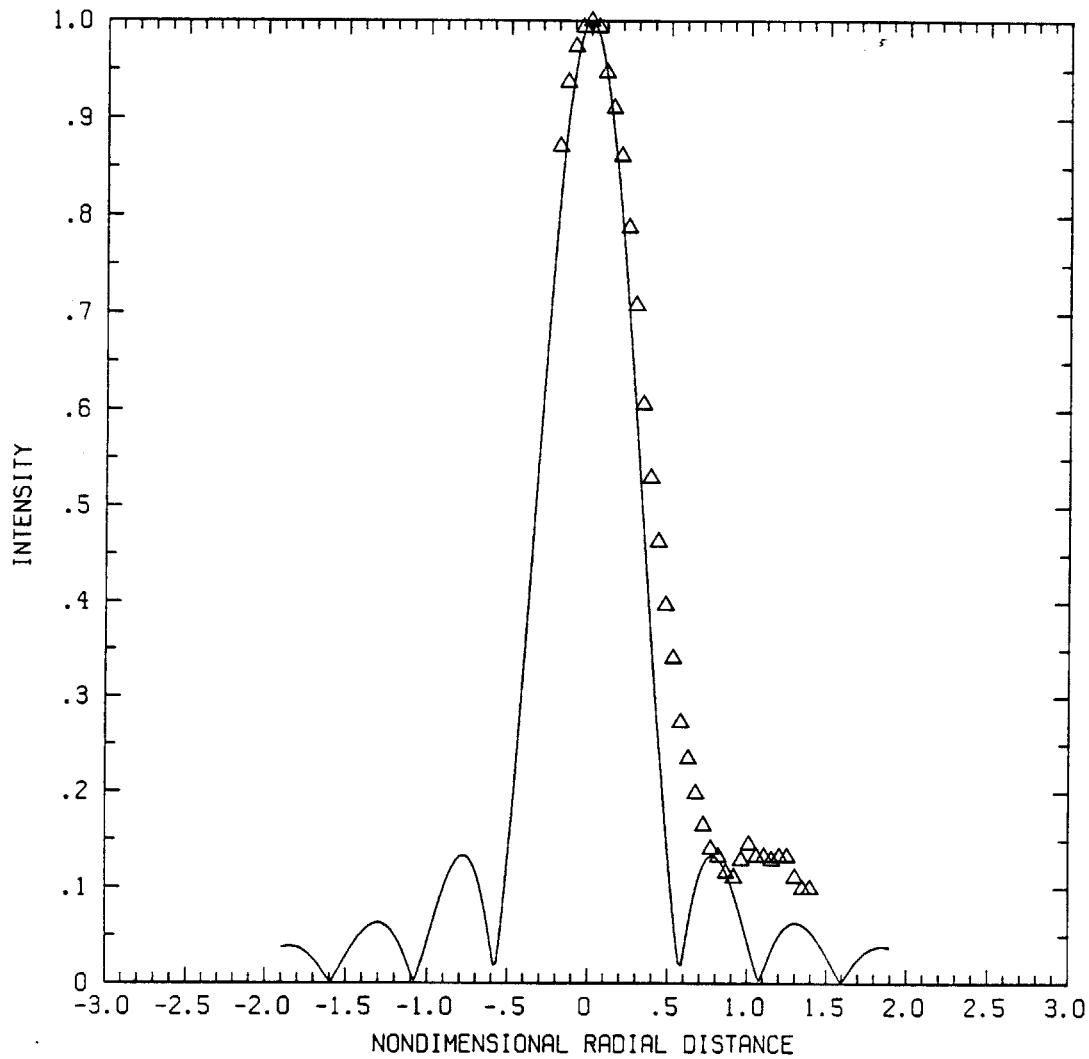


Figure 2.8c Radial intensity profile (as in Figure 2.8a) at 75 mm.



**Figure 2.9a** Radial intensity profile for a 9.5 mm *focused* transducer, operating at 0.70 MHz in a packed bed of 1.0 mm glass beads in water ( $ka \approx 1.3$ ), at 70 mm. The Rayleigh theory is seen to be accurate in predicting the intensity field due to focussed as well as non-focussed transducers.

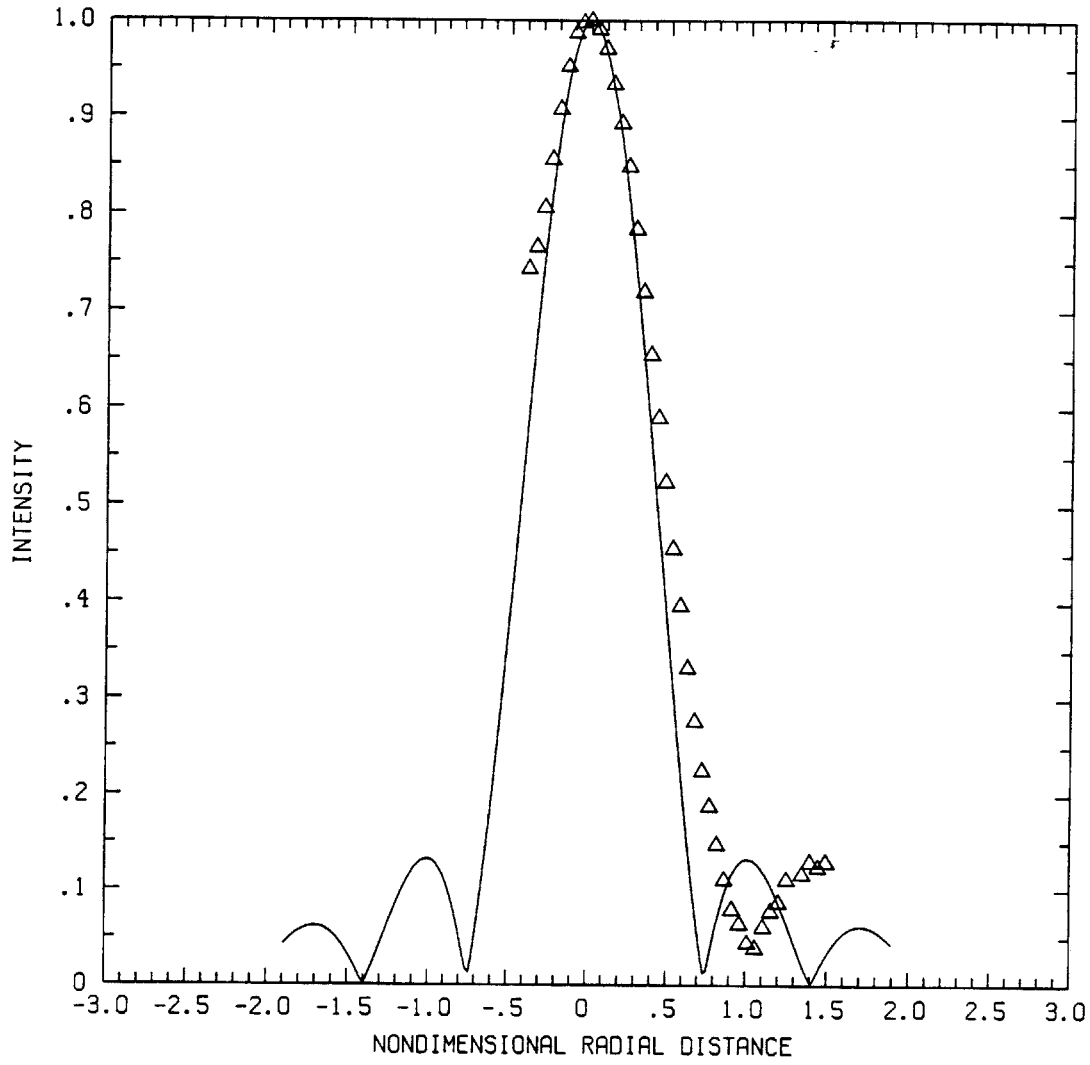
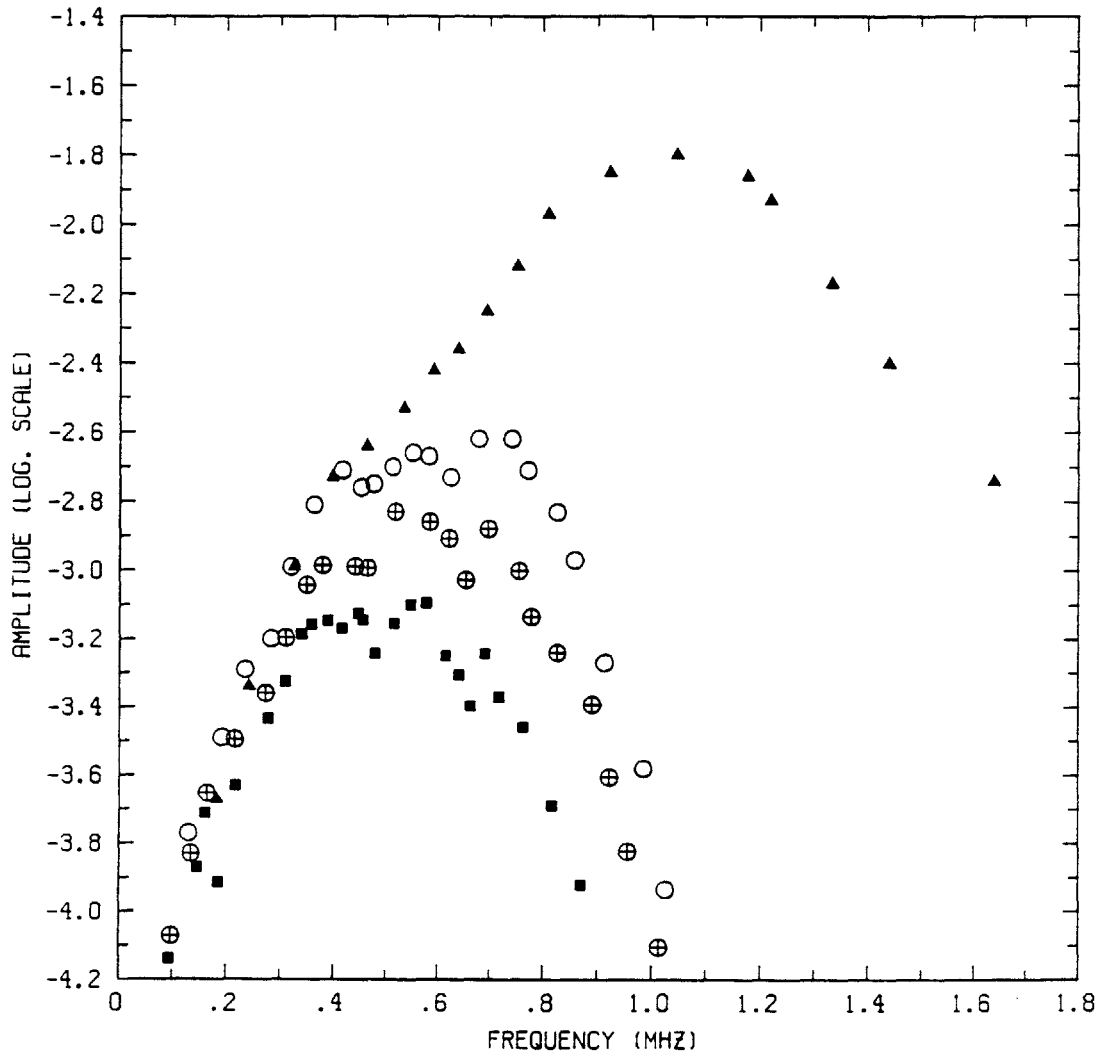
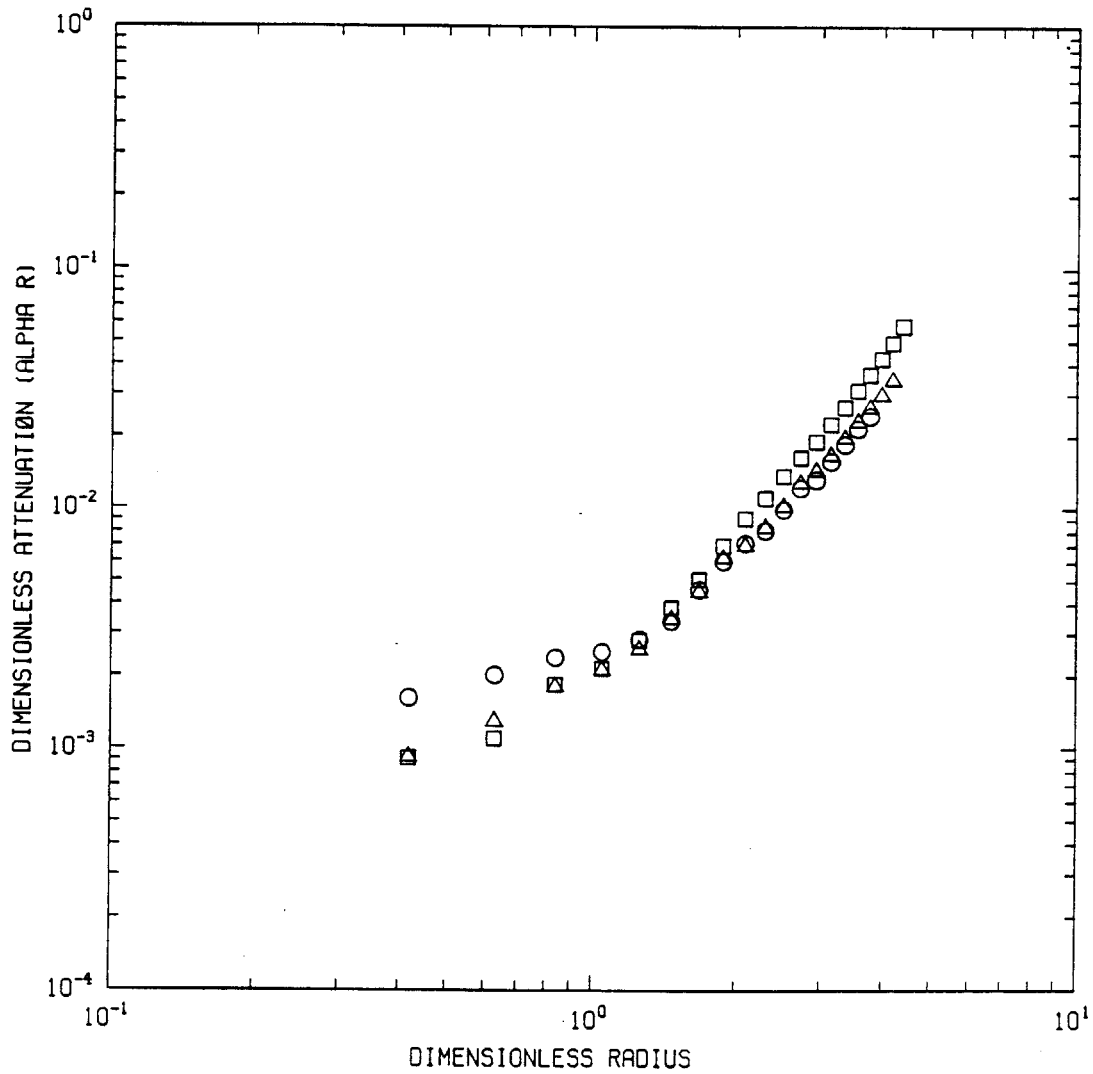


Figure 2.9b Radial intensity profile (as in Figure 2.9a) at 0.545 MHz.



**Figure 2.10** Typical unreduced data showing the attenuation as a function of frequency for pure water ( $\Delta$ ), and a packed bed mixture of 1.0 mm glass beads in water at 50 mm ( $O$ ), 75 mm ( $\oplus$ ) and 100 mm ( $\blacksquare$ ).



**Figure 2.11** Dimensionless representation of the attenuation data of Figure 2.10, showing  $(\alpha a)$  as a function of the reduced frequency  $(ka)$  for sound transmission in a bed of 1 mm silica beads in water for 50, 75 and 100 mm depths. At low frequencies, the attenuation appears to depend roughly on frequency to the first power, while the change in slope indicates a quadratic dependence on frequency for  $ka > 0.75$ .

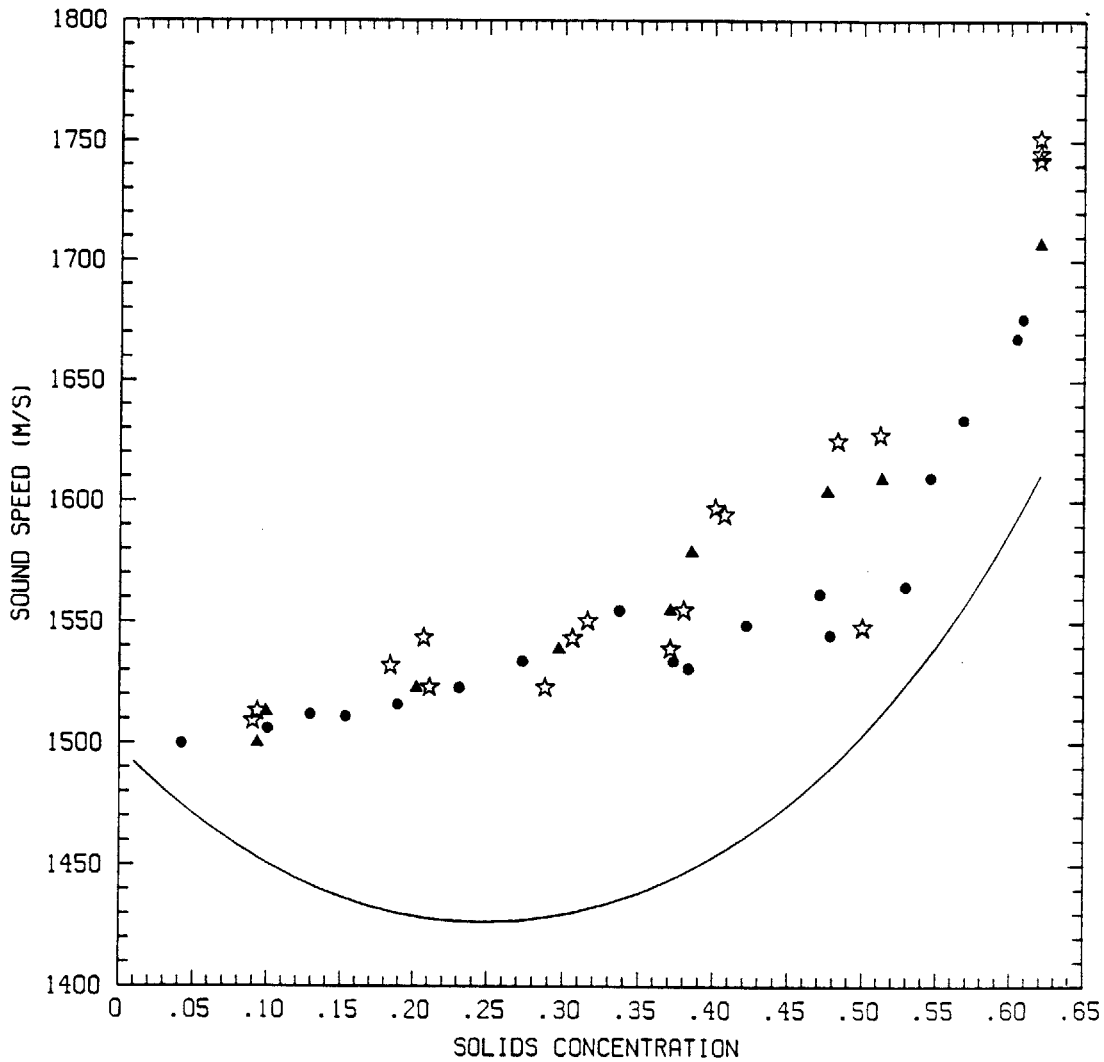


**Figure 2.12** Sound speed in a fluidized bed of 1.0 mm glass beads in water as a function of solids' fraction. The theoretical curve is the prediction using the phenomenological model of Urick (1947), outlined in Section 3.2. The experimental sound speed for  $ka \sim 1$ , in contrast, shows no minimum at intermediate concentrations, but quite significant deviation between experiments. The values of  $ka$  for the symbols are: ● 0.1, △ 0.5 and ★ 1.0.

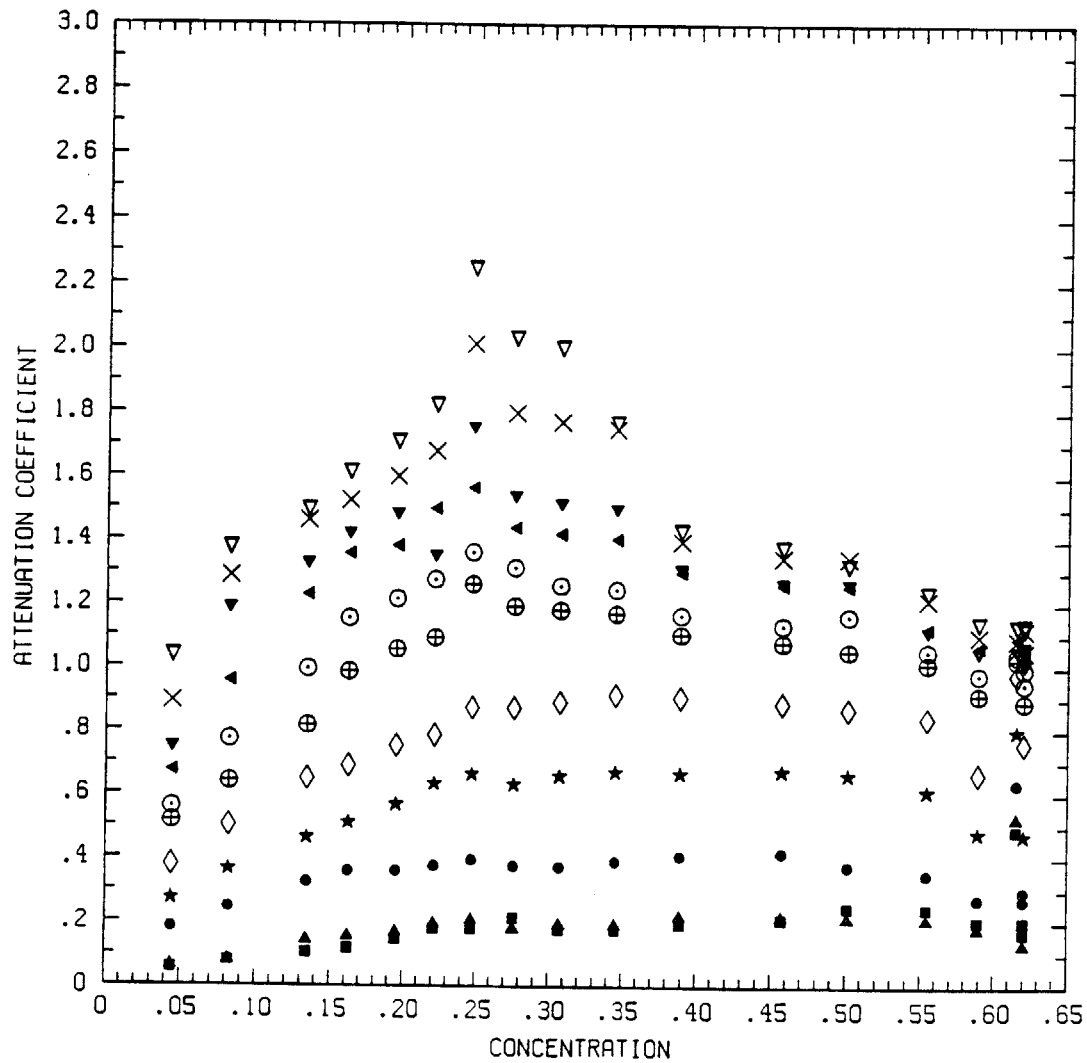


**Figure 2.13** Attenuation coefficient,  $\alpha$ , as a function of solids' concentration for sound transmission in a fluidized bed. The data range in frequency from 0.20 MHz (■ lowest attenuation) to 0.70 MHz (▽ highest attenuation) in 0.05 MHz steps. ◇ corresponds to  $ka \sim 0.9$ . This plot shows that there is a maximum in attenuation at a solids' concentration of about 30%, which is more pronounced at the higher frequencies.

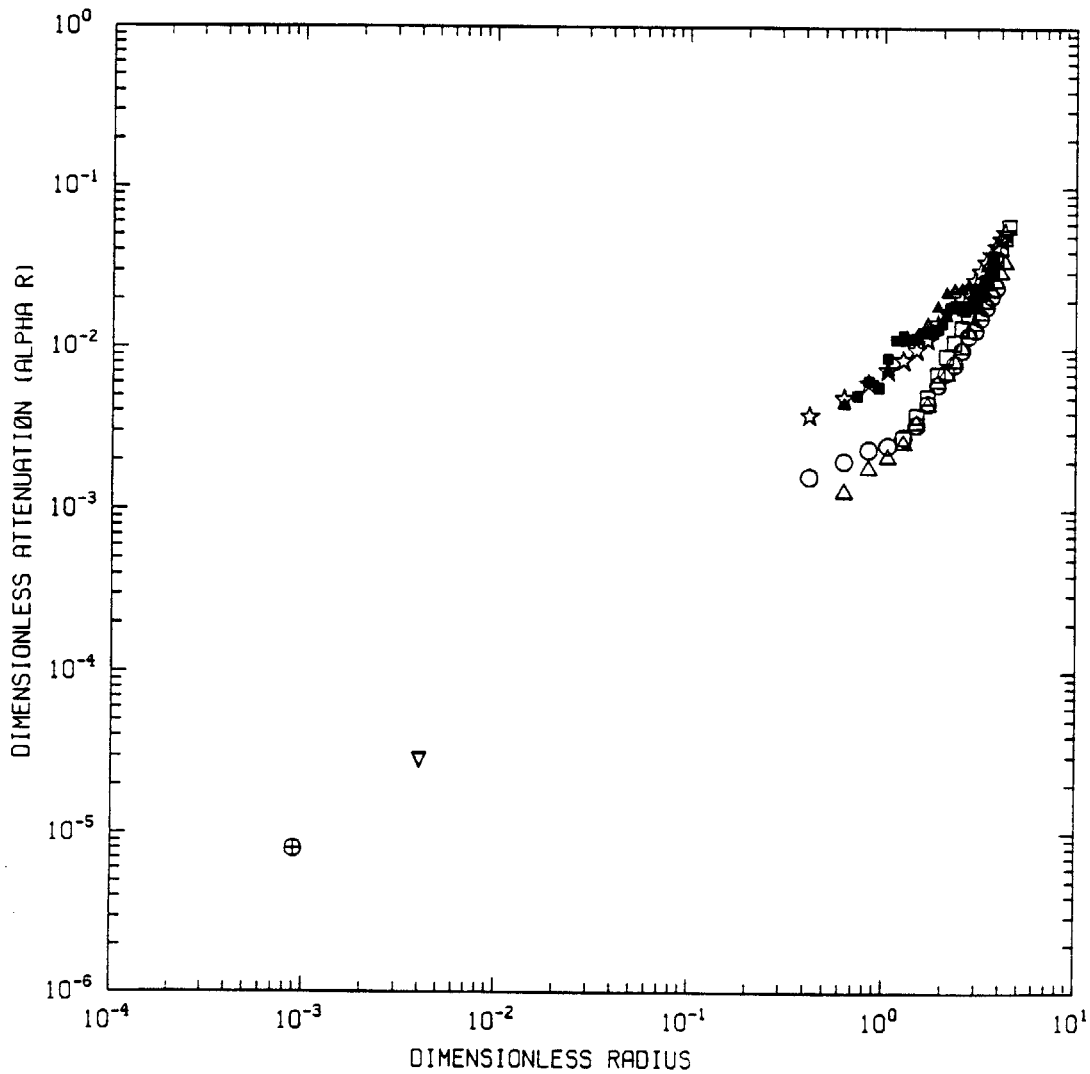


**Figure 2.14** Dimensionless representation of the attenuation at a solids' fraction of 30%, showing  $(\alpha a)$  as a function of the reduced frequency  $(ka)$ . This plot includes data from this study for 1.0 mm silica beads (o Δ □), 1.4 mm steel beads (■) and 1.2 mm zirconium oxide spheres (★), Urlick (1948) (▽), and Hampton (1967) (⊕), and shows the consistent scaling of  $\alpha a$  with  $ka$ .

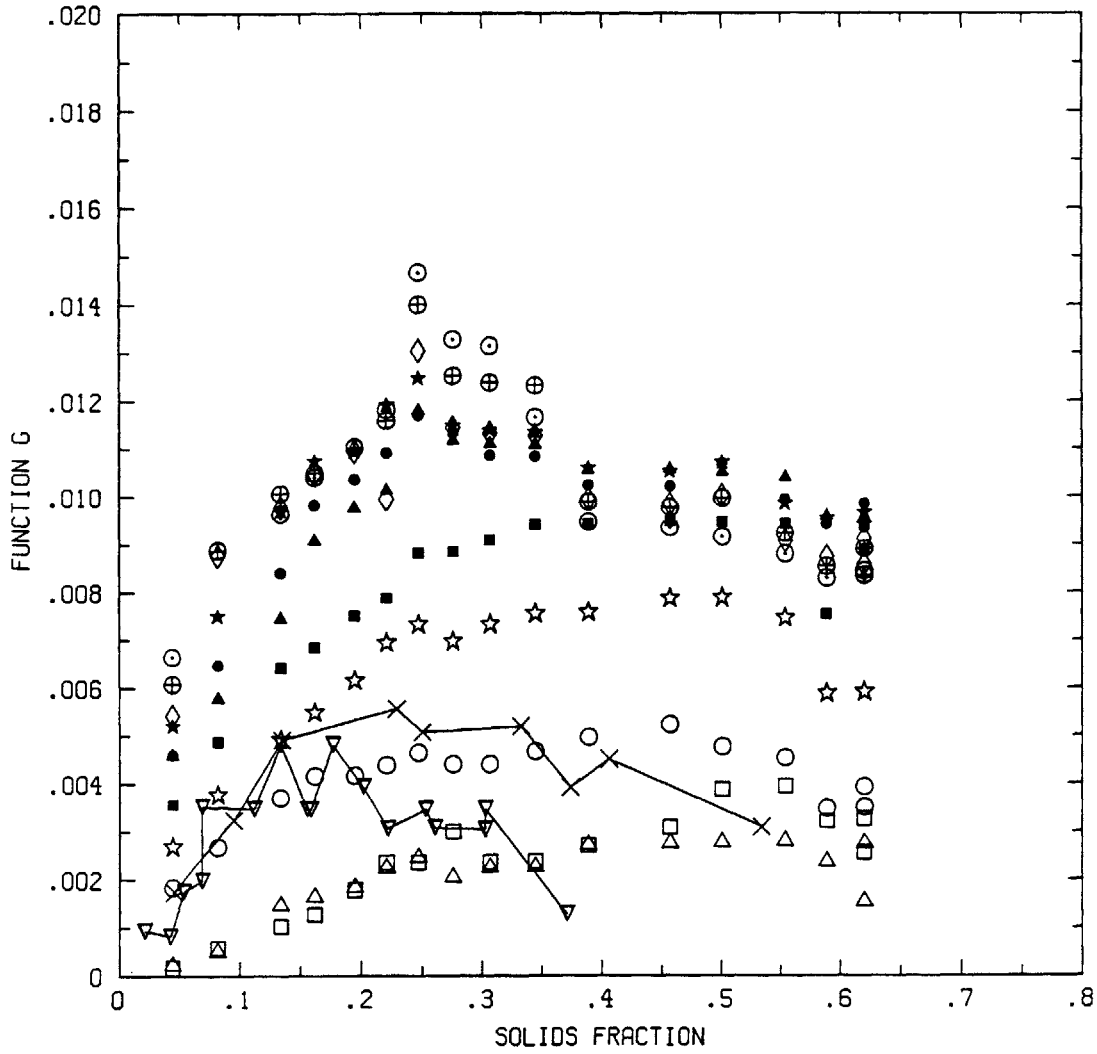


**Figure 2.15** The function  $g(\nu) = \frac{\alpha a}{ka}$  as a function of solids' fraction for varying frequency (0.20 MHz for the lowest points to 0.70 MHz for the highest). The joined data points are due to Urick (1948) ( $\nabla$ ) and Hampton (1967) (x).

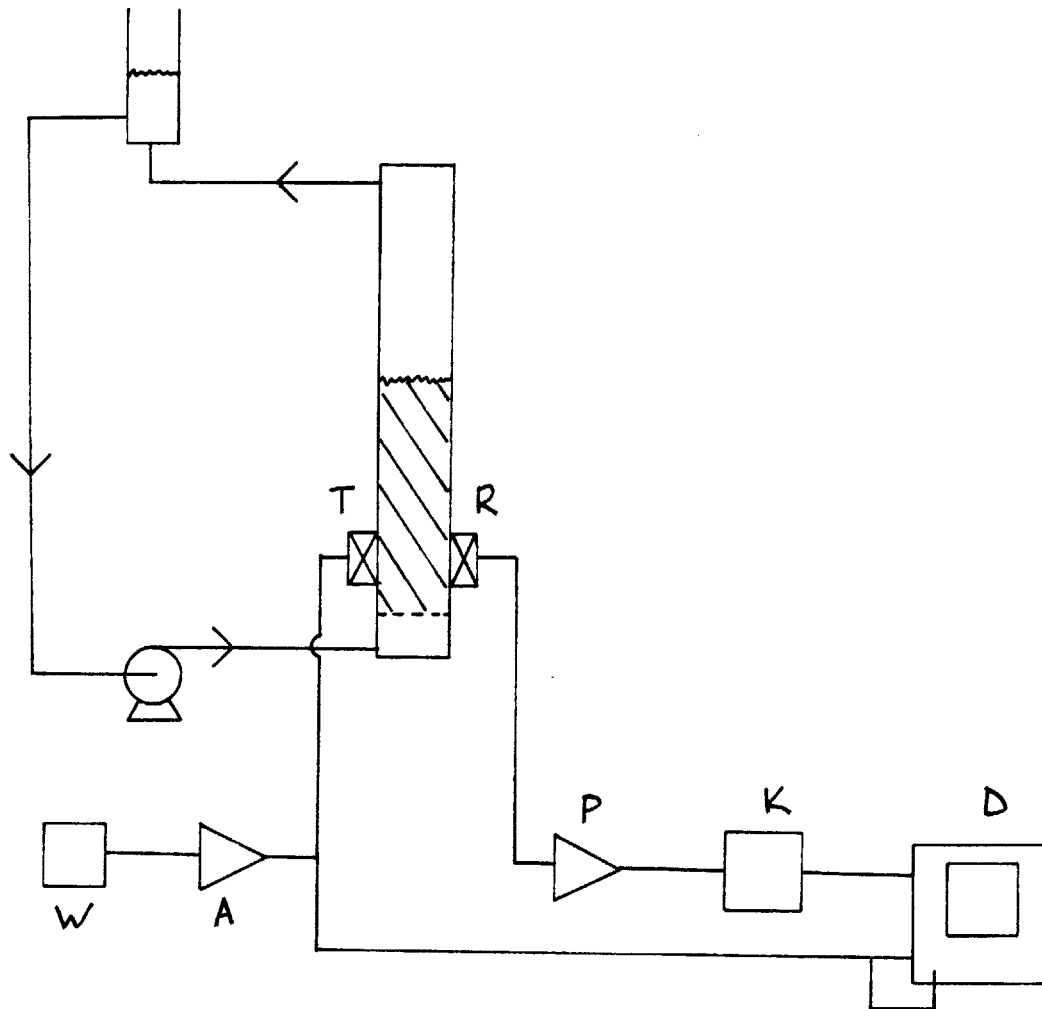


**Figure 2.16** Experimental fluidized bed apparatus for measuring the sound speed and attenuation in a suspension as a function of solids' concentration (determined by the average bed height). The transducer T transmits the signal from the function generator W amplified by the RF amplifier A. The signal received by the receiver R is amplified by the ultrasonic amplifier P and then low pass filtered (K). The transmitted and received signals are displayed on the digital oscilloscope D, which is triggered by the transmitted tone burst.

**CHAPTER 3**  
**ACOUSTIC WAVE PROPAGATION IN SUSPENSIONS**  
**— THEORY**

**3.1 Introduction**

Longitudinal acoustic waves travel through a single phase fluid with a velocity that depends predominantly on the fluid density and compressibility, and weakly on the viscosity. In suspensions and slurries, on the other hand, the wave speed is known to be dependent on the material properties of the two constituents as well as their relative concentrations. A simple phenomenological model for the speed of sound in a two phase mixture, first proposed by Urick (1947), describes the inhomogeneous mixture in terms of its averaged density and compressibility. This 'effective medium' model fits the available experimental data for the sound speed in suspensions very well for low non-dimensional acoustic wavenumbers  $ka = 2\pi a/\lambda$ , (where  $a$  is an average radius of the particles in the suspension) for which the propagation is practically non-dispersive. The attenuation of sound in two phase solid-liquid mixtures is known to increase with increasing frequency, but the dependence of attenuation on dispersed phase concentration is less well known. It has been found experimentally (as shown in Chapter 2) that the acoustic attenuation of high frequency sound in suspensions of small particles (corresponding to low values of  $ka$ ) is non-monotonic with respect to the concentration of solids in suspension - there is a distinct maximum in attenuation at an intermediate concentration between the dilute limit and the fully packed state (Urick, 1948; Hampton, 1967). This has important implications in the development of non-intrusive ultrasonic diagnostic techniques for the study of

concentrated sprays, slurries, pastes and fluidized beds, only to mention a few examples, which cannot readily be probed with existing optical methods. Few attempts have been made to explain this behavior (Gibson and Toksöz, 1989; Harker and Temple, 1988), and by their assumptions, these models are restricted to low  $ka$ . In addition, they employ empirically motivated forms for the effective viscosity of the suspension, and in the case of the former treatment, steady drag behavior. As an extension of this previous work the governing equations for the acoustics of suspensions are used to describe the counter-intuitive behavior of sound in the inertially dominated acoustic regime of considerably higher dimensionless frequency  $a\sqrt{\frac{\omega\rho_l}{\mu}}$  than that previously studied.

There is a large body of literature on the propagation of acoustic waves in porous media, which has been motivated by seismological, oil exploration and oceanographical interests. However, acoustic wave propagation in porous media and suspensions, while similar, have important differences. For example porous media exhibit elastic resistance to shear stresses (Biot, 1956) while a suspension typically does not. Both however can sustain isotropic stresses. One of the difficulties is in the representation of the relative motion between fluid and solids. This, in porous media is described in terms of a frequency dependent permeability, which has recently received attention (Attenborough, 1983, Johnson *et al.*, 1987): with a pore size,  $d$ , as a characteristic geometric length scale, if the viscous boundary layer thickness,  $\approx \sqrt{2\mu/\rho_l\omega}$  is significantly greater than  $d$ , the permeability scales with viscosity and equals its steady flow value. On the other hand if  $d \gg \sqrt{2\mu/\rho_l\omega}$ , the flow is essentially inviscid, is dominated by inertia and can be computed using potential theory. In the latter case, the dissipation is restricted to the thin boundary layer surrounding each particle. While similar scaling arguments can be made with suspensions, the analog of permeability is

inherently coupled with the motion of the particles and cannot be described with linear elasticity. Below, the general solution of the Navier-Stokes equations to the problem of a sphere oscillating at small amplitudes in a viscous fluid is generalized to accommodate oscillatory fluid motion, and it is included in the equations describing the acoustic behavior of a suspension. The sound speed and attenuation are then evaluated for the regime in which inertial effects dominate particle drag, and these predictions are then compared to experimental results.

### 3.2 Measurement of acoustic phase speed and attenuation

Results of the acoustic phase speed in suspensions reported by Hampton (1967) and Urick (1947, 1948) for  $ka \sim O(10^{-5})$  and  $O(10^{-4})$ , respectively, bear out the utility of the phenomenological approach for small  $ka$ . Here the wave speed  $c$  is given by

$$c = \sqrt{\frac{\kappa_{eff}}{\rho_{eff}}} \quad (3.1)$$

where the effective bulk modulus of the system is given by

$$\kappa_{eff} = \left[ \frac{\nu}{\kappa_s} + \frac{(1-\nu)}{\kappa_l} \right]^{-1}$$

and the suspension density is

$$\rho_{eff} = \nu\rho_s + (1-\nu)\rho_l. \quad (3.2)$$

For a system of silica particles in water, Equation (3.1) predicts a minimum in sound speed at a solids fraction of about 25 - 30%, and this prediction is borne out in the available experimental results at low  $ka$ , and hence low  $a\sqrt{\frac{\omega\rho_l}{\mu}}$ . Results obtained in the present study (Figure 3.1), however, show differing behavior. For

$ka \sim O(1)$ , there is no minimum at intermediate concentrations and the velocity increases monotonically with concentration.

The acoustic attenuation in concentrated suspensions is known to scale with the sound frequency, or in this case the non-dimensional wavenumber  $ka$  (Figure 2.13). In contrast to the sound speed results, the attenuation measured by Hampton (1967), Urick (1947, 1948) and in the present study shows consistently non-monotonic behavior as a function of solids fraction or dispersed phase concentration (Figure 3.2), albeit for  $ka$  spanning three to four orders of magnitude. A model is derived below to explain the respective behavior of attenuation and phase speed in suspensions for a wide range of  $ka$  (and  $a\sqrt{\frac{\omega\rho_l}{\mu}}$ ).

**Table 2:** Particle and Fluid Properties

Reference	Hampton (1967)	Urick (1948)	This study
Experimental System	kaolin/ water	kaolin/ water	silica/ water
Frequency	100 kHz	1 MHz	100 kHz - 1 MHz
Particle Radius	1.0 $\mu\text{m}$	0.5 $\mu\text{m}$	0.5 mm
$ka$	$\sim 6.66 \times 10^{-5}$	$\sim 3.35 \times 10^{-4}$	$\sim 0.2 - 0.6$
$a\sqrt{\frac{\omega\rho_l}{\mu}}$	$\sim 0.56$	$\sim 0.89$	$\sim 280 - 886$

### 3.3 Governing equations

A two component model for a suspension of monodisperse spheres in a Newtonian liquid is developed, and by performing a linear perturbation analysis, the expected infinitesimal compressional wave speed as well as the wave attenuation in the composite medium are derived.

The procedure for the formulation of the model is as follows: it is assumed that the solid particles as well as the liquid phase constitute a continuum. Once the two interacting continua assumption is made, a general continuity relation and a volume averaged momentum balance for each of the two phases may be written. Thereafter by invoking an equation of state for each phase, closure of the fluid dynamic equations is achieved.

For a solids fraction  $\nu$  of the total volume, the liquid phase continuity equation is

$$\frac{\partial(1-\nu)\rho_l}{\partial t} + \nabla[(1-\nu)\rho_l v_l] = 0 \quad (3.3)$$

where  $v_l$  is the liquid velocity. Similarly, the solid phase continuity equation takes the form

$$\frac{\partial\nu\rho_s}{\partial t} + \nabla[\nu\rho_s v_s] = 0 \quad (3.4)$$

In developing the momentum conservation equations for high frequency acoustics in a concentrated mixture, it is helpful to evaluate the relative importance of viscous and inertial effects. It is shown below that inertial effects dominate the interphase drag for the range of parameters of interest in the present study, *i.e.* large  $ka$ . For these the Reynolds number for oscillatory motion of a particle of radius  $a$  in a fluid of kinematic viscosity  $\frac{\mu}{\rho_l}$ ,

$$R = \sqrt{\frac{\rho_l \omega a^2}{2\mu}}, \quad (3.5)$$

is very high and it is evident therefore that the flow is essentially inviscid, with the exception of thin viscous boundary layers surrounding the particles. It is to these thin boundary layers that the viscous dissipation in the system is restricted. While they are specifically discussed below, the appropriate form of the one-dimensional momentum equations, neglecting gravitational effects, is:

$$\rho_s \nu \left[ \frac{\partial v_s}{\partial t} + v_s \frac{\partial v_s}{\partial x} \right] = F_{s,l} \quad \text{solids momentum} \quad (3.6)$$

$$\rho_l (1 - \nu) \left[ \frac{\partial v_l}{\partial t} + v_l \frac{\partial v_l}{\partial x} \right] = -\frac{\partial P}{\partial x} + F_{l,s} \quad \text{liquid momentum} \quad (3.7)$$

For the conditions of interest where the bulk of the fluid behaves in an inviscid manner, viscous dissipation beyond the particle boundary layers can be neglected, hence the absence of a  $\mu \nabla^2 v_l$  term. In this analysis, only viscous effects that arise due to interactions between the two phases are considered. In general, the momentum interaction force between the solid and the liquid,  $F_{s,l} = -F_{l,s}$ , consists of the dynamic drag (containing viscous and inertial effects) and buoyancy forces (see Section 3.3.1).

Equations 3.3, 3.4, 3.6 and 3.7 represent four equations in six unknowns,  $v_l, v_s, \rho_l, \rho_s, P$  and  $\nu$ . In order to achieve closure of this set of equations, two equations of state that relate the density variation of each of the two phases to the pressure perturbation,  $P'$ , are invoked, namely

$$\rho_l = \rho_l^0 \left[ 1 + \frac{P'}{\kappa_l} \right] \quad (3.8)$$

and

$$\rho_s = \rho_s^0 \left[ 1 + \frac{P'}{\kappa_s} \right]. \quad (3.9)$$

### 3.3.1 The interaction between the phases

The momentum interaction force between the solid and the liquid,  $F_{s,l} = -F_{l,s}$ , consists in general of dynamic drag (containing viscous and inertial effects) and buoyancy forces. In order to ascertain the momentum interaction force due to drag alone for a concentrated mixture, the result for the drag on a single particle

in an assembly of like particles must be extended to arbitrary concentrations. The analysis proceeds as follows: the drag on a single isolated particle (Section 3.3.2) is modified to give the drag on a single particle in an assembly of like particles (Section 3.3.3). This result is then scaled up to arbitrary concentrations to give the dynamic drag component of the momentum interaction force between the phases.

### 3.3.2 Drag on an isolated sphere

The unsteady drag force on a single isolated sphere (*i.e.* at infinite dilution) was derived by Landau and Lifshitz (1959) and this formulation is extended here for the case of particle and fluid motion:

$$F_D^{\nu \rightarrow 0} = 6\pi\mu a \left(1 + \frac{a}{\delta}\right) (v_s - v_l) + 3\pi a^2 \rho_l \left(\frac{2}{9}a + \delta\right) \frac{D(v_s - v_l)}{Dt} \quad (3.10)$$

where

$$\frac{D(v_s - v_l)}{Dt} = \left[\frac{\partial v_s}{\partial t} + v_s \frac{\partial v_s}{\partial x}\right] - \left[\frac{\partial v_l}{\partial t} + v_l \frac{\partial v_l}{\partial x}\right]. \quad (3.11)$$

The specific form of this time derivative satisfies the condition of objectivity (Drew, 1983). The parameter  $\delta$  ( $= \sqrt{2\mu/\rho_l\omega}$ ) is the unsteady viscous boundary layer thickness surrounding the particle. Its dimension relative to the separation between nearest neighbors provides a measure of the importance of viscous effects. At low frequencies,  $\delta$  is large, while the converse is true at high frequencies. For oscillatory, or harmonic, relative motion between the phases, where  $U_{rel} = v_s - v_l = U_0 e^{i\omega t}$ , the drag force is given by

$$\begin{aligned} F_D^{\nu \rightarrow 0} &= 6\pi\mu a U_{rel} \left[1 + a \sqrt{\frac{\rho_l}{2\mu}} \sqrt{\omega} + i \frac{a^2 \rho_l}{9\mu} \omega + i \frac{a \rho_l}{2\mu} \sqrt{\frac{2\mu}{\rho_l}} \sqrt{\omega}\right] \\ &= 6\pi\mu a U_{rel} \left[1 + a \sqrt{\frac{\rho_l}{2\mu}} \sqrt{\omega} + i a \sqrt{\frac{\rho_l}{2\mu}} \sqrt{\omega} + i \frac{a^2 \rho_l}{9\mu} \omega\right] \\ &= 6\pi\mu a U_{rel} \left[1 + \frac{a}{\delta} + i \frac{a}{\delta} + i \frac{2}{9} \frac{a^2}{\delta^2}\right] \end{aligned} \quad (3.12)$$

This implies that for  $\delta \gg a$ , or alternatively  $R \ll 1$ , the drag force reduces to the steady Stokesian drag, *i.e.* viscous forces dominate. On the other hand for large  $\omega$ , or  $\delta \ll a$ , the steady drag term becomes negligible compared to the dissipative term associated with the unsteady generation of vorticity in the boundary layer near the particle surface and its motion away from the particle surface. This latter limit shows the dominance of inertial forces (as manifested in the added mass term  $i\frac{2}{3}\frac{a^2}{\delta^2}$ ) over viscous forces in the interphase drag. As will be seen later, it is the history force terms in the drag expression (the terms  $\frac{a}{\delta}$  and  $i\frac{a}{\delta}$ ) that contribute most significantly to the attenuation of acoustic waves in suspensions at high frequencies.

To give an indication of the regime of validity of each of the terms in the equation above, for a 1 mm particle in water the crossover frequency at which the steady viscous drag term (*i.e.* the  $\omega^0$  term) equals the transition terms (these contain  $\delta^{-1}$ ) is 0.25 Hz. Correspondingly the second crossover frequency at which the  $\omega^1$  term (the inertial term) starts to dominate the drag is at about 18 Hz. From this the following asymptotic behavior can be recognized. At very low  $\omega$ , the expression reduces to the well known steady Stokes drag result,

$$F_D^{\nu \rightarrow 0} \stackrel{\text{lim}}{\omega \rightarrow 0} 6\pi\mu a(v_s - v_l) \quad (3.13)$$

and at high  $\omega$ , the dominant term is

$$F_D^{\nu \rightarrow 0} \stackrel{\text{lim}}{\omega \rightarrow \infty} \frac{1}{2}\rho_l \frac{4\pi a^3}{3} \frac{D(v_s - v_l)}{Dt}. \quad (3.14)$$

This latter equation be recognized as the added mass term for the drag on an isolated sphere where the added mass coefficient,  $C$  is  $\frac{1}{2}$ . So clearly for frequencies very much greater than the second cross-over frequency (say, for example >1 kHz) it would seem appropriate to use the inertial asymptotic behavior of the drag law.

However, while the drag becomes inertially dominated for high  $\omega$ , the dissipation associated with the particle and fluid oscillation remains viscous in origin but is restricted to a boundary layer surrounding each particle that becomes thinner with increasing frequency of oscillation. As is shown below, for the case of  $\omega > 100$  kHz, the terms that contain viscosity as a parameter have little effect on the sound speed, but do significantly affect the attenuation.

### 3.3.3 The added mass term and its dependence on concentration

Equation (3.10) may thus be represented as

$$F_D^{v \rightarrow 0} = 6\pi\mu a \left(1 + \frac{a}{\delta}\right) (v_s - v_l) + 3\pi a^2 \rho_l \left(\frac{4}{9} C a + \delta\right) \frac{D(v_s - v_l)}{Dt}. \quad (3.15)$$

It has long been recognized, however, that the added mass coefficient  $C$  associated with each sphere in a suspension is not a constant but is a function of concentration as well as the geometrical configuration of the suspension. By analogy, this dependence is directly related to Maxwell's relation for the effective conductivity of such an assembly of non-conducting spheres in a conducting fluid. This analogy is appropriate as Laplace's equation describes both the electrical potential equation and the potential flow equation in the two processes. Wallis (1989) showed that the relationship between the added mass coefficient and the normalized mixture conductivity is

$$C = \frac{1}{2\beta},$$

where  $\beta$  is the ratio of the liquid conductivity to that of the mixture. Maxwell (1881) obtained the following for the conductivity of a *random* assembly of non-conducting spheres

$$\beta = \frac{1 + \nu/2}{1 - \nu}, \quad (3.16)$$

which has been shown to be a good approximation up to maximum packing concentrations of mono-dispersed spheres (Turner, 1976). The added mass coefficient then is

$$C(\nu) = \frac{1 - \nu}{2 + \nu}, \quad (3.17)$$

which will be used in the momentum equation. It must be remembered here that this coefficient is very sensitive to the geometrical configuration (which explains the differences between existing models) and that this chosen representation is strictly valid for random distributions. The drag on a single particle in an assembly of like particles at a solids' fraction of  $\nu$  is thus

$$F_D^\nu = 6\pi\mu a \left(1 + \frac{a}{\delta}\right) (v_s - v_l) + 3\pi a^2 \rho_l \left(\frac{4}{9} C(\nu) a + \delta\right) \frac{D(v_s - v_l)}{Dt}. \quad (3.18)$$

### 3.3.4 The momentum interaction force

It is well known that for very low particle concentrations the drag on an assemblage of particle increases linearly with the solids' fraction; we assume here that linear superposition of the drag on a single particle in an assembly of similar particles  $F_D^\nu$  is appropriate up to maximum packing, or roughly 62 % by volume for monodisperse spheres. This in effect assumes an assembly of non-interacting particles as it neglects viscous interactions between adjacent particles. To extend the single particle drag result to higher concentrations, we assume that the equivalent drag per unit volume for the suspension  $F_{eq}$  is equal to the drag per sphere multiplied by the number of spheres per unit volume,  $n$ , or  $F_{eq} = n F_D^\nu$ . This result is an approximation and is tantamount to neglecting hindered settling effects in particle sedimentation — the non-linear viscous interactions between adjacent particles at high concentrations are neglected. It is known that the

solids' fraction, which is the volume of particles per unit total volume, is related to the number of particles per unit volume by

$$\nu = n \left( \frac{4\pi a^3}{3} \right).$$

Thus

$$n = \frac{3\nu}{4\pi a^3}. \quad (3.19)$$

As was mentioned previously, there is also a component of the phase interaction force which is due to the instantaneous pressure gradients. This buoyancy force is included in the momentum interaction force between the phases in the following manner

$$F_{ls} = \frac{3\nu F_D^\nu}{4\pi a^3} + \nu \frac{\partial P}{\partial x} \quad (3.20)$$

where  $F_D^\nu$  is the unsteady force on a single sphere of radius  $a$  in an assembly of like spheres executing oscillatory motion in a fluid, given in Section 3.3.3. This theory is valid in the limit that  $\delta \ll h/2$ , where  $h$  is the average inter-particle spacing and is thus strongly concentration dependent. Now from geometrical arguments  $h$  is given by

$$\frac{h}{a} = \frac{1 - \eta^{\frac{1}{3}}}{\eta^{\frac{1}{3}}}$$

where

$$\eta = \frac{\nu}{\nu_{max}}$$

and the maximum particle packing fraction  $\nu_{max} \simeq 0.635 \pm 0.005$  for a random close packed structure of monodisperse spheres and  $\nu_{max} \simeq 0.555$  for random loose packing (Onoda and Liniger, 1990).

The requirement for the particles in the suspension to be non-interacting is

$$\delta \ll h/2$$

which implies that the frequencies for which the present theory is valid are such that

$$\omega \gg \frac{4\mu}{a^2 \rho_l} \left[ \frac{\eta^{2/3}}{(1 - \eta^{1/3})^2} \right]. \quad (3.21)$$

The long wavelength assumption implicit in the continuum approximation in equations (3.4) and (3.6), places an upper bound on the frequencies for which this theory is valid. This assumption may be written

$$ka \ll 1$$

which implies

$$\omega \ll \frac{c}{a}.$$

For a system of 0.5 mm radius particles at maximum packing in water, this implies frequencies less than 525 kHz. The regime of  $\omega$  and  $\nu$  for which this restriction holds in a suspension of particles of radius 0.5 mm in water is shown in Figure 3.3.

### 3.3.5 Linearized Equations

It is assumed that the state variables  $v_l, v_s, P, \nu, \rho_l$  and  $\rho_s$  (denoted collectively by  $f = f^0 + f'$ ) are perturbed from their steady state values by some small amount. The frequencies of excitation of the particles in the fluid due to the acoustic wave propagation are high enough that the timescale of the duration of an individual wave or a series of waves is very much smaller than the timescale for any other fluctuation in the flow. This implies that the motion of the particle due to its oscillation in the sound wave may be completely decoupled from its gross motion in whatever flow situation is being considered, be it flow in a

pipeline or in a fluidized bed. The time averaged velocity of the particles and the liquid may be taken to be zero, or

$$v_l^0 = v_s^0 = 0.$$

Likewise, the datum pressure may be arbitrarily assumed to be zero or

$$P^0 = 0.$$

The state variables thus reduce to

$$\begin{pmatrix} v_l \\ v_s \\ P \\ \nu \\ \rho_l \\ \rho_s \end{pmatrix} = \begin{pmatrix} v_l' \\ v_s' \\ P' \\ \nu^0 + \nu' \\ \rho_l^0 + \rho_l' \\ \rho_s^0 + \rho_s' \end{pmatrix}. \quad (3.22)$$

The linearized perturbation equations are (to first order in the perturbed variables):

$$\frac{\partial(1-\nu^0)\rho_l'}{\partial t} - \frac{\partial\rho_l^0\nu'}{\partial t} + \frac{\partial(1-\nu^0)\rho_l^0v_l'}{\partial x} = 0 \quad (3.23)$$

$$\frac{\partial\nu^0\rho_s'}{\partial t} + \frac{\partial\rho_s^0\nu'}{\partial t} + \frac{\partial\nu^0\rho_s^0v_s'}{\partial x} = 0 \quad (3.24)$$

$$\rho_l^0(1-\nu^0)\left(\frac{\partial v_l'}{\partial t}\right) = -(1-\nu^0)\frac{\partial P}{\partial x} + \frac{9\mu\nu^0}{2a^2}\left(1+\frac{a}{\delta}\right)(v_s'-v_l') + \frac{9\nu^0}{4a}\rho_l'\left(\frac{2}{9}a+\delta\right)\left[\frac{\partial v_s'}{\partial t} - \frac{\partial v_l'}{\partial t}\right] \quad (3.25)$$

$$\rho_s^0\nu^0\left(\frac{\partial v_s'}{\partial t}\right) = -\nu^0\frac{\partial P}{\partial x} - \frac{9\mu\nu^0}{2a^2}\left(1+\frac{a}{\delta}\right)(v_s'-v_l') - \frac{9\nu^0}{4a}\rho_l'\left(\frac{2}{9}a+\delta\right)\left[\frac{\partial v_s'}{\partial t} - \frac{\partial v_l'}{\partial t}\right] \quad (3.26)$$

$$\rho_l' = \frac{\rho_l^0 P'}{\kappa_l} \quad (3.27)$$

$$\rho_s' = \frac{\rho_s^0 P'}{\kappa_s}. \quad (3.28)$$

### 3.4 Dispersion Relation

Wave-like solutions to these equations of the form

$$f' = f^0 e^{i(\omega t + kx)}$$

are sought, where

$$k = \frac{\omega}{c} + i\alpha,$$

$c$  is the wave speed in the medium and  $\alpha$  is the attenuation parameter. Substituting the perturbed variables into the full equations and neglecting terms higher than first order in the perturbation variables, we obtain the following matrix equation

$$[\mathbf{M}] \begin{pmatrix} v_l' \\ v_s' \\ P' \\ \nu' \\ \rho_l' \\ \rho_s' \end{pmatrix} = \mathbf{0} \quad (3.29)$$

where  $\mathbf{M} =$

$$\begin{pmatrix} -A - i\omega B & A + i\omega(B + \rho_s^0) & ik & 0 & 0 & 0 \\ A + i\omega(B + \rho_l^0 [\frac{1-\nu^0}{\nu^0}]) & -A - i\omega B & ik [\frac{1-\nu^0}{\nu^0}] & 0 & 0 & 0 \\ k\rho_l^0(1-\nu^0) & 0 & 0 & -\omega\rho_l^0 & \omega(1-\nu^0) & 0 \\ 0 & k\rho_s^0\nu^0 & 0 & \omega\rho_s^0 & 0 & \omega\nu^0 \\ 0 & 0 & -\frac{\rho_l^0}{\kappa_l} & 0 & 1 & 0 \\ 0 & 0 & -\frac{\rho_s^0}{\kappa_s} & 0 & 0 & 1 \end{pmatrix}$$

where

$$A = \frac{9\mu}{2a^2} \left(1 + \frac{a}{\delta}\right) \quad (3.30)$$

and

$$B = \rho_l \left[ C(\nu) + \frac{9\delta}{4a} \right]. \quad (3.31)$$

This implies that the column vector has a non-trivial solution if and only if

$$\det \mathbf{M} = 0$$

which in turn for the above case implies that

$$k^2 = -\omega^2 \left[ \frac{\nu}{\kappa_s} + \frac{(1-\nu)}{\kappa_l} \right] \frac{((1-\nu)\rho_l(A + i\omega B + i\omega\rho_s) + \nu\rho_s(A + i\omega B))}{A + i\omega((1-\nu)^2\rho_s + \nu(1-\nu)\rho_l + B)}. \quad (3.32)$$

The wavespeed  $c$  is given by

$$c = \frac{\omega}{\Re(k)} \quad (3.33)$$

and the attenuation

$$\alpha(\omega) = \Im(k). \quad (3.34)$$

## 3.5 Results

### 3.5.1 Sound Speed

The sound speed is given by

$$c = \left[ \frac{\frac{A^2}{\rho_l^2} + \omega^2(G(\nu))^2}{\rho_l \left[ \frac{\nu}{\kappa_s} + \frac{(1-\nu)}{\kappa_l} \right] \left[ \frac{A^2 \rho_s^*}{\rho_l^2} + \omega^2 G(\nu)(B^* \rho_s^* + D(1-\nu)) \right]} \right]^{\frac{1}{2}} \quad (3.35)$$

where

$$\begin{aligned} \frac{A}{\rho_l} &= \frac{9\mu}{2a^2\rho_l} \left(1 + \frac{a}{\delta}\right) = \frac{9\mu}{2a^2\rho_l} (1 + R) \\ B^* &= \frac{B}{\rho_l} = C(\nu) + \frac{9}{4} \frac{\delta}{a} = C(\nu) + \frac{9}{4} \frac{1}{R} \end{aligned}$$

$$D = \frac{\rho_s}{\rho_l}$$

$$\rho^* = (1 - \nu) + \nu D$$

and

$$G(\nu) = (1 - \nu)\rho^* + B^*.$$

The sound speed can be seen to be dependent on the frequency of the acoustic wave and hence the parameters  $ka$  and  $R$ , through the terms  $A$  and  $B^*$ , which involve the unsteady boundary layer thickness  $\delta$ .

The low frequency limit for the sound speed as predicted by the two component model is given by

$$c \underset{\omega \rightarrow 0}{\overset{lim}{\approx}} \left[ \frac{1}{\left[ \frac{\nu}{\kappa_s} + \frac{(1-\nu)}{\kappa_l} \right] \rho_l (1 - \nu + \nu D)} \right]^{\frac{1}{2}} \quad (3.36)$$

which is entirely independent of the frequency and material properties other than the fluid and solid densities and compressibilities. In the limit that  $ka \rightarrow 0$  or  $R \rightarrow 0$ , the sound speed as a function of  $ka$  reduces to that predicted by the phenomenological model of Urlick (1947) (Figure 3.4). In addition, the low frequency expression has the expected behavior for the high and low concentration limits: for  $\nu \rightarrow 0$ , or pure fluid, the velocity tends to that of the single phase fluid,

$$c = \left[ \frac{\kappa_l}{\rho_l} \right]^{\frac{1}{2}}. \quad (3.37)$$

The high frequency limit for the sound speed is given by

$$c \underset{\omega \rightarrow \infty}{\overset{lim}{\approx}} \left[ \frac{(1 - \nu)\rho^* + C(\nu)}{\left[ \frac{\nu}{\kappa_s} + \frac{(1-\nu)}{\kappa_l} \right] \rho_l (C(\nu)\rho^* + D(1 - \nu))} \right]^{\frac{1}{2}} \quad (3.38)$$

which is independent of frequency and hence  $ka$  and  $R$ , but is quite strongly dependent on the added mass coefficient  $C(\nu)$ . The phase velocity of a compressional wave in a suspension as defined by Equation (3.35) is compared with

available data for a range of  $ka$  in Figure 3.5. For  $ka \sim O(1)$  which is of interest in this study, the sound speed profile can be seen to be somewhat different to the low frequency case, and does not show a minimum at intermediate concentrations, but rather increases monotonically with increasing solids fraction. The difference in the behavior of  $c$  across four orders of magnitude of  $ka$  is not large, and the sound speed thus shows a relative insensitivity to frequency and all other factors except the fluid and particle densities and compressibilities.

### 3.5.2 Attenuation

The attenuation of an acoustic wave propagating in a suspension is given by

$$\alpha(\omega) = \left[ \frac{\left[ \frac{\nu}{\kappa_s} + \frac{(1-\nu)}{\kappa_l} \right] \omega^3 \frac{A}{\rho_l} (1-\nu) (\rho^* \hat{\rho} - D)}{\left( \frac{A}{\rho_l} \right)^2 + \omega^2 (G(\nu))^2} \right]^{\frac{1}{2}} \quad (3.39)$$

where

$$\hat{\rho} = \nu + (1-\nu)D$$

The low frequency limit for the attenuation as predicted by the two component model is given by

$$\alpha \underset{\omega \rightarrow 0}{\overset{\text{lim}}{\approx}} \left[ \frac{\left[ \frac{\nu}{\kappa_s} + \frac{(1-\nu)}{\kappa_l} \right] \omega^3 (1-\nu) (\rho^* \hat{\rho} - D)}{\left( \frac{A}{\rho_l} \right)} \right]^{\frac{1}{2}} \quad (3.40)$$

and is therefore proportional to  $\omega^{\frac{3}{2}}$  as  $\frac{A}{\rho_l} \rightarrow \frac{9}{2} \frac{\mu}{a^2 \rho_l}$  for  $ka \rightarrow 0$ . The term dominating the drag on the particles at the low frequency limit is the steady Stokesian drag, and it is this term that predominates in the attenuation expression as well.

At high frequencies the attenuation is given by

$$\alpha \underset{\omega \rightarrow \infty}{\overset{\text{lim}}{\approx}} \left[ \frac{\left[ \frac{\nu}{\kappa_s} + \frac{(1-\nu)}{\kappa_l} \right] \omega \frac{A}{\rho_l} (1-\nu) (\rho^* \hat{\rho} - D)}{\left( (1-\nu) \rho^* + C(\nu) \right)^2} \right]^{\frac{1}{2}} \quad (3.41)$$

and  $\frac{A}{\rho_l} \rightarrow \frac{9}{2} \frac{\mu}{a \rho_l} \frac{1}{\delta}$  as  $ka \rightarrow \infty$ , or  $R \rightarrow \infty$ . This leads to the result that the attenuation at high frequencies is proportional to  $\mu^{\frac{1}{2}} \omega^{\frac{3}{4}}$ . As  $\mu \rightarrow 0$ , the attenuation tends to zero, which is to be expected as the dissipation is purely viscous in nature. However, it should be noted that for high values of  $ka$  the chief attenuation mechanism is not viscous forces arising from the steady or Stokesian drag, but viscous interactions due to the Basset or history terms that dominate the particle drag at high frequencies of oscillation.

There are few reported sets of data in the literature that show attenuation in suspensions, as opposed to porous media. As it can be seen, the data that is available show a distinct maximum at intermediate concentrations, and this result is borne out in the simulations. The data of Hampton (1967) are for  $ka \simeq 6.66 \times 10^{-5}$  (Figure 3.6) and that of Urick (1948) are for  $ka \simeq 3.4 \times 10^{-4}$  (Figure 3.7), while the data of the present study correspond to  $ka \simeq 0.2 - 0.6$  (Figure 3.8). The present calculations show the dependence of the attenuation on concentration and frequency for the range of dynamic particle Reynolds number  $R$ , which had essentially been overlooked by these previous studies.

### 3.6 Discussion

A consistent physical argument to describe acoustic wave propagation in suspensions has been presented and its agreement with experimental results spanning a range of the non-dimensional wavenumber  $ka$  of approximately four orders of magnitude has been shown. It has been shown that the attenuation of acoustic waves propagating in a suspension of monodisperse spheres in a viscous fluid at high frequency is primarily due to the Basset or history forces exerted on the oscillating particles by the fluid. At low frequencies of oscillation corresponding

to large boundary layer thicknesses relative to the particle radius, the chief attenuation mechanism is steady or Stokesian drag on the particles and  $\alpha \sim \mu^{-\frac{1}{2}}\omega^{\frac{3}{2}}$ . In contrast to its effect on the attenuation, the effect of varying  $ka$  on the speed of sound of the propagating wave is small.

Predictions of the attenuation of sound in porous media using Biot's theory (1956) give the attenuation in the high frequency limit proportional to  $\mu^{\frac{1}{2}}\omega^{\frac{1}{2}}$ , whereas it is found here that for the case of a suspension that the attenuation scales as  $\mu^{\frac{1}{2}}\omega^{\frac{3}{4}}$  (Figure 3.9). Indeed, Salin and Schön (1981) have found experimentally that for the attenuation of sound in a packed bed of spheres in water increases at a rate "between  $\sqrt{\omega}$  and  $\omega$ ".

As has been noted, for large  $ka$  the present theory predicts that the attenuation varies almost linearly with frequency. However at a  $ka$  of about unity, it has been found experimentally that the attenuation becomes non-linear and apparently quadratic in frequency (Figure 3.10). This is probably due to multiple scattering effects which are known to dominate the attenuation behavior of suspensions at high frequencies (Allegra and Hawley, 1971; Waterman and Truell, 1961). Multiple scattering effects are also known to occur in porous media at  $kd \sim 1$  where  $d$  is some representative pore size (Salin and Schön, 1981). However, for all  $ka$  up to  $\sim O(1)$  the primary attenuation mechanism for acoustic wave propagation in a particulate suspension appears to be viscous interactions due to steady drag and Basset or history forces between the oscillating fluid and the particles.

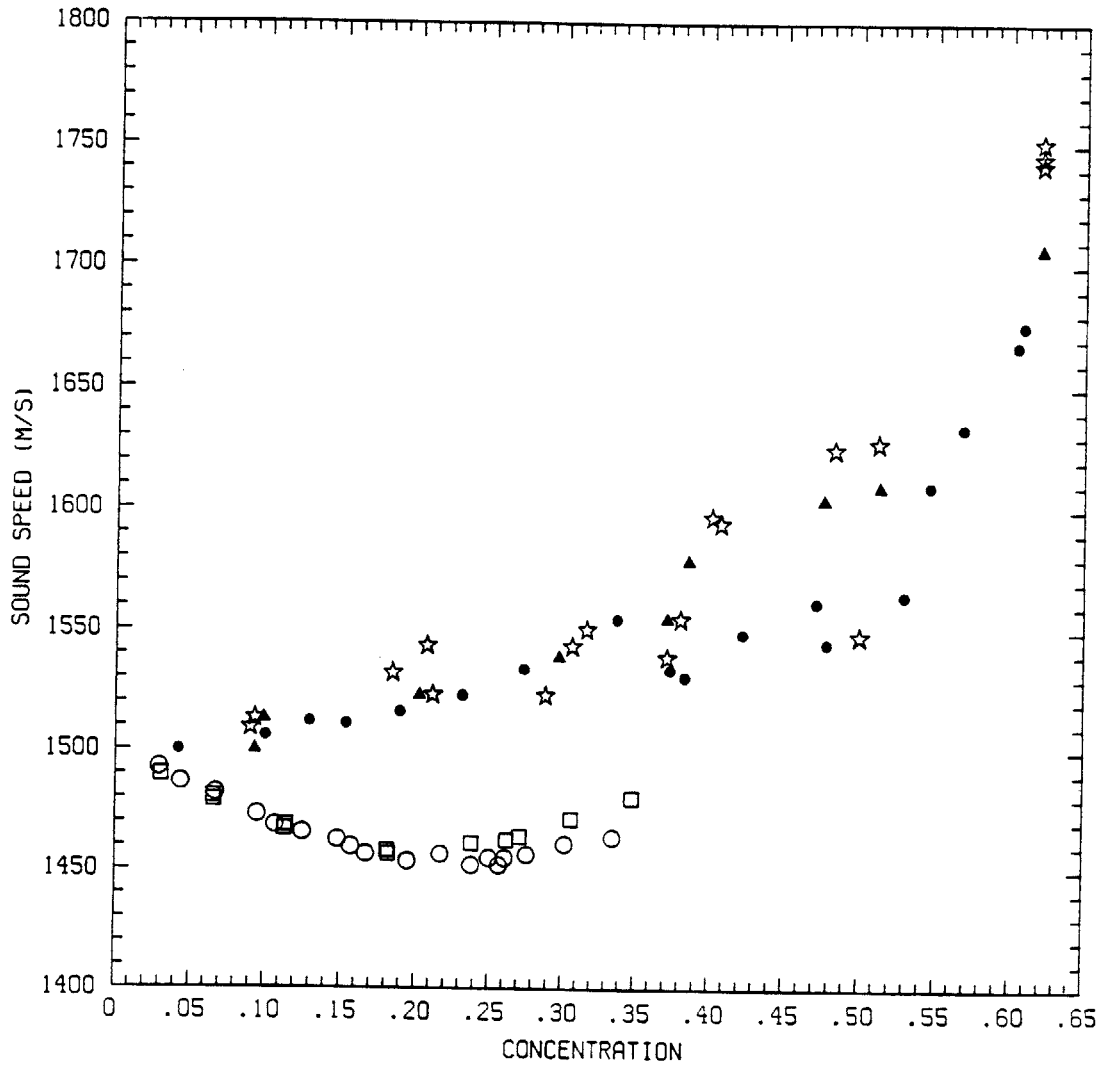


**Figure 3.1:** The variation of sound speed in a suspension with particle concentration. The data of Hampton (1967) (o) are for  $ka \simeq 6.66 \times 10^{-5}$  ( $R \simeq 0.40$ ) and that of Urick (1948) (□) are for  $ka \simeq 3.4 \times 10^{-4}$  ( $R \simeq 0.63$ ). The data of this study corresponding to  $ka \simeq 0.2 - 0.6$  ( $R \simeq 200 - 625$ ), show some scatter due to concentration fluctuations about the measured mean, but no minimum at intermediate solids fractions.

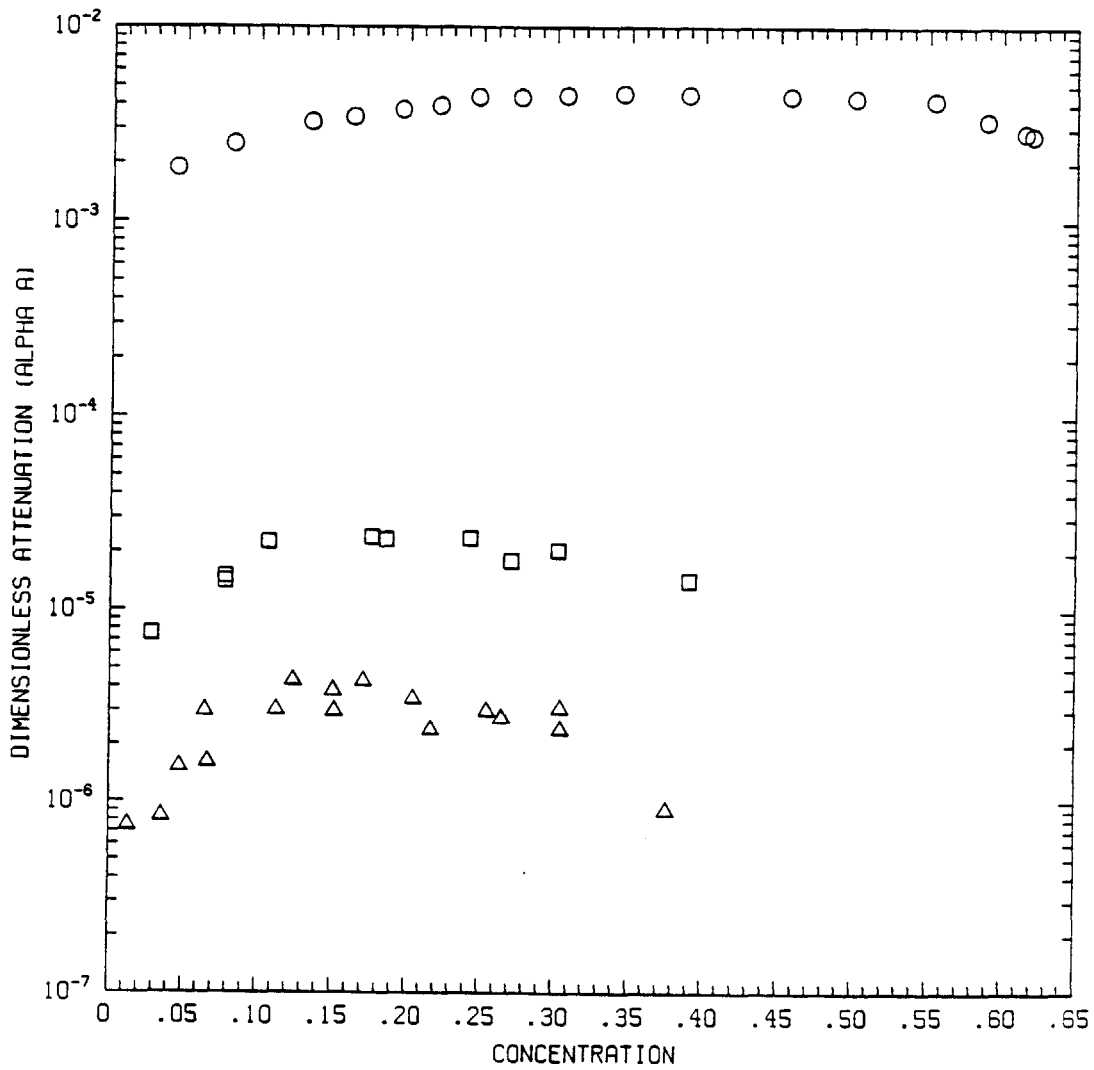


**Figure 3.2:** Dimensionless representation of the acoustic attenuation  $\alpha a$  as a function of  $ka$  at a solids fraction of 30% ( $\Delta$ : Hampton (1967),  $\square$ : Urick (1948),  $o$ : this study). The data shows distinct maxima at intermediate concentrations and the persistence of this behavior over four orders of magnitude of  $ka$ .

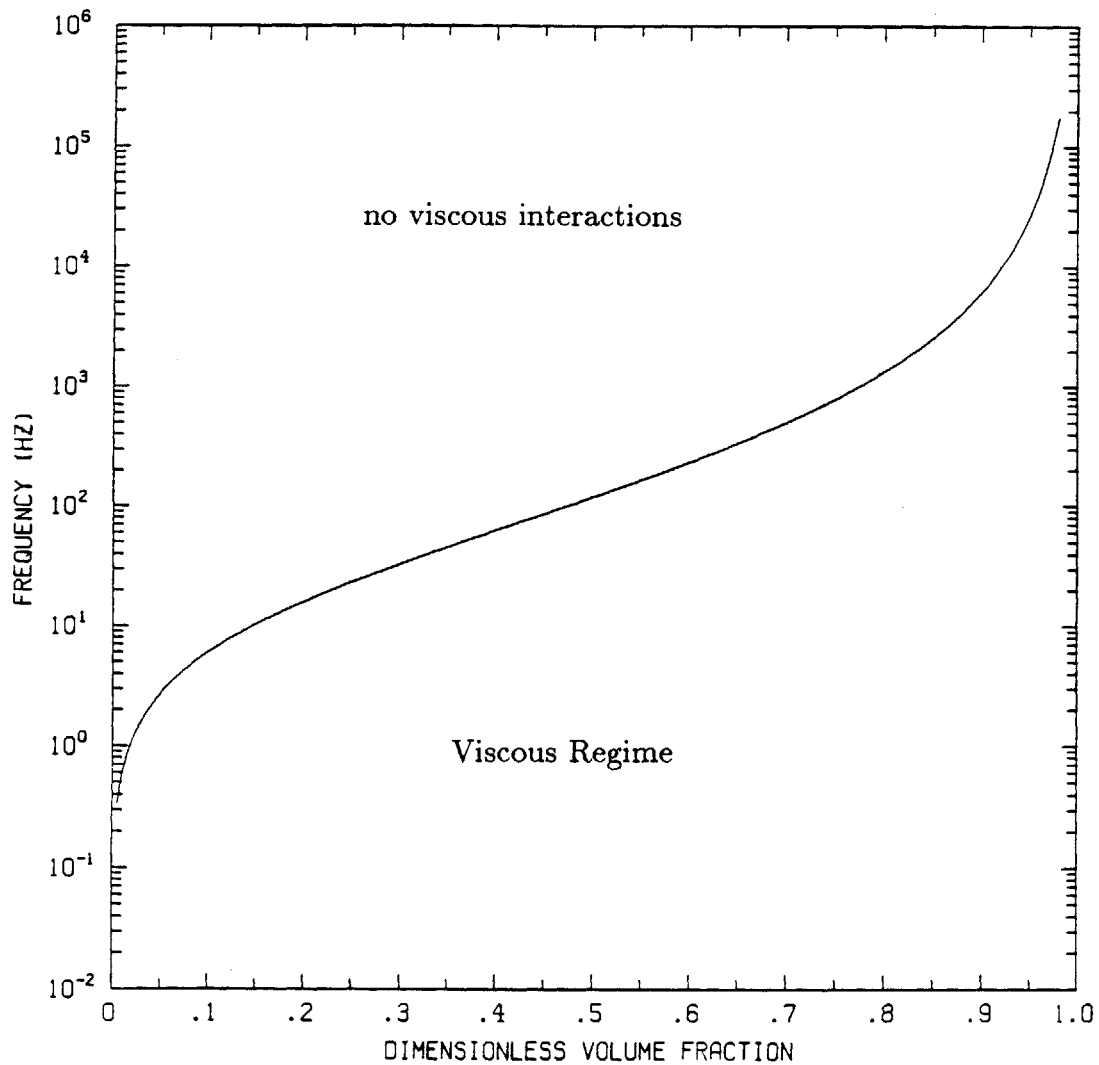


**Figure 3.3:** Regime map of the range of frequencies for which the assumption of non-interacting particles is valid. For frequencies above the theoretical curve (Equation 3.21), the 0.5 mm radius particles (in water) may be considered to have non-overlapping viscous boundary layers.

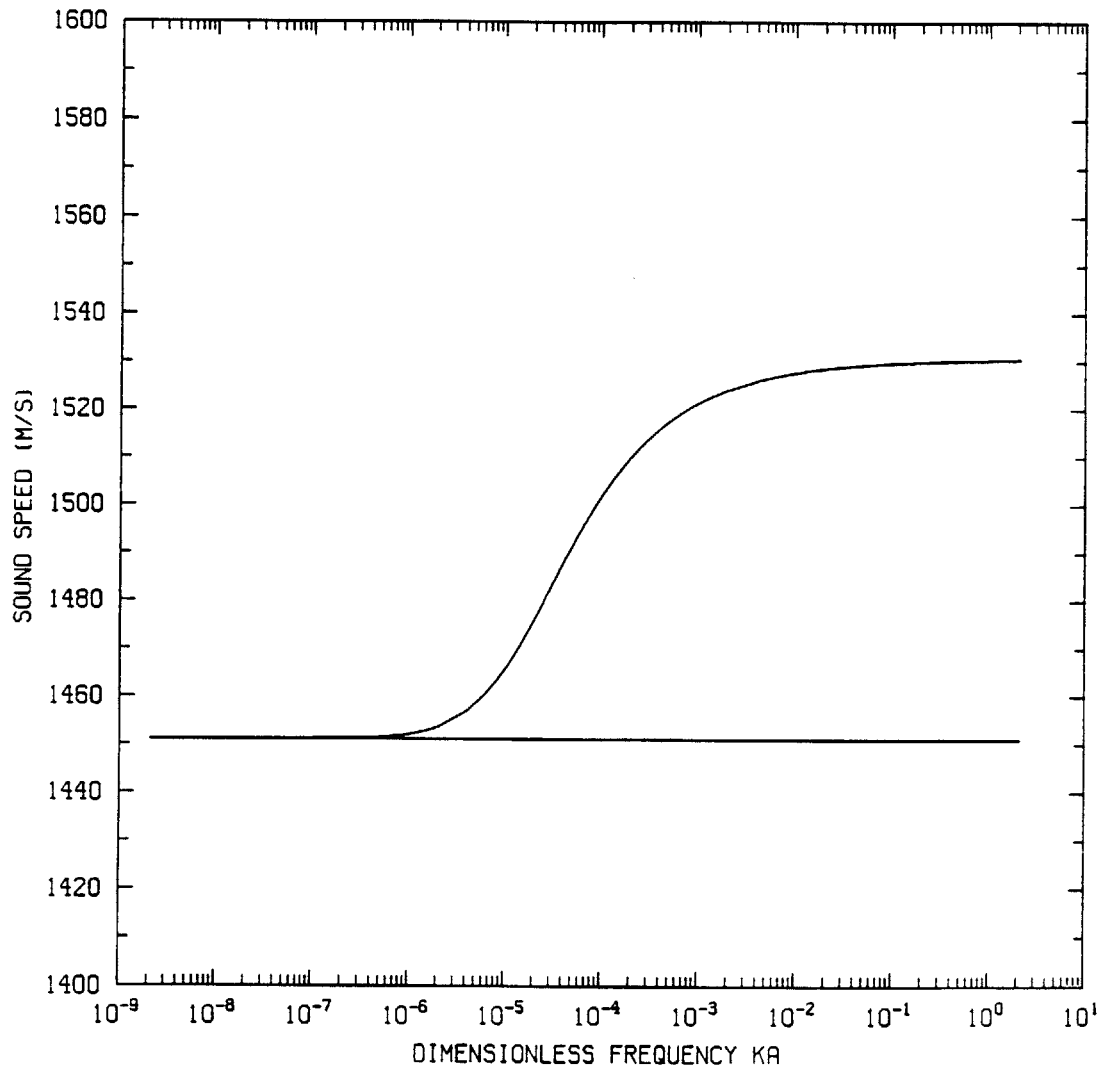


**Figure 3.4:** Predicted sound speed as a function of  $ka$  for 1.0 mm diameter silica particles in water at a concentration of 30% (from Equation 3.35). For  $ka \rightarrow 0$  ( $R \rightarrow 0$ ), the sound speed tends to the prediction of the phenomenological model of Urick (1947), and for  $ka > 0.1$  the sound speed asymptotes to a value somewhat greater than the speed in pure water. The cross-over frequency is seen to be in the region of  $ka \sim 10^{-4}$ .

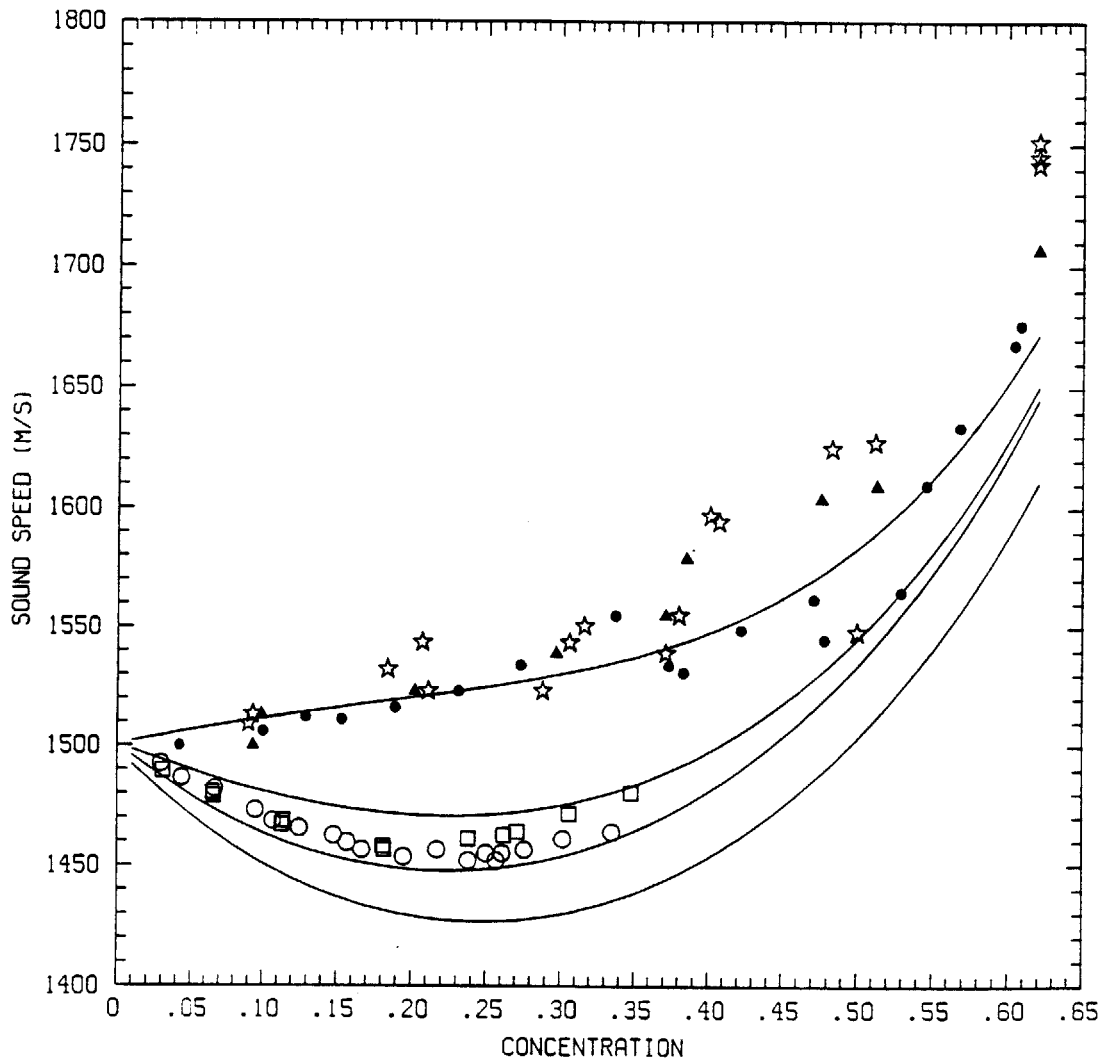


**Figure 3.5:** The sound speed predictions of Equation 3.35 compared to the available data. The data is as in Figure 3.1. The theoretical curves are (from bottom to top) for  $ka \sim 0, 6.66 \times 10^{-5}, 3.4 \times 10^{-4}$  and 0.5.

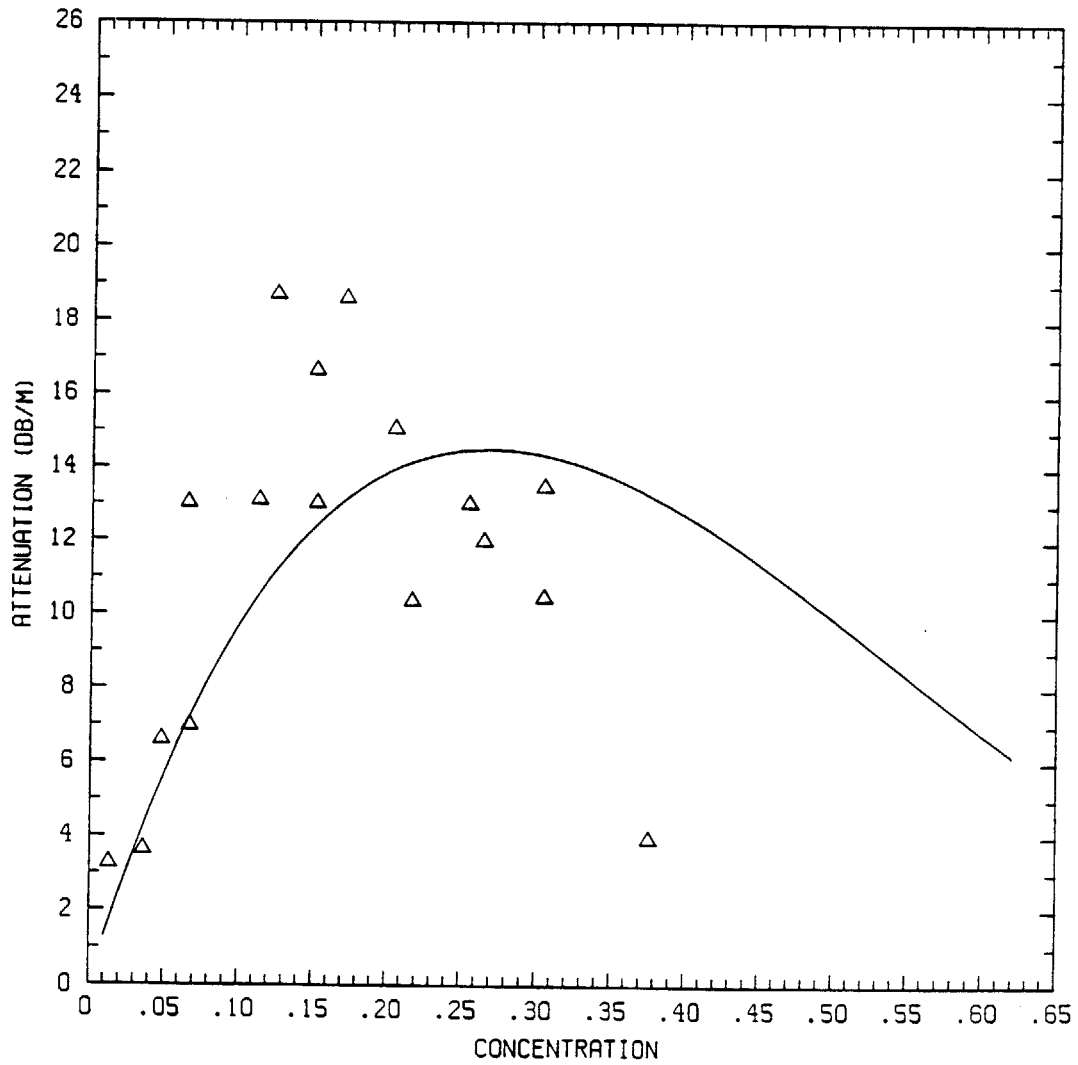


**Figure 3.6:** Attenuation (in dB/m) as a function of solids fraction for  $1.0\mu\text{m}$  radius kaolinite particles in water at a frequency of 100 kHz (Hampton, 1967), compared to the theoretical prediction of Equation 3.39.

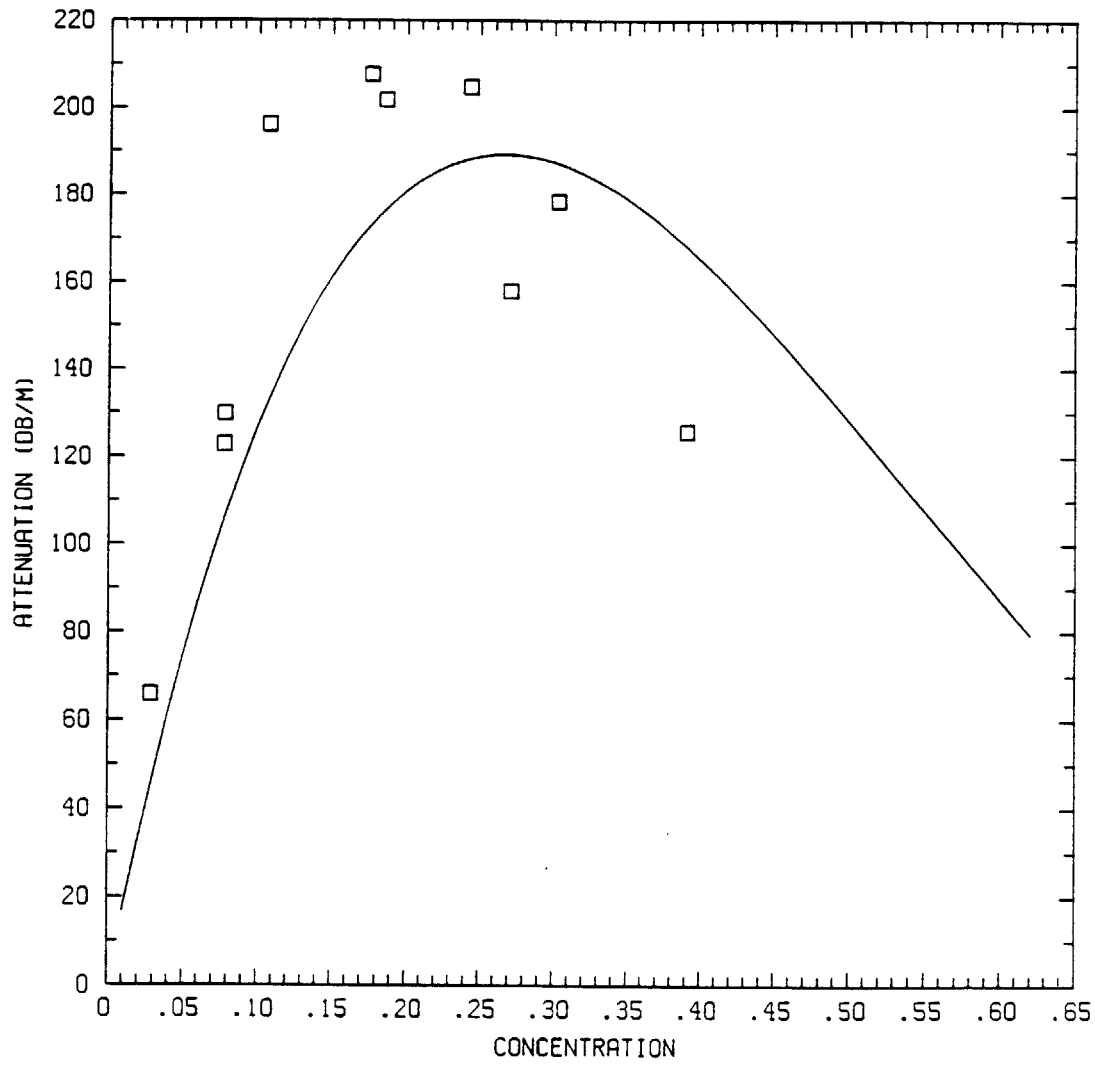


**Figure 3.7:** Attenuation (in dB/m) as a function of solids fraction for  $0.5 \mu\text{m}$  radius kaolinite particles in water at a frequency of 1 MHz (Urick, 1948), compared to the theoretical prediction of Equation 3.39.

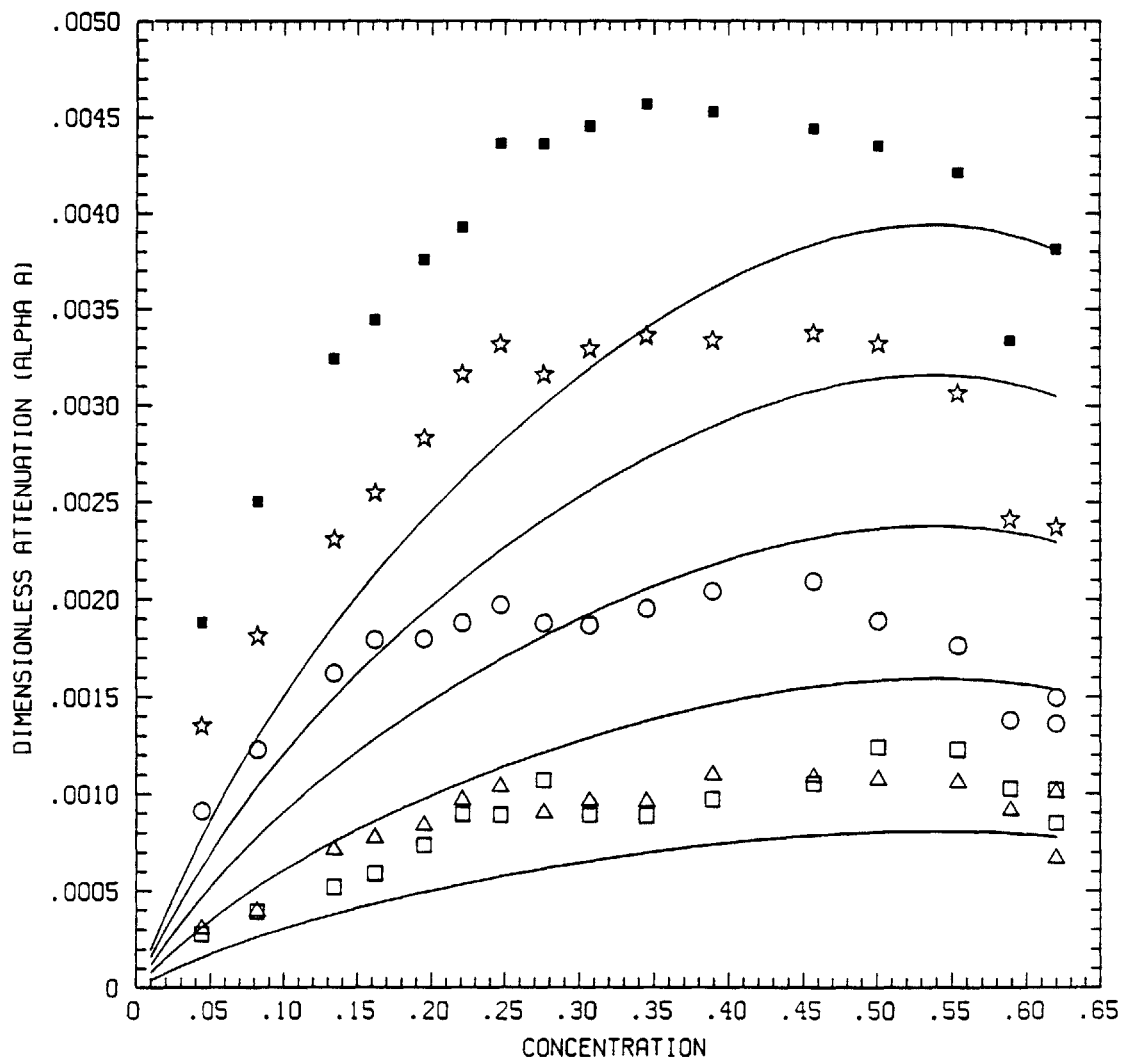


**Figure 3.8:** Dimensionless attenuation  $\alpha a$  for acoustic wave propagation in a suspension of 0.5 mm radius silica particles in water as a function of solids concentration. The theoretical curves and data from Equation (3.39) are for (from bottom to top)  $ka = 0.52, 0.62, 0.73, 0.84, 0.94$ .

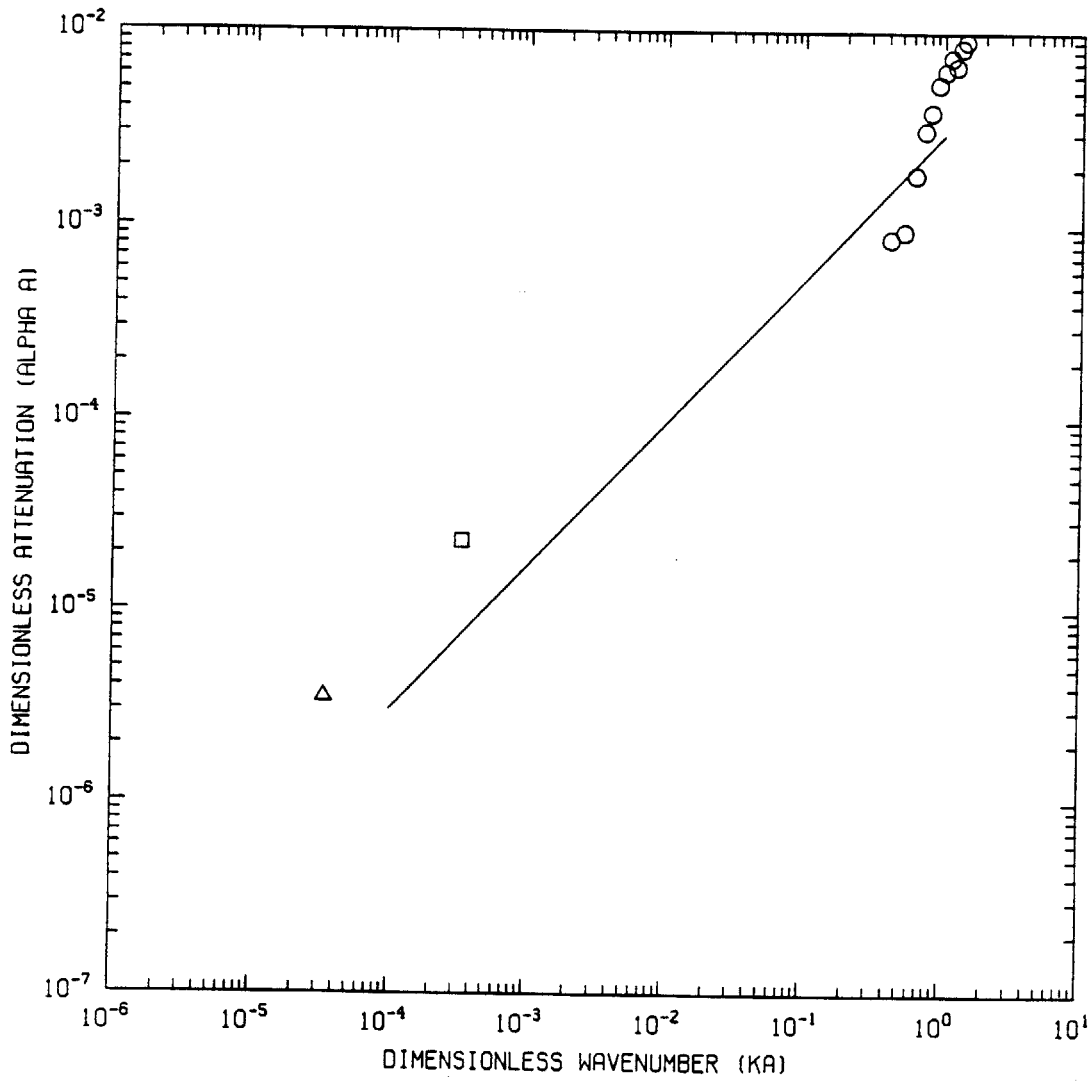


**Figure 3.9:** The data of Urick (1947, ◻), Hampton (1967, ◻) and this study (◦) at about 62% concentration showing the dependence of the dimensionless attenuation  $\alpha a$  on  $(ka)^{3/4}$ .

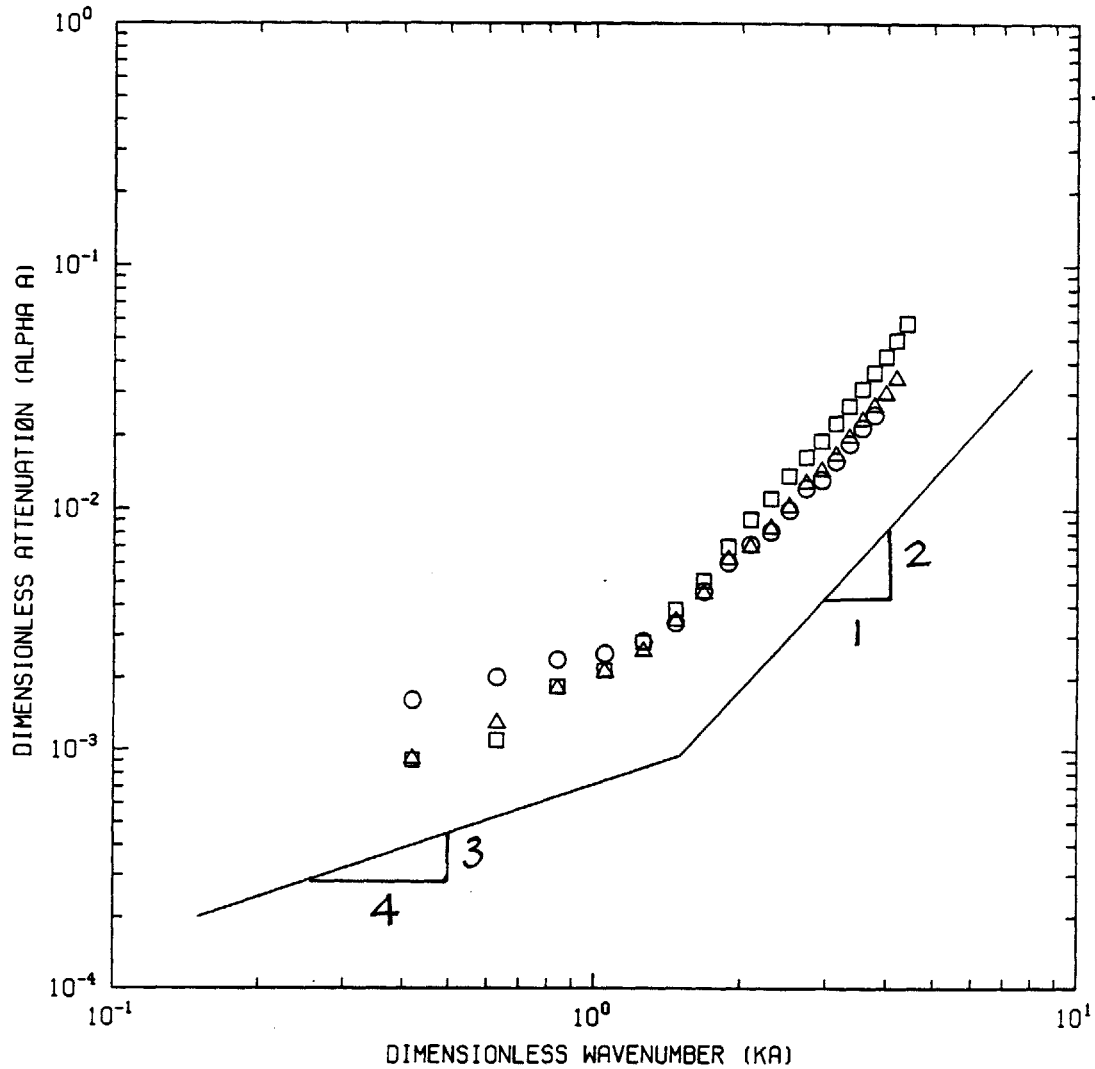


**Figure 3.10:** Attenuation parameter  $\alpha a$  as a function of  $ka$  for 1.0 mm silica beads in water at the maximum packing fraction, showing the  $\frac{3}{4}$  power dependence for  $ka < \sim 1$ , and an apparently quadratic dependence for  $ka > \sim 1$ .

## CHAPTER 4

### DYNAMIC PERMEABILITY IN POROUS MEDIA — A DYNAMIC DRAG APPROACH

#### 4.1 Introduction

The measurement of the dynamic response of fluid saturating a porous medium to an infinitesimal oscillatory pressure gradient has been postulated as an effective non-intrusive method for the determination of the geometry of the interstitial pores that constitute the flow path through the medium. Various models of the predicted response have been presented, based mostly on a combination of phenomenological results for internal flows in passages of various geometries, numerical predictions in simulated capillary and pore geometries as well as experimental data. Johnson, Koplik and Dashen (1987) have presented a model combining phenomenological and analytical arguments to describe the response of a Newtonian fluid saturating the pore space of a rigid, isotropic porous medium under the influence of an infinitesimal oscillatory pressure gradient. Sheng and Zhou (1988), using the approach of Burridge and Keller (1981), have derived a first principles model for the dynamic permeability of a periodic medium of various simulated microstructures. They have shown that there exists an universal behavior for the dynamic permeability, when it is scaled by its static value  $k_0$  and the frequency by a characteristic  $\omega_c$ , that is largely independent of the microstructure of the porous medium.

In an approach parallel to the method of simulating a porous medium as a packed bed of spheres for the determination of steady drag and permeability (Happel, 1958), an analytical model for the dynamic permeability of a packed bed of spheres based on a dynamic drag model is presented. The result of Landau

and Lifshitz (1959) for the drag on a sphere in an oscillating fluid is extended to higher particle concentrations and it is shown that the results for the dynamic permeability and tortuosity agree well at intermediate and high frequencies, with the available experimental results in porous media made up of spheres.

## 4.2 Background

This work was been motivated by the fundamental study of acoustic wave propagation through a suspension of spheres in a Newtonian fluid detailed in Chapter 3. There is a large body of literature on the propagation of acoustic waves in porous media, which has been motivated by seismological, oil exploration and oceanographical interests. However, acoustic wave propagation in porous media and suspensions, while similar, have important differences. For example porous media exhibit elastic resistance to shear stresses while a suspension typically does not. Both however can sustain isotropic stresses. One of the difficulties is in the representation of the relative motion between fluid and solids. This, in porous media is described in terms of a frequency dependent permeability, which has recently received attention (Attenborough, 1983; Johnson *et al.*, 1987): with a pore size,  $d$ , as a characteristic geometric length scale, if the viscous boundary layer thickness,  $\delta = \sqrt{2\mu/\rho_1\omega}$ , is significantly greater than  $d$ , the permeability scales with viscosity and equals its steady flow value. On the other hand if  $d \gg \sqrt{2\mu/\rho_1\omega}$ , the flow is essentially inviscid, is dominated by inertia and can be computed using potential theory in conjunction with boundary layer analysis. Under these conditions, the dissipation is restricted to the thin boundary layer surrounding each particle.

While similar scaling arguments can be made with suspensions, the analog of permeability is inherently coupled with the motion of the particles that cannot be

described with linear elasticity. However, by assuming that a porous medium may be modelled as a suspension of spheres at high solids' fraction, with the added restriction that the particles are restrained and may not move relative to one another, it is of interest to see how the suspension theory predicts the dynamic permeability and tortuosity of the simulated porous medium, and in addition if it can shed some light on the somewhat intractable geometric parameters inherent in the models available. In general this analysis is restricted to those frequencies and porosities such that the boundary layers on adjacent particles do not overlap or interact with each other.

Probstein (1989) discusses capillary and drag models for the determination of the pressure drop due to steady flow through porous media. Recent work (Johnson *et al.*, 1987) has extended the capillary or Darcy type models for the pressure drop-velocity relationship to the case of oscillatory pressure gradients. Instead the approach that Happel (1958) and others have used for the steady flow case is adopted, and it is chosen to model the porous medium as a random assemblage of monodisperse spheres. By determining the drag on a single sphere for the case of oscillatory fluid flow, and scaling up the results to the whole medium, the pressure drop across the porous medium can be determined. To this end we present a model for the flow in a porous medium made up of monodisperse spheres.

Specifically, the small amplitude solution of the Navier-Stokes equations to the problem of oscillatory fluid flow around a sphere in a viscous fluid is generalized to the case of a high concentration of spheres. The dynamic permeability and tortuosity are then calculated as a function of frequency, and these predictions are compared to the available models and experimental results.

### 4.3 Governing equations

#### 4.3.1 Momentum equation

A general model for a *suspension* of monodisperse spheres in a Newtonian liquid is adopted here, and it is assumed that in the limit that the particle concentration or solids' fraction tends to the maximum packing limit,  $\nu \rightarrow \nu_{max}$ , that the suspension approaches the behavior of a porous medium made up of packed spheres. Then, by relating the instantaneous pressure gradient to the instantaneous fluid velocity in the packed bed (by casting the momentum equation for the fluid into a form analogous to that of the Darcy model), the expected response to a infinitesimal oscillatory pressure gradient in the composite medium, and hence the dynamic permeability, may be derived.

The procedure for the formulation of the model is as follows: a volume averaged momentum balance for the liquid phase is written. Thereafter by invoking the theoretical result of Landau and Lifshitz (1959) for the drag between the phases and scaling this result to higher concentrations, the response of the interstitial fluid velocity to a fluctuating pressure gradient may be calculated.

In developing the momentum conservation equation for high frequency oscillatory fluid velocities in a concentrated mixture, it is helpful to evaluate the relative importance of viscous and inertial effects. It is shown below that inertial effects dominate the particle drag for high frequencies. For these the Reynolds number for oscillatory motion of a particle of radius  $a$  in a fluid of kinematic viscosity  $\frac{\mu}{\rho_l}$ ,

$$R = \sqrt{\frac{\rho_l \omega a^2}{2\mu}} = \frac{a}{\delta}, \quad (4.1)$$

is very high and it is evident therefore that the flow around the particles is essentially inviscid, with the exception of thin viscous boundary layers surrounding

the particles. It is to these thin boundary layers that the viscous dissipation in the system is restricted. While it is specifically discussed below, the appropriate form of the one-dimensional momentum equation for the fluid, neglecting gravitational and fluid compressibility effects, is:

$$\rho_l(1 - \nu) \left[ \frac{\partial v_l}{\partial t} + v_l \frac{\partial v_l}{\partial x} \right] = -\frac{\partial P}{\partial x} + F_{ls} \quad \text{liquid momentum} \quad (4.2)$$

Viscous dissipation within the bulk of the fluid (beyond the particle boundary layers) is neglected, hence the absence of a  $\mu \nabla^2 v_l$  term. Only dissipation due to phase interactions is considered, the origin of which is considered next.

#### 4.3.2 The solid-liquid interaction force

The momentum interaction force between the solid and the liquid,  $F_{sl} = -F_{ls}$ , consists in general of dynamic drag (containing viscous and inertial effects) and buoyancy forces. In order to ascertain the momentum interaction force due to drag alone for a flow through a packed bed of spheres, the result for the drag on a single particle in an assembly of like particles must be extended to arbitrary concentrations. The analysis proceeds as follows: the drag on a single isolated particle (Section 4.3.3) is modified to give the drag on a single particle in an assembly of like particles (Section 4.3.4). This result is then scaled up to arbitrary concentrations to give the dynamic drag component of the momentum interaction force between the phases (Section 4.3.5).

#### 4.3.3 Drag on an isolated sphere

The unsteady drag force on a single isolated sphere (i.e. at infinite dilution) was derived by Landau and Lifshitz (1959) for the case of oscillatory fluid motion:

$$F_D^{\nu \rightarrow 0} = - \left[ 6\pi\mu a \left( 1 + \frac{a}{\delta} \right) v_l + 3\pi a^2 \rho_l \left( \frac{2}{9} a + \delta \right) \frac{Dv_l}{Dt} \right] \quad (4.3)$$

where

$$\frac{Dv_l}{Dt} = \left[ \frac{\partial v_l}{\partial t} + v_l \frac{\partial v_l}{\partial x} \right]. \quad (4.4)$$

The specific form of this time derivative satisfies the condition of objectivity (Drew, 1983). The quantity  $\delta$  ( $= \sqrt{2\mu/\rho_l\omega}$ ) is the unsteady viscous boundary layer thickness surrounding the particle. Its dimension relative to the separation between nearest neighbors provides a measure of the importance of viscous effects. At low frequencies,  $\delta$  is large, while the converse is true at high frequencies. For oscillatory, or harmonic, motion of the fluid  $v_l = v_l^0 e^{-i\omega t}$ , it is found that

$$F_D^{\nu \rightarrow 0} = -6\pi\mu a v_l \left[ 1 + a \sqrt{\frac{\rho_l}{2\mu}} \sqrt{\omega} - i \frac{a^2 \rho_l}{9\mu} \omega - i \frac{a \rho_l}{2\mu} \sqrt{\frac{2\mu}{\rho_l}} \sqrt{\omega} \right] \quad (4.5)$$

$$= -6\pi\mu a v_l \left[ 1 + a \sqrt{\frac{\rho_l}{2\mu}} \sqrt{\omega} - i a \sqrt{\frac{\rho_l}{2\mu}} \sqrt{\omega} - i \frac{a^2 \rho_l}{9\mu} \omega \right] \quad (4.6)$$

$$= -6\pi\mu a v_l \left[ 1 + \frac{a}{\delta} - i \frac{a}{\delta} - i \frac{2a^2}{9\delta^2} \right]$$

This implies that for  $\delta \gg a$ , or alternatively (noting that  $R = \frac{a}{\delta}$ )  $R \ll 1$ , the drag force reduces to the steady Stokesian drag, *i.e.* viscous forces dominate. On the other hand for large  $\omega$ , or  $\delta \ll a$ , the steady drag term becomes negligible compared to the dissipative terms that arise from the Basset or history terms ( $\frac{a}{\delta}$  and  $i\frac{a}{\delta}$ ) and the inertial term ( $i\frac{2}{9}\frac{a^2}{\delta^2}$ ).

To give an indication of the regime of validity of each of the terms in Equation (4.7) above, for a 1 mm diameter particle in water the crossover frequency at which the steady viscous drag term (*i.e.* the  $\omega^0$  term) equals the transition terms (these contain  $\delta^{-1}$ ) is 0.25 Hz. Correspondingly the second crossover frequency at which the  $\omega^1$  term (the inertial term) starts to dominate the drag is at about 18 Hz. From this the following asymptotic behavior can be recognized. At very low  $\omega$ , the expression reduces to the well known steady Stokes drag result,

$$F_D^{\nu \rightarrow 0} \stackrel{\text{lim}}{\omega \rightarrow 0} -6\pi\mu a v_l \quad (4.8)$$

and at high  $\omega$ , the dominant term is

$$F_D^{\nu \rightarrow 0} \underset{\omega \rightarrow \infty}{\equiv} \lim -\frac{1}{2} \rho_l \frac{4\pi a^3}{3} \frac{Dv_l}{Dt}. \quad (4.9)$$

This latter equation be recognized as the added mass term for the drag on an isolated sphere where the added mass coefficient,  $C$  is  $\frac{1}{2}$ . So clearly for frequencies very much greater than the second cross-over frequency (say, for example  $>1$  kHz) it is appropriate to use the inertial asymptotic behavior of the drag law. However, while the drag becomes inertially dominated for high  $\omega$ , the dissipation associated with the particle and fluid oscillation remains viscous in origin but is restricted to a boundary layer surrounding each particle that becomes thinner with increasing frequency of oscillation.

#### 4.3.4 The added mass term and its dependence on concentration

It has long been recognized that the added mass coefficient associated with each sphere in a suspension is not a constant but is a function of concentration as well as the geometrical configuration of the suspension. An expression for the added mass coefficient as a function of particle concentration is developed. By analogy, the dependence of added mass on solids' fraction is directly related to Maxwell's relation for the effective conductivity of such an assembly of non-conducting spheres in a conducting fluid. This analogy is appropriate as Laplace's equation describes both the electrical potential equation and the potential flow equation in the two processes. Wallis (1989) showed that the relationship between the added mass coefficient and the normalized mixture conductivity is

$$C = \frac{1}{2\beta}, \quad (4.10)$$

where  $\beta$  is the ratio of the liquid conductivity to that of the mixture. Maxwell (1881) obtained for a random assembly of spheres

$$\beta = \frac{1 + \nu/2}{1 - \nu}, \quad (4.11)$$

which has been shown to be a good approximation up to maximum packing concentrations of mono-dispersed spheres (Turner, 1976). The added mass coefficient then is

$$C(\nu) = \frac{1 - \nu}{2 + \nu}, \quad (4.12)$$

which will be used in the momentum equation. It must be remembered here that this coefficient is very sensitive to the geometrical configuration of the particles in the mixture, which explains the differences between existing predictions of the added mass coefficient for a sphere in a highly concentrated suspension. The drag on a single particle in an assembly of like particles at a solids' fraction of  $\nu$  is thus

$$F_D^\nu = 6\pi\mu a \left(1 + \frac{a}{\delta}\right) (v_s - v_l) + 3\pi a^2 \rho_l \left(\frac{4}{9} C(\nu) a + \delta\right) \frac{D(v_s - v_l)}{Dt}. \quad (4.13)$$

The tortuosity  $\alpha$  is defined for a porous medium by the inertially dominated momentum balance (Johnson *et al.*, 1987)

$$\alpha \rho_l \frac{\partial v_l}{\partial t} = -\nabla P.$$

For an inviscid flow, the tortuosity is thus given by

$$\alpha = 1 + \frac{\nu}{(1 - \nu)} C(\nu) \quad (4.14)$$

For a packed bed of spheres of porosity 0.365 (or a solid fraction of 63.5%) we obtain  $\alpha = 1.24$  which compares well to tortuosities of  $\sim 1.50$  measured

electrically in porous media of sintered glass beads of 30% porosity (Johnson *et al.*, 1982).

#### 4.3.5 The extension of the single particle result to an assembly of particles

The momentum interaction force between the solid and the liquid,  $F_{ls}$ , consists in general of dynamic drag (containing viscous and inertial effects) and buoyancy forces. In order to ascertain the momentum interaction force due to drag alone for a concentrated mixture, the single particle drag result must be extended to arbitrary concentration. It is well known that for very low particle concentrations the drag on an assemblage of particles increases linearly with the solids' fraction; it is assumed here that linear superposition of the viscous interactions is appropriate up to maximum packing, or roughly 62% by volume for monodisperse spheres.

To extend the single particle drag result to higher concentrations, we assume that the equivalent drag per unit volume for the suspension  $F_{eq}$  is equal to the drag per sphere multiplied by the number of spheres per unit volume,  $n$ , or  $F_{eq} = n F_D^v$ . This result is an approximation and is tantamount to neglecting hindered settling effects in particle sedimentation — the non-linear interactions between adjacent particles at high concentrations are neglected. It is known that the solids' fraction, which is the volume of particles per unit total volume, is related to the number of particles per unit volume by

$$\nu = n \left( \frac{4\pi a^3}{3} \right)$$

Thus

$$n = \frac{3\nu}{4\pi a^3}. \quad (4.15)$$

As was mentioned previously, there is also a component of the phase interaction force which is due to the instantaneous pressure gradients. This buoyancy force is added to the equivalent drag force for the suspension to give the momentum interaction force between the phases

$$F_{ls} = \frac{3\nu F_D^\nu}{4\pi a^3} + \nu \frac{\partial P}{\partial x} \quad (4.16)$$

where  $F_D^\nu$  is the unsteady force on a single (stationary) sphere of radius  $a$  in an assembly of like particles subjected to oscillatory fluid motion, given in Equation (4.13).

This theory in effect assumes an assembly of non-interacting particles as it neglects viscous interactions between adjacent particles, which is valid in the limit that  $\delta \ll r_H$ , where  $r_H$  is the hydraulic radius of an average flow channel between the particles. The hydraulic radius is related to the average inter-particle spacing  $h$  and is thus strongly concentration dependent. Now from geometrical arguments  $h$  is given by

$$\frac{h}{a} = \frac{1 - \eta^{\frac{1}{3}}}{\eta^{\frac{1}{3}}}, \quad (4.17)$$

where

$$\eta = \frac{\nu}{\nu_{max}},$$

and  $\nu_{max} \simeq 0.635 \pm 0.005$  for a random close packed structure of monodisperse spheres and  $\nu_{max} \simeq 0.555$  for random loose packing (Onoda and Liniger, 1990). Now the mean hydraulic radius for the passages formed in a packed bed of spheres is given by

$$r_H = 2 \frac{\text{pore volume}}{\text{interfacial area}} = 2 \frac{(1 - \nu)}{3\nu} a \quad (4.18)$$

which equals  $0.383a$  for  $\nu_{max} = 0.635$  and  $0.535a$  for  $\nu_{max} = 0.555$ . A more restrictive pore dimension is the minimum hydraulic radius, which for a suspension

of spheres at a given concentration arises at the throat formed by three particles lying in the same plane in a triangular formation. For this configuration, the minimum hydraulic radius is given by

$$(r_H)_{min} = a \left[ \frac{2\sqrt{3}}{\pi} \frac{1}{\eta^{2/3}} - 1 \right] \quad (4.19)$$

which equals  $0.103a$  at the maximum close packing limit.

Now the requirement for the particles that make up the porous medium to be non-interacting is

$$\delta \ll (r_H)_{min}.$$

(The frequency at which  $\delta = (r_H)_{min}$  is denoted as  $\omega_{min}$ ). The above requirement implies that the frequencies for which the present theory is valid are such that

$$\omega \gg \omega_{min} = \frac{2\mu}{a^2 \rho_l \left[ \frac{2\sqrt{3}}{\pi} \frac{1}{\eta^{2/3}} - 1 \right]^2}.$$

The regime of  $\omega$  and  $\nu$  for which this restriction holds is shown for 1.0 mm diameter particles in water in Figure 4.1.

## 4.4 Dynamic Permeability

### 4.4.1 General solution

The dynamic pressure drop-velocity relationship for the case of the porous medium of packed spheres may now be derived along with the relationship for the frequency dependent permeability. Substituting the expression for the momentum interaction force between the phases into the liquid momentum equation gives

$$\left[ \rho_l + \frac{\nu \rho_l}{(1-\nu)} \left( C(\nu) + \frac{9}{4} \frac{\delta}{a} \right) \right] \left( \frac{\partial v_l}{\partial t} + v_l \frac{\partial v_l}{\partial x} \right) + \left[ \frac{9}{2} \frac{\nu}{(1-\nu)} \frac{\mu}{a^2} \left( 1 + \frac{a}{\delta} \right) \right] v_l + \frac{\partial P}{\partial x} = 0. \quad (4.20)$$

In their analysis of the flow in a porous medium due to an oscillating pressure gradient, Johnson *et al.* (1987), define the dynamic permeability  $k(\omega)$ , such that

$$(1 - \nu)v_l = -\frac{k(\omega)}{\mu}\nabla P.$$

Casting Equation (4.20) into the same form, linearizing and assuming an harmonic liquid velocity

$$v_l = v_l^0 e^{-i\omega t}$$

gives

$$k(\omega) = \left[ \frac{9}{2a^2} \frac{\nu}{(1-\nu)^2} \left(1 + \frac{a}{\delta}\right) - i \frac{\omega \rho_l}{\mu(1-\nu)} \left\{ 1 + \frac{\nu}{(1-\nu)} \left( C(\nu) + \frac{9}{4} \frac{\delta}{a} \right) \right\} \right]^{-1}.$$

Expanding  $k(\omega)$  gives

$$k(\omega) = \frac{\left[ \frac{9}{2a^2} \frac{\nu}{(1-\nu)^2} \left(1 + \frac{a}{\delta}\right) + i \frac{\omega \rho_l}{\mu(1-\nu)} \left\{ 1 + \frac{\nu}{1-\nu} \left( C(\nu) + \frac{9}{4} \frac{\delta}{a} \right) \right\} \right]}{\left[ \frac{9}{2a^2} \frac{\nu}{(1-\nu)^2} \left(1 + \frac{a}{\delta}\right) \right]^2 + \left[ \frac{\omega \rho_l}{\mu(1-\nu)} \left\{ 1 + \frac{\nu}{1-\nu} \left( C(\nu) + \frac{9}{4} \frac{\delta}{a} \right) \right\} \right]^2} \quad (4.21)$$

which is applicable for all  $\omega$  such that  $\delta < (r_H)_{min}$ , *i.e.*  $\omega > \omega_{min}$ .

The low frequency limit for the permeability is

$$k(\omega) \underset{\omega \rightarrow 0}{\lim} \frac{2}{9} a^2 \frac{(1-\nu)^2}{\nu} = k_0 \quad (4.22)$$

which is, strictly speaking, valid only for very low solids' concentrations as it neglects non-linear effects that arise due to viscous interactions at high concentrations. However for a porous medium made up of 0.85 mm radius spheres at the maximum packing fraction, the predicted  $k_0 \simeq 3.2 \times 10^{-2} \text{ mm}^2$ , which is of the same order as experimental results obtained by Charlaix *et al.* (1988) ( $1.2 \times 10^{-2} \text{ mm}^2$  for 0.85 mm radius beads). The discrepancy between the experimental result and that predicted by this analysis is of the same order as the difference

between hindered and unhindered drag laws for particles sedimenting at high concentrations. The dc permeability  $k_0$  is thus related to the mean hydraulic radius of the pore spaces in the porous medium (defined in Equation 4.18) by

$$k_0 = 2 r_H^2 \nu, \quad (4.23)$$

implying that as the hydraulic radius of the pores increases, so the medium permeability increases.

#### 4.4.2 High frequency permeability

Using the fact that for  $\omega \rightarrow \infty$ ,

$$R = \frac{a}{\delta} \gg 1$$

or conversely

$$R^{-1} = \frac{\delta}{a} \ll 1$$

the high frequency asymptote for the permeability is obtained as

$$k(\omega) \stackrel{\text{lim}}{\omega \rightarrow \infty} \frac{9\nu}{2\sqrt{2}a} \left(\frac{\mu}{\rho_l}\right)^{\frac{3}{2}} \frac{1}{\alpha^2} \omega^{-\frac{3}{2}} + i \frac{(1-\nu)}{\alpha} \left(\frac{\mu}{\rho_l}\right) \omega^{-1} \quad (4.24)$$

where  $\alpha$  is the tortuosity of the medium. This result has no restrictions on  $\nu$  for all  $\omega > \omega_{min}$ . The cross-over frequency at which this theory predicts that the contribution to the permeability of the  $\omega^{-\frac{3}{2}}$  term equals that of the  $\omega^{-1}$  term for the case of 0.85 mm spheres (0.475 mm) is approximately 9.3 Hz (29.8 Hz), which compares very well to experimental results of 6.2 Hz for the case of 0.85 mm spheres and 25 Hz for 0.475 mm spheres established by Charlaix *et al.* (1988).

Sheng and Zhou (1988) have proposed the following non-dimensional scaling for the frequency

$$\tilde{\omega} = \frac{\omega}{\omega_c}$$

where

$$\omega_c = \frac{\mu(1-\nu)}{\rho l k_0 \alpha},$$

and for the dynamic permeability

$$\tilde{k}(\tilde{\omega}) = \frac{k}{k_0}. \quad (4.25)$$

The dynamic permeability (Equation 4.24) may thus be represented in the non-dimensional form

$$\begin{aligned} \tilde{k}(\tilde{\omega}) &= \left[ 1 + \frac{a}{\delta} - i \frac{\tilde{\omega}}{\alpha} \left\{ 1 + \frac{\nu}{1-\nu} \left( C(\nu) + \frac{9}{4} \frac{\delta}{a} \right) \right\} \right]^{-1} \\ &= \left[ 1 + R - i \frac{\tilde{\omega}}{\alpha} \left\{ \alpha + \frac{9}{4} \frac{\nu}{1-\nu} \frac{1}{R} \right\} \right]^{-1} \end{aligned} \quad (4.26)$$

where  $\alpha$  is the (inertial) tortuosity of the medium. The non-dimensional dynamic permeability thus depends on the Reynolds number,  $R$ , the suspension porosity  $(1-\nu)$  and the tortuosity  $\alpha$  alone.

#### 4.5 Discussion: Comparison to Existing Models

Using an approach analogous to Darcy's law, Sheng and Zhou (1988) obtain from a first principles analysis of oscillatory flow in capillaries (in dimensionless variables)

$$\tilde{k}(\tilde{\omega}) = \begin{cases} 1 + iF_1^{-1}\tilde{\omega}, & \tilde{\omega} \rightarrow 0, \\ \sqrt{2}F_2^{-1}\tilde{\omega}^{-\frac{3}{2}} + i\tilde{\omega}^{-1}, & \tilde{\omega} \rightarrow \infty. \end{cases}$$

where

$$F_1 = \left( \frac{\alpha k_0^2}{C_1(1-\nu)} \right)$$

$$F_2 = \left( \frac{\Lambda^2(1-\nu)}{\alpha k_0} \right)^{\frac{1}{2}}. \quad (4.27)$$

The parameter  $C_1$  is a geometric shape coefficient and  $\frac{2}{\Lambda}$  is a flow velocity-weighted surface area to pore volume ratio, and is thus directly analogous to the hydraulic radius  $r_H$  of the present treatment. Charlaix *et al.* (1988) have found experimentally that for packed beds of spheres of radii in the range 0.25 to 0.85 mm,  $F_1 \simeq 0.71 - 0.75$  and  $F_2 \simeq 2.8 - 3.0$ .

From the present derivation by comparison, (in primitive variables)

$$k(\omega) = \frac{9}{2} \left( \frac{\nu}{\sqrt{2}a} \right) \left( \frac{1}{\alpha^2} \right) \left( \frac{\mu}{\rho_f} \right)^{\frac{3}{2}} \omega^{-\frac{3}{2}} + i(1-\nu)\alpha^{-1} \left( \frac{\mu}{\rho_f} \right) \omega^{-1}. \quad (4.28)$$

In non-dimensional terms this reduces to

$$\tilde{k}(\tilde{\omega}) = \begin{cases} 1 + i\tilde{\omega}, & \tilde{\omega} \rightarrow 0, \\ \frac{a}{\delta} \tilde{\omega}^{-2} + i\tilde{\omega}^{-1}, & \tilde{\omega} \rightarrow \infty. \\ \text{or, } R \tilde{\omega}^{-2} + i\tilde{\omega}^{-1}, & \tilde{\omega} \rightarrow \infty. \end{cases} \quad (4.29)$$

Equations (4.27) and (4.29) give expressions for the dynamic permeability resulting from two quite different approaches. However, these two independent approaches give the same frequency dependence for both the high and low frequency asymptotes, and in fact Figures 4.2 and 4.3 show that the dynamic permeability predicted by this theory and that calculated from Equation (4.27) using the experimental values reported by Charlaix *et al.*, (1988), are quite close in value. Figure 4.2 shows the magnitude of the real part of the permeability, while Figure 4.3 shows the imaginary component. Figure 4.4 shows the phase associated with the permeability, which translates into the phase lag that the velocity experiences with respect to the pressure perturbation at increasing frequencies. It should be noted that the present treatment gives a result that is independent of any scaling factors other than those inherent in the tortuosity and concentration. For the

purposes of predicting the permeability of porous media, the models of Sheng and Zhou (1988), Zhou and Sheng (1989) and Johnson *et al.* (1987) require values of the parameter  $\Lambda$  which do not appear to be analytically predictable. On the other hand, this model which is admittedly limited to high frequencies at low medium porosities, requires knowledge of the porosity  $(1 - \nu)$ , the particle Reynolds number and the tortuosity alone.

It has been found that the dynamic permeability of a porous medium made up of monodisperse spheres is governed by the unsteady Reynolds number of the oscillatory flow around the particles, the particle added mass, the porosity of the medium, and most importantly the mean hydraulic radius of the interstitial pores. This theory provides a mechanism whereby the pore size and geometry in a packed bed of spheres may be ascertained in a non-intrusive fashion. In the case of a polydisperse system with a wide range of pore sizes and geometries, it is anticipated that the experimental results might deviate significantly from the present theory, due to the fact that the dominant viscous attenuation mechanism in such a system would be due to the oscillatory flow through the smallest pore spaces, these being quite significantly smaller than the average in the polydisperse case.

A derivation for the frequency dependent dynamic permeability of a porous medium of spheres has been presented by considering the external flow around particles in a suspension and extending these results to high solids' fractions. This approach has been shown to give results that are consistent with those obtained by considering internal flow in cylindrical and sinuous pores.

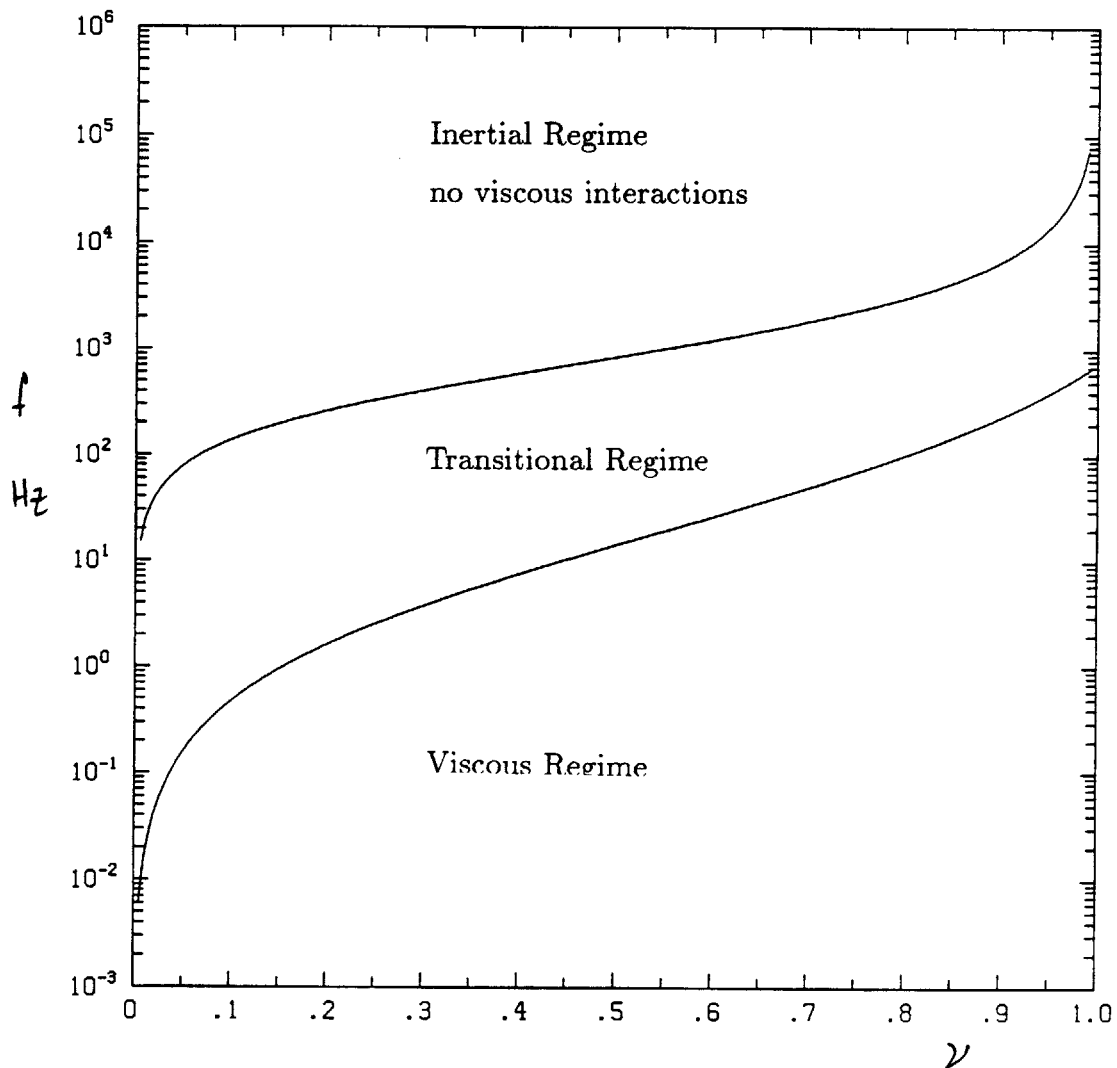


**Figure 4.1:** Regime map of the range of frequencies for which the assumption of non-interacting particles is valid in the dynamic permeability model. The lower curve is the frequency constraint calculated according to Equation 4.18, while the upper curve is calculated from the more restrictive Equation 4.19. For frequencies above the theoretical curve, the 0.5 mm radius pores may be considered to have non-overlapping viscous boundary layers.

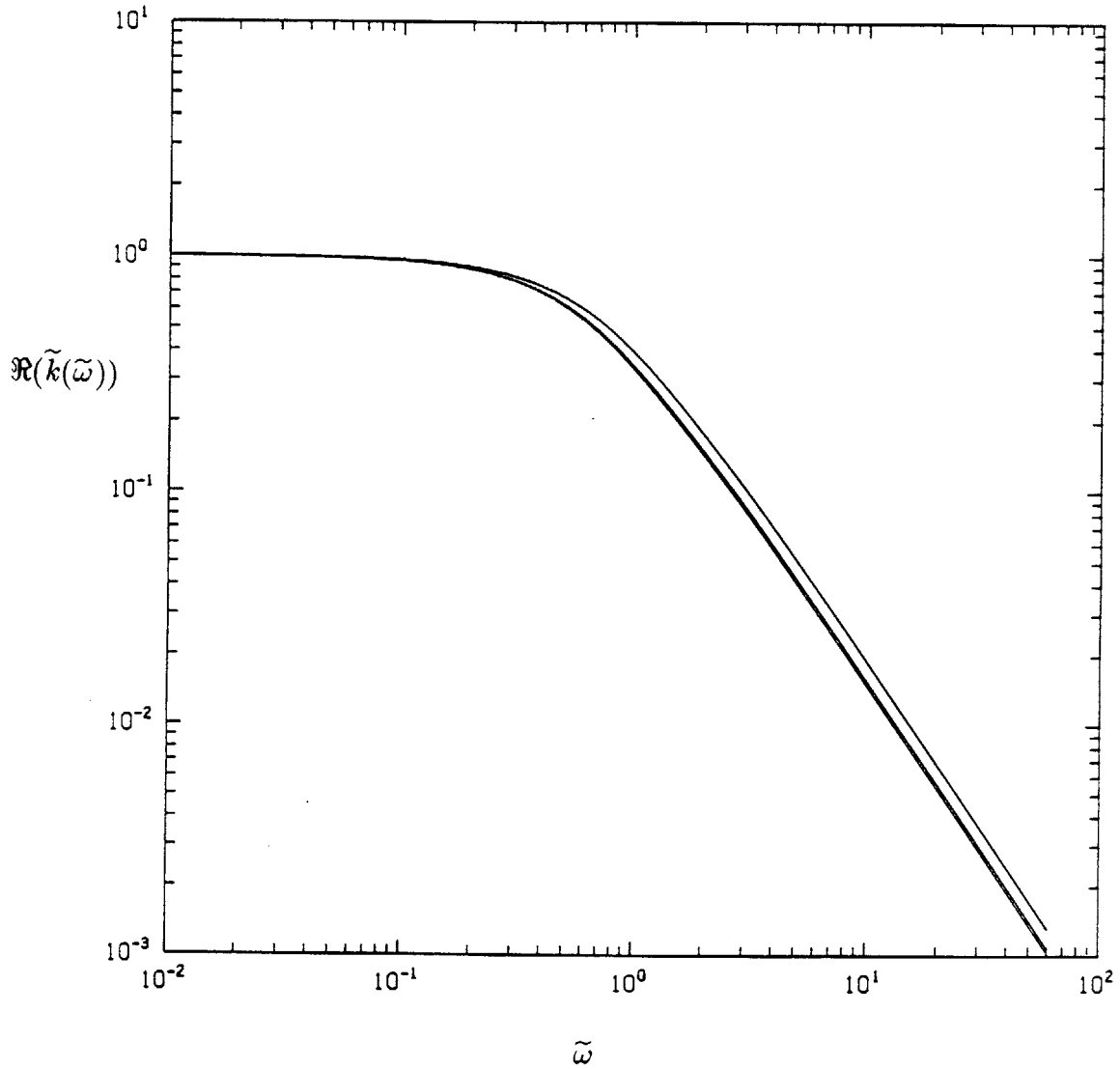


**Figure 4.2:** Real part of the dynamic permeability  $\Re(\tilde{k}(\tilde{\omega}))$ , as a function of the dimensionless frequency  $\tilde{\omega}$  showing the crossover frequency  $\tilde{\omega} \simeq 1$ . The upper curve is the prediction of the present theory (Equation 4.29) while the lower curves are for the theory of Sheng and Zhou (1988) (Equation 4.27) with  $F_1 = 0.71$ ,  $F_2 = 2.8$  and  $F_1 = 0.75$ ,  $F_2 = 3.0$ .

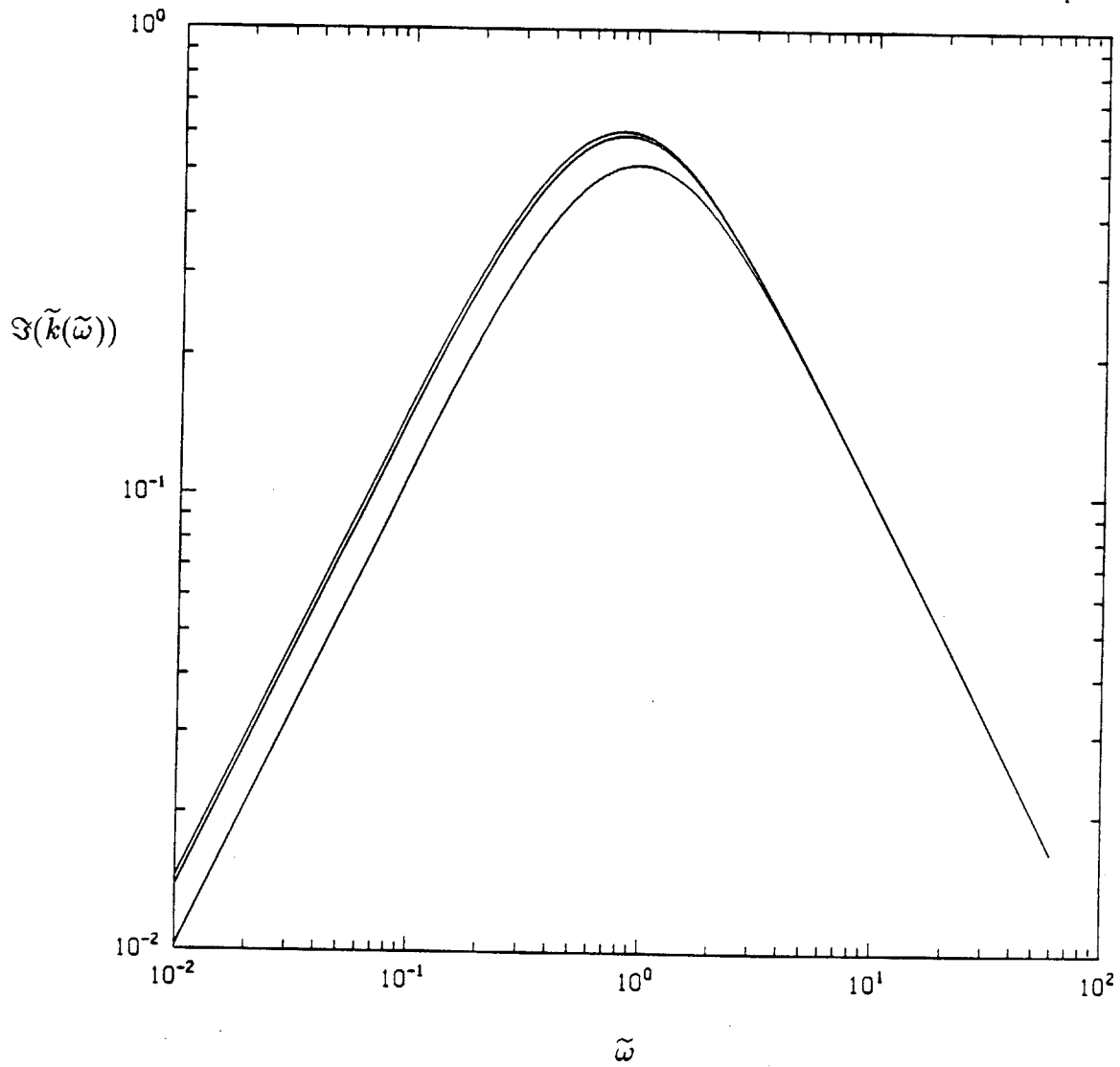


**Figure 4.3:** Frequency dependence of the Imaginary part of the dynamic permeability  $\Im(\tilde{k}(\tilde{\omega}))$ . Refer to Figure 4.2.

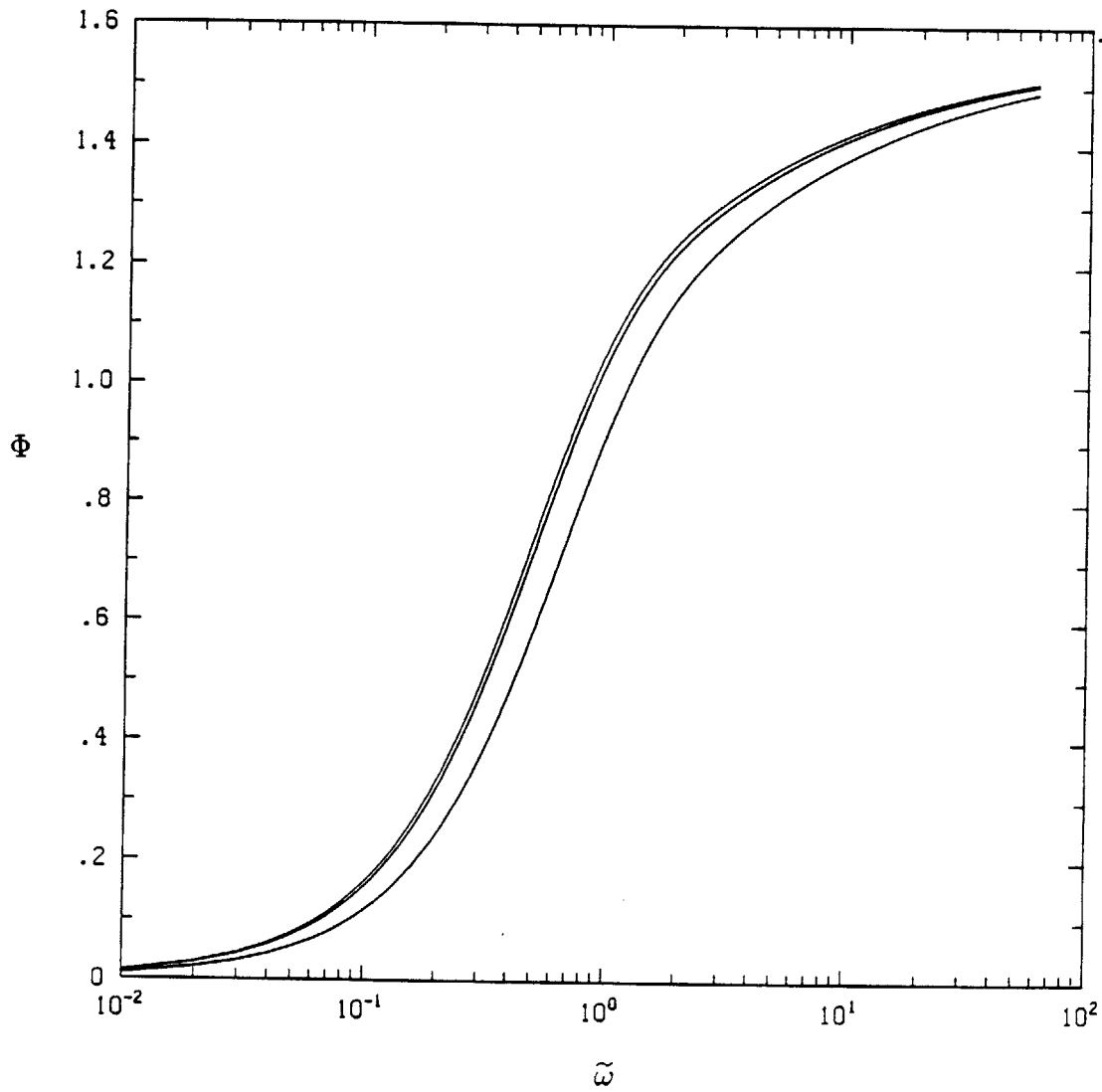


**Figure 4.4:** Frequency dependence of the phase of the dynamic permeability defined as

$$\Phi = \arctan \frac{\Im(\tilde{k})}{\Re(\tilde{k})}.$$

Refer to Figure 4.2.

## CHAPTER 5

### ULTRASONIC DOPPLER VELOCIMETRY

#### 5.1 Introduction

Ultrasound as a technique for interrogating two-phase mixtures has the advantages of being non-intrusive, it has a very high frequency response and is able to penetrate typically opaque highly concentrated mixtures. It has been shown in this thesis that there exists an inherent compromise in the choice of the frequency of the ultrasound between maximizing spatial resolution (high  $ka$ ) and ensuring adequate beam penetration (low  $ka$ ). To this end, the propagation of ultrasound in solid-liquid mixtures has been investigated experimentally for a range of frequencies and concentrations of the dispersed phase. The limitations of ultrasonic wave propagation as a non-intrusive diagnostic technique, in terms of spatial resolution, are clear: to maximize resolution while maintaining adequate beam penetration into a highly concentrated mixture requires  $ka \sim O(1)$ . Acknowledging these limitations, ultrasonic instrumentation for determining the velocity of moving particles at or near maximum packing was developed. Preliminary results from a prototypical ultrasonic Doppler velocimeter show good agreement with observations of the settling velocity of silica beads at high concentrations. A new version of this velocimeter was used to measure particle velocities in a Dynamic Shear Cell (Figure 5.1) (Poutiatine, 1990), and to quantify the scattering characteristics of particulate mixtures for further acoustic instrumentation development.

Ultrasound (typically in the range of tens of kilohertz to several megahertz) has several distinct advantages over other methods of measurement in the investigation of highly concentrated mixtures. It is truly non-intrusive (unlike

resistive or capacitive point probes such as those described by Shook *et al.*, 1982, or Hsu *et al.*, 1989), it has an inherently high frequency response, and can thus be used for the measurement of dynamic or transient phenomena; it can penetrate highly concentrated and optically opaque mixtures (unlike laser Doppler anemometry or other optical techniques which require index of refraction matching, as described by Kadambi, Bhunia and Dybbs, 1988, for example) and it has the capability of providing good spatial resolution. Ultrasonic wave propagation has been used extensively in the measurement of single phase flowrates (for *in vivo* blood flow measurements (McLeod, 1967)). A wide variety of acoustic and ultrasonic instruments for the measurement of single phase fluid velocities in industrial applications have been developed. The earliest acoustic flow measurements made were based on the contrapropagating transmission technique (see, for example the comprehensive review by Lynnworth, 1990). These flowmeters, developed for use in predominantly single phase systems such as gas and water pipelines, rely on the mechanism that the time of flight of sound between two points in a flowing fluid will change with the fluid velocity. Other more sophisticated devices such as ultrasonic cross-correlation flowmeters (Ong and Beck, 1975), and ultrasonic vortex flowmeters (Joy, 1984) have also found widespread use in single phase flows. Several proprietary devices are available that infer fluid velocities from the Doppler shift due to particles moving along with the fluid (*cf.* Controlotron Corporation, Nusonics, Polysonics, Leeds and Northrup and Texas Nuclear); these devices are also considered suitable for measurements in suspensions with low solids' loading, such as those found in sewage and waste treatment.

The search for new non-intrusive diagnostic instrumentation for use in advanced coal combustion technology has driven research into acoustic measure-

ment techniques in multiphase systems (Penner *et al.*, 1984). Passive techniques, such as the measurement of flow noise and its correlation with flow velocity (Raptis, 1984) as well as active techniques, such as those employing the Doppler effect have been developed (Karplus and Raptis, 1979; Beltran *et al.*, 1989). Colwell *et al.* (1988) found that for Doppler measurements at  $ka = 0.56$  the velocity of a flowing sand-water slurry could be determined quite accurately at up to 35% particles by volume. In addition, they found that at  $ka = 1.12$  the signal attenuation was too high to allow for Doppler measurements. Hilgert and Hoffmann (1986) used an ultrasonic Doppler flowmeter to measure the rise velocity of bubbles in a bubble column at gas hold-ups of up to 10% and velocities of up to  $0.25 \text{ ms}^{-1}$ . Ricker and Forster (1985) have measured velocities in 3% aqueous pulp fiber suspensions at velocities of up to  $0.1 \text{ ms}^{-1}$  using a pulsed, focussed Doppler system at 4.7 MHz, giving a claimed spatial resolution of 2 mm. Little work has been performed on measuring slurry velocities at up to maximum packing concentrations, and it is this omission that this work seeks to address.

Acoustic wave propagation as a non-intrusive technique has certainly not been used to its full potential in highly concentrated mixtures, due mainly to the difficulties posed by signal attenuation. There exists an inherent compromise in the selection of operating frequency for an acoustic device between the need to minimize the wavelength (with respect to the physical dimensions of the system under investigation) for better spatial resolution, while maximizing the wavelength (with respect to the particle size) for better penetration of such mixtures.

Described here is the use of an ultrasonic Doppler velocimeter for the measurement of particle velocities in mixtures at up to the maximum packing concentration.

## 5.2 Theory

The Dynamic Shear Cell (Figure 5.1) is a large (400 mm diameter) annular rotating device designed to study the dynamic behavior of saturated beds of particles in response to steady and oscillatory imposed motion. A packed or sedimented bed of particles in water (typically glass beads), of several centimeters in depth, is sheared from below by a rotating roughened plate, and the pore pressure, bed surface height and other features of the mixture are monitored. It was anticipated that the velocity of the particles in the bed could be measured using ultrasonic Doppler velocimetry. Initially, the velocity of the particles at the bed surface below several centimeters of water were measured (Figure 5.2). Thereafter internal velocities of the rotating mixture were measured by repositioning the transmitter and receiver such that their foci coincided below the bed surface. It is thus appropriate to review the physics of the interaction of a sound wave with an interface between a single phase liquid and a two phase mixture as well as the interaction of sound with a packed bed of scatterers.

### 5.2.1 Acoustic reflection, refraction and scattering at a water/sediment interface

In direct analogy to the theory of geometrical optics, when sound passes from a medium of some sonic velocity  $c_s^1$  to a second medium of sonic velocity  $c_s^2$ , some component of the energy of the incident wave will be reflected while the remaining energy will be transmitted into the second medium and refracted. The relative proportions of energy in the reflected and transmitted waves are given by the acoustic impedances of the two media. In terms of the acoustic impedance

$Z = \rho c_s$ , the reflection coefficient  $R_{int}$  is given by

$$R_{int} = \frac{Z_2 - Z_1}{Z_2 + Z_1}. \quad (5.1)$$

This implies that the greater the mismatch in acoustic impedances between the two media, the greater will be the proportion of the incident energy that is reflected back into the first medium. As for the transmitted wave that is refracted at the surface, the angle of refraction measured from the normal  $\theta_r$  is related to the angle of incidence  $\theta_i$  by Snell's Law (Figure 5.2), namely

$$\frac{\sin \theta_i}{c_s^1} = \frac{\sin \theta_r}{c_s^2}. \quad (5.2)$$

In general, for the case of an absorbing (or attenuating) medium, the index of refraction is a complex quantity, and is given by (Jenkins and White, 1957)

$$\underline{n} = n (1 - i \kappa) \quad (5.3)$$

where  $\kappa$  is an extinction coefficient and is related to the attenuation coefficient  $\alpha$  by

$$\kappa = \frac{\alpha \lambda}{4\pi} \quad (5.4)$$

and

$$n = \frac{c_s^1}{c_s^2}. \quad (5.5)$$

Now

$$\alpha \lambda = \frac{\alpha a}{ka} 2\pi. \quad (5.6)$$

In this study  $ka \sim O(1)$  while  $\alpha a \sim O(10^{-3})$ , and this implies that  $\kappa \sim O(10^{-4})$ , or that the medium is weakly absorbing and hence that the index of refraction may be approximated by its real component alone with little loss of accuracy. Assuming that a plane acoustical wave encounters a smooth interface between water ( $Z_1 \simeq 1.5 \times 10^6 \text{ kgm}^{-2}\text{s}^{-1}$  and  $c_s^1 \simeq 1500 \text{ ms}^{-1}$ ) and a settled bed of silica particles ( $Z_2 \simeq 3.3 \times 10^6 \text{ kgm}^{-2}\text{s}^{-1}$  and  $c_s^2 \simeq 1650 \text{ ms}^{-1}$ ) at various angles  $\theta_i$  to the normal, the corresponding angles of refraction are given in Table 3.

**Table 3:** Angles of Refraction

$\theta_i$	0°	10°	20°	30°	40°	50°	60°	65.4°
$\theta_r$	0°	11.0°	22.1°	33.4°	45.0°	57.4°	72.3°	90°

This shows that at angles of 65.4° from the normal and greater, there will be total reflection from the settled bed interface — additionally, at angles of  $\sim 50^\circ$  and more, there will be some uncertainty as to the exact path of the refracted wave. Moreover, as the incident acoustic wave will in general not be planar, and noting that for propagation at  $ka \sim 1$  that the wavelength is of the same order as the size of the surface features at the medium interface, the uncertainty in the actual acoustic path will be even more significant.

The scattering behavior of a single elastic particle in a viscous fluid has been studied by many authors, but the more successful studies have been quite recent, beginning with the work of Waterman (1969). In theory, scattering may be fully described by the solution to the equations of motion in the particle and in the surrounding fluid under the influence of an infinitesimal compressional wave, once the boundary conditions have been taken into account. In reality, however, the problem is quite intractable analytically and complex numerically. Böstrom (1980) has studied the scattering of a single mobile elastic particle in a standing acoustical wave, and has presented polar diagrams of the total intensity of the scattered wave as a function of  $ka$  for an aluminum sphere in water. The scattering behavior as a function of  $ka$  is shown in Figure 5.3. The acoustic impedance of aluminum is roughly  $1.7 \times 10^7 \text{ kgm}^{-2}\text{s}^{-1}$ , while that for silica glass is about  $1.3 \times 10^7 \text{ kgm}^{-2}\text{s}^{-1}$ .

What is less well known and considerably more difficult to predict analytically than the scattering response of a single isolated particle, is the scattering performance of an ensemble of particles (Twersky, 1978). An approach termed

“configurational averaging” is sometimes employed to evaluate the non-linear multiple scattering behavior of an arrangement of particles in space. This is of importance in the development of ultrasonic instrumentation operating in the frequency regime  $ka > O(1)$ , as it will determine the response of an interrogated group of particles to an incident compressional wave, but it is not considered here.

### 5.2.2 The Doppler frequency shift

The theory behind ultrasonic Doppler velocimetry borrows much from that of laser Doppler anemometry (LDA), although the non-dimensional wavenumbers in the latter case are several orders of magnitude greater (the frequency of visible light being of the order of  $10^{15}$  Hz). As in LDA measurements, the Doppler shift of sound that is scattered off a moving particle is calculated thus: a particle moving with a velocity  $v_p$  at an angle  $\theta_T$  relative to a transducer  $T_T$  (Figure 5.2) transmitting at a frequency  $f_0$  ‘observes’ an apparent frequency  $f'$  given by

$$f' = \frac{f_0}{\sqrt{1 - v_p^2/c_s^2}} \left( 1 + \frac{v_p}{c_s} \cos \theta_T \right). \quad (5.7)$$

A receiving transducer  $T_R$  aligned at an angle  $\theta_R$  from the direction of motion of the particle ‘sees’ sound scattered from the moving particle of frequency  $f''$  where

$$\begin{aligned} f'' &= f' \frac{\sqrt{1 - v_p^2/c_s^2}}{\left( 1 - \frac{v_p}{c_s} \cos \theta_R \right)} \\ &= f_0 \frac{\left( 1 + \frac{v_p}{c_s} \cos \theta_T \right)}{\left( 1 - \frac{v_p}{c_s} \cos \theta_R \right)}. \end{aligned} \quad (5.8)$$

The Doppler frequency shift measured  $\Delta f_D$  is thus the difference

$$\Delta f_D = f'' - f_0 = f_0 \frac{\frac{v_p}{c_s} (\cos \theta_T + \cos \theta_R)}{\left(1 - \frac{v_p}{c_s} \cos \theta_R\right)}. \quad (5.9)$$

For most physical processes of interest (solid particles in a continuous liquid)

$$\frac{v_p}{c_s} \ll 1 \quad (5.10)$$

so that

$$\Delta f_D = f_0 \frac{v_p}{c_s} (\cos \theta_T + \cos \theta_R). \quad (5.11)$$

This implies that the Doppler shift measured is maximized by maximizing  $f_0$  (subject to the attenuation limitations), and by aligning the transmitting transducer along the line of flight of the particle (either in the same direction as or opposing the direction of motion), and by having the receiver aligned at the same angle as the transmitter. However, if the transmitter angle and the receiver angle are related by the expression

$$\theta_T + \theta_R = 180^\circ, \quad (5.12)$$

the resultant shift measured is zero: this situation is obviously to be avoided. For the measurement of the velocity of a flowing suspension of particles, the orientation of the transmitter and receiver with respect to the flowing mixture is restricted by the geometry of the system — typically the transmitter and receiver cannot be placed in the plane of the flow, which would result in the maximum detectable frequency shift, but must be offset slightly from that plane in order to prevent disturbing the flow. For particles that scatter predominantly in the forward direction (with respect to the incident compressional wave), the choice of transducer orientation is problematic due to the  $180^\circ$  restriction. For

particles that scatter in the rearward direction ( $ka \sim 1$ ) the selection of geometry is clearer: the transducers should preferably be aligned with as large an angle between them and the direction of the flowing mixture.

In ultrasonic Doppler velocimetry the frequency shift is determined by demodulating the backscattered (received) signal with the original (transmitted) signal and measuring the beat or heterodyne signal that arises. This is normally performed by a multiplier or double balanced mixer. The demodulated signal contains two major components at frequencies that are the sum of and the difference between the two signals, and the lower frequency component (which is the one of interest) is isolated through the application of a low-pass filter (see the circuit diagram in the Appendix). Consider the multiplication of two cosinusoidal signals, the monochromatic incident wave of frequency  $f_0$ ,  $A \cos(2\pi f_0 t)$ , and the backscattered and shifted signal  $B \cos[2\pi(f_0 + \Delta f_D)t + \psi] = B \cos(2\pi F t + \psi)$  where  $\psi$  is the phase difference between the transmitted and received signals and  $F = (f_0 + \Delta f_D)$ , where the sign of  $\Delta f_D$  depends on the direction of motion of the scattering particles. In practice, due to the finite size of the scattering volume, velocity distributions across the measuring volume and the scattering behavior of the moving particles, the backscattered signal will be rich in frequency content and will have some distribution of phase information.

$$\begin{aligned}
& A \cos(2\pi f_0 t) \cdot B \cos(2\pi F t + \psi) \\
&= AB \left\{ \left[ \cos(2\pi f_0 t) \cos(2\pi F t) \right] \cos \psi - \left[ \cos(2\pi f_0 t) \sin(2\pi F t) \right] \sin \psi \right\} \\
&= AB \left\{ \left[ \cos(2\pi F t - 2\pi f_0 t) - \sin(2\pi F t) \sin(2\pi f_0 t) \right] \cos \psi \right. \\
&\quad \left. - \left[ \sin(2\pi F t - 2\pi f_0 t) + \sin(2\pi f_0 t) \cos(2\pi F t) \right] \sin \psi \right\}
\end{aligned} \tag{5.13}$$

After low pass filtering, the deconvoluted signal will be

$$\begin{aligned}
& AB \left\{ \cos(2\pi \Delta f_D t) \cos \psi - \sin(2\pi \Delta f_D t) \sin \psi \right\} \\
&= AB \cos(2\pi \Delta f_D t + \psi)
\end{aligned} \tag{5.14}$$

On the other hand, instead of demodulating the received Doppler shifted signal with a signal at the incident frequency,  $f_0$ , a signal at some small frequency offset from the original may be used, namely  $f_0 - \Delta f_{dec}$ . The result is that the final demodulated signal is measured to be  $\Delta f_{dec} + \Delta f_D$  and not simply  $\Delta f_D$ . The advantage to such a demodulation scheme is that the direction of motion of the moving particles may be determined depending on whether the Doppler shifted frequency is greater than or less than the frequency offset. If  $v_p > 0$ , then the resultant frequency is  $\Delta f_{dec} + |\Delta f_D|$ , whereas if  $v_p < 0$ , it is  $\Delta f_{dec} - |\Delta f_D|$ . This technique, used in LDA, is accomplished with a frequency shifting Bragg cell, whereas here the same effect is accomplished electronically. Experimentally the Doppler shifted frequency can be evaluated using an efficient frequency deconvolution scheme such as the Fast Fourier Transform (FFT) technique. In practice while the transmitted signal will be monochromatic (of a single frequency), the received signal will have some frequency bandwidth related to the manner in which the signal is scattered from the moving particles and the fact that the measurement volume is of finite extent.

## 5.3 Experimental Procedure

### 5.3.1 The prototype ultrasonic Doppler velocimeter

Based on the results obtained in the packed bed and fluidized bed experiments, it was clear that an ultrasonic transducer operating at or near  $ka = 1$  could provide information on a flowing mixture of 1.0 mm particles in a 100 mm tube at concentrations up to the maximum packing fraction, where the attenuation factor,  $e^{-\alpha L} \simeq 0.40$ . To confirm this supposition, the prototypical ultrasonic Doppler velocimeter shown schematically in Figure 5.4 was constructed

and tested. The device was operated in the following manner; an unfocused 100 kHz transducer (Massa Corporation) with a natural focal length of about 100 mm, inclined at an angle of about  $45^\circ$  to the vertically flowing solid-liquid mixture, insonified the mixture in a tone-burst mode with ultrasound of a frequency at  $ka \simeq 0.75$ . Approximately 10 complete waveforms were used in each tone-burst. A receiving transducer, aligned with its region of natural focus coincident with that of the transmitter, detected the signal shifted in frequency due to the velocity of the scattering particles with respect to the incident ultrasound.

The Doppler shifted frequency was obtained by demodulating the received signal with the driving signal in a double balance mixer (see the Appendix). This yielded a signal that had components at the sum and the difference of the frequencies of the two waveforms, and the low frequency content, which was proportional to the velocity of the scatterers, was obtained from a low pass filter stage. The Doppler shifted signal (in these experiments in the range 0 to 1000 Hz) was first digitized by a data acquisition system and its spectrum was analyzed by determining its Fast Fourier Transform. The device was tested by measuring the settling velocity of 1 mm glass beads at a range of concentrations in a 100 mm diameter vertical column; the frequency spectra of the velocity corresponding to settling at two different initial volume fractions, namely  $\nu_o = 0.45$  and  $\nu_o = 0.50$ , are shown in Figure 5.5. The particle settling speed was independently verified by visual measurement of the downward velocity of the mixture-water interface, which for a monodispersion settles (on average) at the same speed as the particles. A comparison between the measured settling velocities and the visually observed values corresponding to a range of initial concentrations is shown in Figure 5.6. This graph shows that the settling velocity, as deduced from the Doppler shifted frequency, is a good measure of the actual velocity.

### 5.3.2 Device Refinements

A second generation velocimeter was constructed for use in measuring particle velocities in a Dynamic Shear Cell (Poutiatine, 1990). Among the more significant modifications to the instrument were the use of a smaller transmitter (Panametrics, V310 500 kHz, 12.7 mm radius) and a focussed receiver (Panametrics, V314 1.0 MHz, 12.7 mm radius, 60 mm focal length), and the introduction of a calibrated frequency shift in the demodulation stage for the measurement of directional changes in velocities. The received Doppler shifted signal is demodulated with a signal at some small frequency offset from the original, namely  $f_0 - \Delta f_{dec}$ . The result is that the final demodulated signal is measured to be  $\Delta f_{dec} + \Delta f_D$ . If  $v_p > 0$ , then the resultant frequency is  $\Delta f_{dec} + |\Delta f_D|$ , and if  $v_p < 0$ , it is  $\Delta f_{dec} - |\Delta f_D|$ . This effect is accomplished experimentally by the use of two function generators (Hewlett-Packard 3314A) with a small frequency offset between them, the first being used as the incident or driving signal and the second as the demodulation signal. In addition, the modified velocimeter allowed the orientation of the transmitter and receiver to be varied independently so that the scattering and reflection characteristics of the two phase mixture could be measured as a function of angle.

### 5.3.3 Frequency Resolution and Signal Processing Considerations

The Doppler shifted frequency  $\Delta f_D$  is known to be proportional to the velocity of the scattering particles that travel through the receiver's focal region and the frequency of the incident acoustic wave. If the particle velocity is time-invariant, it is possible to use continuous wave transmission. In order to measure velocity data in dynamically accelerating or decelerating flows, however, the length of the Doppler bursts is limited to being very much less than the timescale

$T$  over which the velocity varies, or

$$\tau \ll T. \quad (5.15)$$

This imposes certain limitations on the method that are addressed below. To resolve the frequency shift accurately, a sufficiently long burst of information of duration  $\tau$  is required such that the demodulated signal contains at least one complete wavelength at the frequency of interest or

$$\tau > \frac{1}{(\Delta f_{dec} \pm \Delta f_D)}. \quad \text{Constraint 1} \quad (5.16)$$

The data acquisition sampling frequency  $f_{sample}$  must be somewhat greater than twice the frequency of interest (the Nyquist criterion) or

$$f_{sample} > 2 (\Delta f_{dec} \pm \Delta f_D). \quad \text{Constraint 2} \quad (5.17)$$

The frequency resolution of the FFT is given by

$$f_{res} = \frac{f_{sample}}{\#_{FFT}} \quad (5.18)$$

where  $\#_{FFT}$  is the number of points in each FFT deconvolution. To maintain good frequency resolution (low  $f_{res}$ ), requires a low sampling rate  $f_{sample}$  (which translates into fewer data points per burst  $N$  for a fixed length burst  $\tau$ ), and a large number of points in the FFT convolution. Alternatively, it is desirable to minimize  $f_{res}$  with respect to the Doppler shift  $\Delta f_D$ , subject to the constraints 1 and 2. Thus

$$\min \frac{f_{res}}{\Delta f_D} = \min \frac{f_{sample}}{\#_{FFT} \Delta f_D} = \frac{2}{\#_{FFT}} \left( \frac{\Delta f_{dec}}{\Delta f_D} + 1 \right). \quad (5.19)$$

This function is minimized by maximizing  $\#_{FFT}$ , and minimizing  $\frac{\Delta f_{dec}}{\Delta f_D}$  but there is a restriction on  $\Delta f_{dec}$  such that

$$\Delta f_{dec} \geq \Delta f_D \quad \text{Constraint 3} \quad (5.20)$$

that must be met in order to obtain directional information. Constraint 1 may be written as

$$(\Delta f_{dec} - \Delta f_D) \tau > 1 \quad (5.21)$$

or

$$\Delta f_{dec} > \frac{1}{\tau} + \Delta f_D. \quad (5.22)$$

Thus

$$\min \frac{f_{res}}{\Delta f_D} = \min \frac{2}{\#_{FFT}} \left( \frac{1}{\tau \Delta f_D} + 2 \right). \quad (5.23)$$

Now there is an added restriction on the number of points in the FFT deconvolution  $\#_{FFT}$  such that this number should not exceed the number of points sampled in the burst. If  $\#_{FFT} > N$ , then the FFT is calculated from a data record which contains the  $N$  points of the Doppler burst and a series of trailing zeroes. This leads to an unfortunate deconvolution artifact which manifests itself as a frequency spreading or ‘smearing’ effect. To avoid this requires

$$\#_{FFT} = f_{sample} \tau = 2(\Delta f_D + \Delta f_{dec})\tau = 2(1 + 2\Delta f_D\tau). \quad (5.24)$$

and so

$$\min \frac{f_{res}}{\Delta f_D} = \frac{1}{(1 + 2\Delta f_D\tau)} \left( \frac{1}{\tau \Delta f_D} + 2 \right) = \frac{1}{\tau \Delta f_D}. \quad (5.25)$$

Now for a burst of length 0.1 second, and for Doppler shifts of the order of 100 Hz, this implies that the minimum resolution is 10% of the total frequency shift.

Unfortunately, the above argument show that the FFT is not particularly efficient in determining frequency information in a burst mode of operation, which is obviously necessary when attempting to resolve fluctuating velocities or transient motion. The use of other advanced signal processing algorithms is recommended for establishing the frequency spectrum of short, finite length Doppler bursts (Erk, 1990).

## 5.4 Experimental Results

### 5.4.1 Interface Reflection

The velocity at the upper surface of a moving bed of silica particles was determined by measuring the Doppler shift in the annular shear cell. The transmitting transducer was aligned at  $45^\circ$  from the vertical with its natural focus (about 60 mm from the face of the transducer) situated at the water-bed interface, while the focussed receiver was aligned at a variety of angles, with its focal region arranged to coincide with the bed surface (Figure 5.2). Initially, the intensity of the reflected signal was measured as a function of angle of the receiver, for a range of rotational speeds of the shear cell. It was found that for the low frequency case ( $ka = 1.05$ , Figure 5.7) that the reflection was predominantly specular — that is to say that the maximum intensity of the received signal was found when the angle of incidence equalled the angle of reflection. A further maximum was found for intermediate bed rotational speeds corresponding to a particle velocity of  $0.25 \text{ ms}^{-1}$  — at higher speeds, the bed surface deviated from the horizontal due to centrifugal forces, and was somewhat higher at the outer edge of the annular gap in the shear cell than at the inner edge. At increasing velocities, as the bed surface tilted from the horizontal, so the transmitted wave did not reflect off the bed surface in the same plane as the (directional) focussed receiver, thus reducing the received intensity of the reflected signal. At  $ka = 2.10$ , the reflection changed from specular or directional to diffuse reflection as seen in Figure 5.8. This occurred as the wavelength was significantly smaller than the surface irregularities at the bed interface (which are of the order of the particle radius). Thus there are two distinct frequency regimes for the reflection of an acoustic wave off the packed bed-water interface — the long wavelength regime in which the bed surface appears smooth, and the short wavelength limit,

in which it appears rough. This result is qualitatively similar to results obtained by Kobayashi *et al.* (1991) in their study of the reflection of ultrasonic waves in air off two types of moving surfaces. It was found that for the smooth surface ( $ka \ll 1$ ) the reflection was specular, while for the rough surface ( $ka = 6.6$ ) the reflection was diffuse.

#### 5.4.2 Surface Velocity Measurements

The velocity was determined from the measured Doppler frequency shift. One such frequency spectrum appears in Figure 5.9. There is a distinct intensity peak at the center frequency with a reasonably broad frequency spread, and an appreciable bandwidth. The frequency bandwidth, measured to be the range of frequency over which the intensity is greater than half of its maximum value normalized with respect to the center frequency, is shown in Figure 5.10 as a function of the Doppler frequency shift. This -6 dB bandwidth in most cases was of the order of 20-30% of the total frequency shift. The surface velocity of the particle bed in the shear cell may be calculated from knowledge of the rotational speed of the shear cell  $f$  and the radius  $R$  at which the transmitter and receiver are focussed, namely

$$v_p = 2 \pi R f. \quad (5.26)$$

Due to the fact that the receiving transducer has a finite beam-width which is of the order of 10 mm at the focal length of 60 mm, there will be a velocity gradient in the particles across the measurement volume. This will correspond to a variation in the velocity  $\Delta v_p$  given by

$$\frac{\Delta v_p}{v_p} = \frac{\Delta R_{meas}}{R} \quad (5.27)$$

which will be of the order of 6-7% for a radius of 150 mm, and will be independent of particle velocity. Furthermore due to the finite beam-width, the angles  $\theta_T$

and  $\theta_R$  should not be regarded as single valued but should be considered as  $\theta_T \pm \Delta\theta_T$  and  $\theta_R \pm \Delta\theta_R$ . Substituting in the nominal values of  $45^\circ \pm 10^\circ$  and  $90^\circ \pm 10^\circ$ , the function  $\cos\theta_T + \cos\theta_R$  varies between 0.400 and 0.992, with the nominal center value of 0.707. Assuming a linear decrease in intensity of the backscattered signal as a function of angular deviation from the nominally stated orientation, this would lead to an approximately 30% -6 dB frequency bandwidth. The measured frequency bandwidth is seen to be of the same order and is independent of velocity, as would be expected from the above reasoning. The spectral broadening is thus assumed to be the result of the finite volume of the measurement cell, the velocity distribution across the cell, and the angular spreading of the receiving and transmitting transducer beams. The observed signal to noise ratio (SNR) was high (as can be seen from the frequency spectra) and typically in the range of 40 to 100 dB.

#### 5.4.3 Scattering and Interior Velocity Measurements

By moving the transmitting and receiving transducers together in a vertical plane, measurements of the particle velocity below the water-packed bed interface were taken. The velocity profile and the frequency bandwidth are shown as a function of depth of penetration into the mixture in Figure 5.11 — both the measured velocity and the bandwidth are seen to be reasonably constant with depth. The velocity measurement at depth is subject to some geometrical uncertainty due to the refraction of the acoustic beams discussed in Section 5.2.1. The path length for a transmitter angle of  $45^\circ$  and a receiver oriented at  $90^\circ$  to the bed interface is about 47 mm for a nominal target depth below the interface of 25 mm (the unrefracted path length would be about 60 mm). This path length should be taken into account in calculating the expected beam attenuation. A polar diagram of the scattered intensity as a function of the receiver orientation

was obtained with the transmitter aligned at  $45^\circ$  to the normal (Figure 5.12), and this shows that the preferred angle at which the maximum scattered intensity is measured is the  $90^\circ$  position, i.e. the angle between the incident and the maximum scattering direction is  $45^\circ$ . In addition, this maximum is evident for  $ka \sim 1 - 3$ . This result, which shows that the interaction of the incident sound and the particles at depth is indeed one of scattering as opposed to the mechanism of reflection seen at the bed surface, bears striking similarity to the results of Böstrom (1980) who showed that the maximum intensity in the signal scattered off a single particle for  $ka = 1$  occurs at an angle of about  $45^\circ$  from the incident. This angle corresponds exactly with the maximum seen at the  $90^\circ$  receiver position in the velocimeter geometry.

## 5.5 Discussion

There is a distinct change in mechanism between reflection at the water/sediment surface and scattering from particles at depth in the packed bed. However, in both cases the velocity of the moving particles may be accurately measured from the Doppler frequency shift. In the case of the measurement at depth, the maximum backscattered intensity for  $ka \sim O(1)$  occurs at an angle of about  $45^\circ$  from the incident, and this coincides exactly with the prediction of scattering from a single mobile elastic particle. The frequency spectra, which are similar for both the surface reflection and the internal scattering cases, show significant spectral broadening which is fully accounted for by the finite beam geometry of the transmitter and receiver. (In contrast, the Doppler spectra obtained in the sedimenting bed (Figure 5.5) have significantly smaller bandwidths due to the fact that there was not an appreciable velocity gradient across the measuring volume in this case). The use of very sharply focussed transducers

would reduce the frequency bandwidth somewhat, but this effect must also be seen as an artifact of the particular rotational setup studied. In the case of a flowing two phase mixture in a horizontal pipe, for example, the spatial velocity gradients will not be as severe as those encountered in the Dynamic Shear Cell, and so the spectral bandwidth will not be as large.

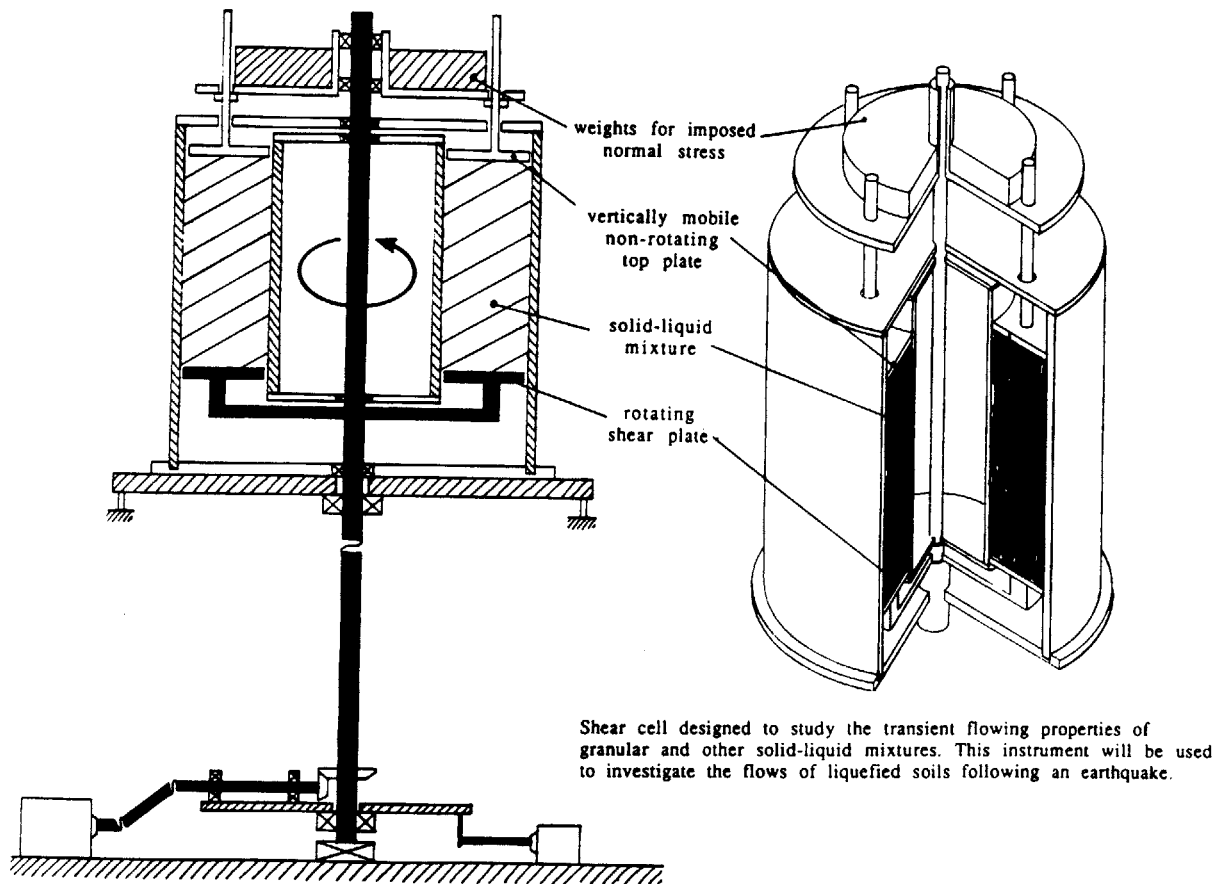


**Figure 5.1:** Dynamic Shear Cell (Poutiatine, 1990) designed to study steady and oscillatory motion of highly concentrated solid-liquid mixtures. Particle velocities in this annular shear cell were measured using the ultrasonic Doppler velocimeter detailed in Chapter 5. The cell was typically operated with a depth of about 40 mm of 1.0 mm silica beads submerged in water.

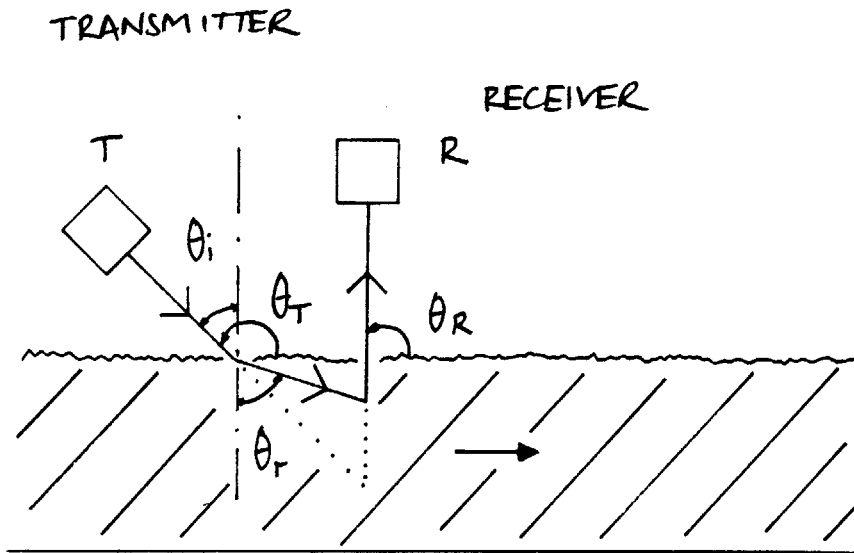


**Figure 5.2:** Geometrical acoustics for refraction at an interface between two media of dissimilar acoustic indices of refraction, showing Snell's Law, and the geometry of the ultrasonic Doppler velocimeter. The transmitter and receiver could be moved together in the same vertical plane to allow subsurface as well as surface velocity measurements to be made.

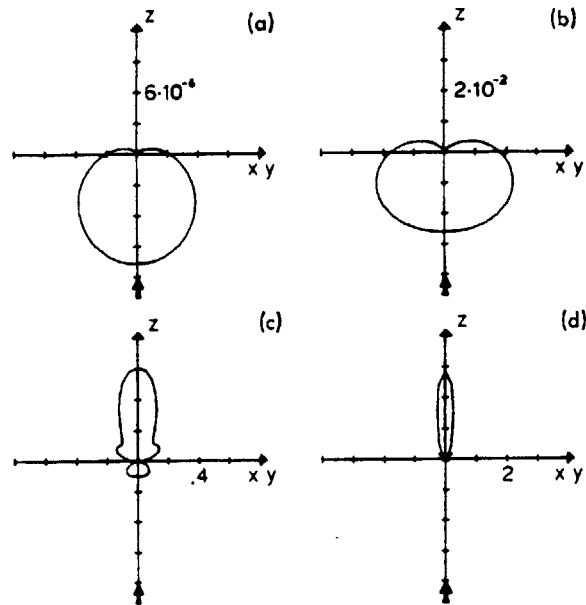
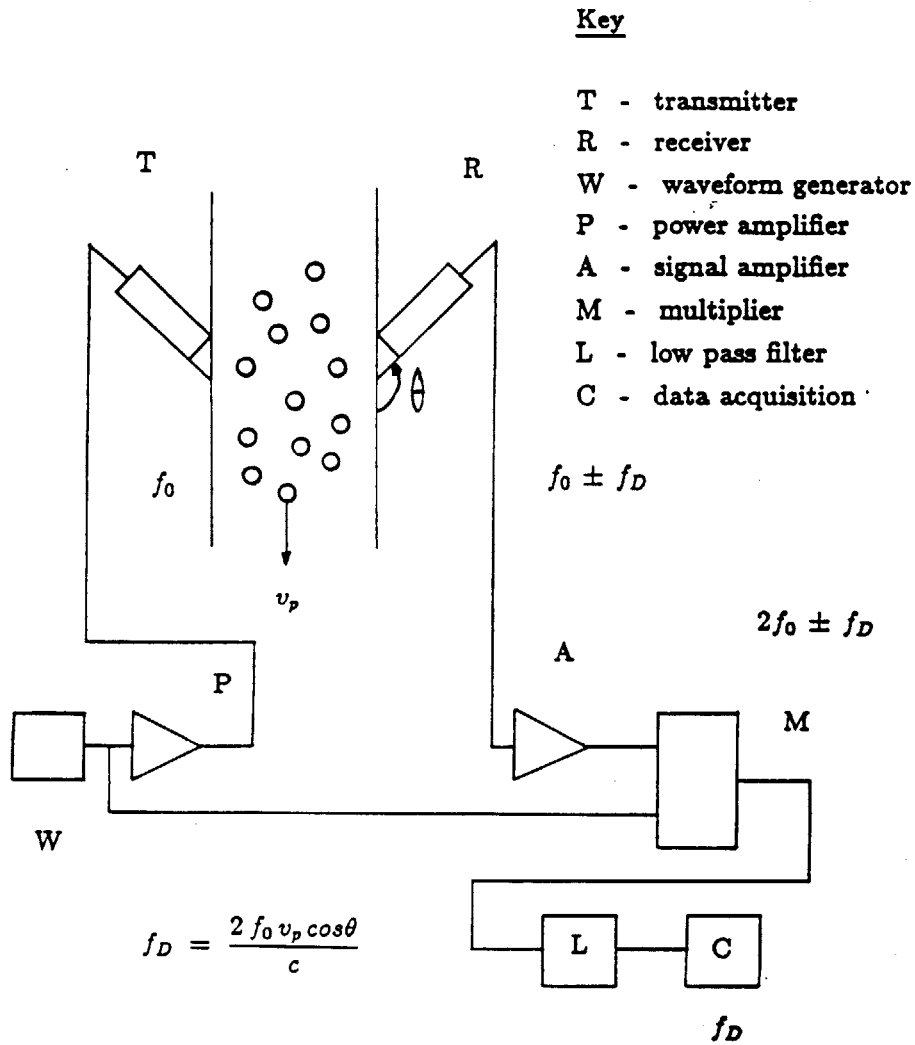
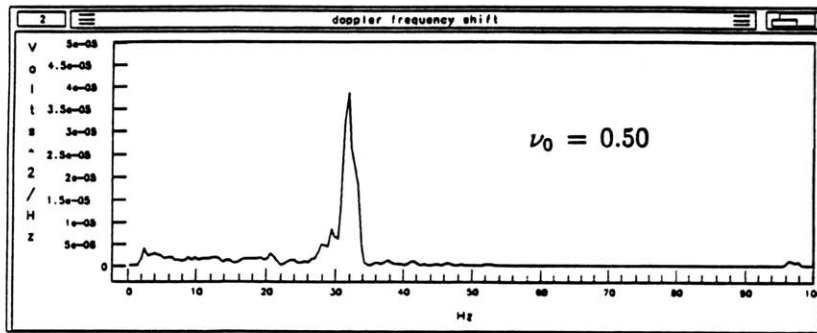
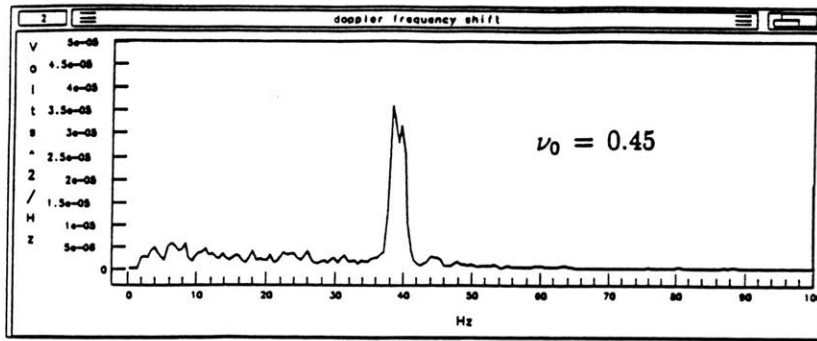


FIG. 4. The differential scattering cross section for a sphere for four different values of  $ka$ : (a)  $ka=0.1$ , (b)  $ka=1$ , (c)  $ka=3$ , (d)  $ka=8$ .

**Figure 5.3:** Scattering behavior of a single mobile elastic particle in a standing acoustical wave. These polar diagrams of the total intensity of the scattered wave as a function of  $ka$  for an aluminum sphere in water are from Böstrom (1980).



**Figure 5.4:** Schematic of the prototype ultrasonic Doppler velocimeter. The scattered signal is measured at an angle  $\theta$  to the incident beam and it is demodulated electronically with a double balance mixer to determine the Doppler shift.



**Figure 5.5:** Typical spectra of the demodulated scattered signal showing distinct peaks corresponding to the Doppler shift caused by particles sedimenting at concentrations up to 50% by volume. These spectra have a small bandwidth due to the fact that there is not an appreciable velocity gradient across the measurement volume.

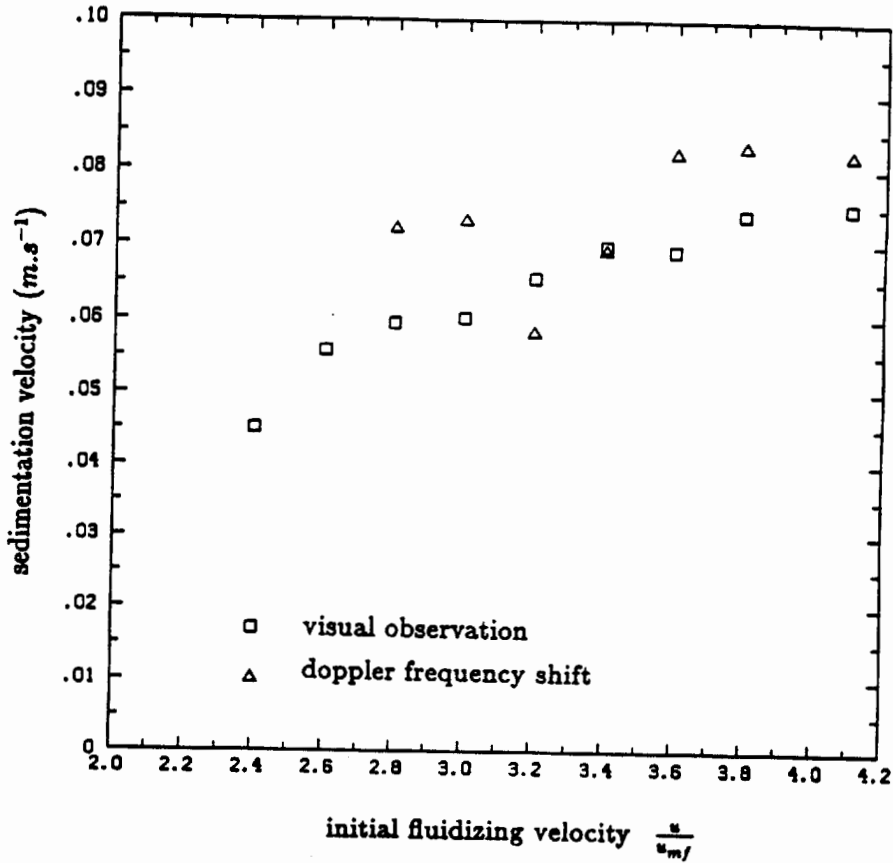


**Figure 5.6** Comparison of particle velocities measured visually and using the ultrasonic Doppler technique. The data show some scatter due to error in the visual technique and the short duration of the tone bursts that were used in the ultrasonic method. Longer time records would introduce averaging, and the statistics of velocity fluctuations could also be derived from these.

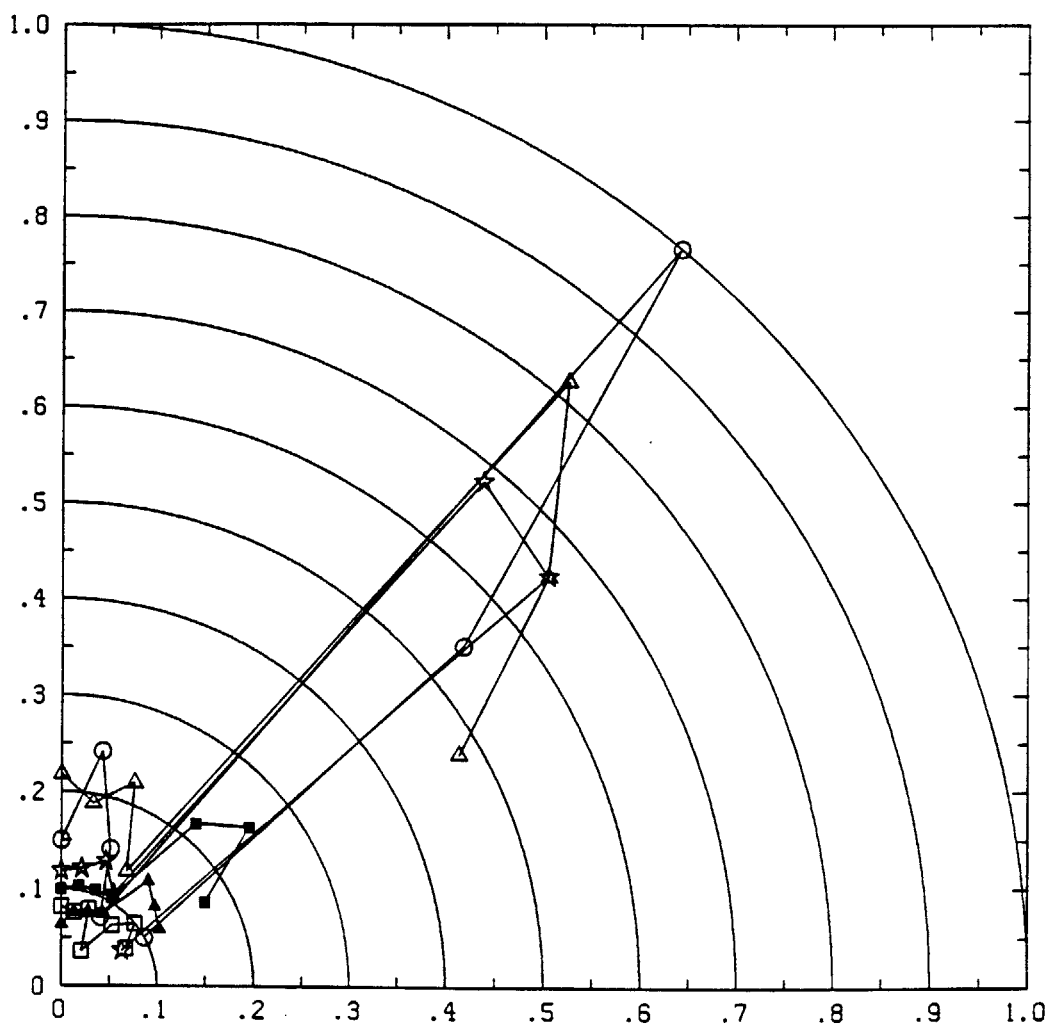


**Figure 5.7** Intensity of the wave reflected off the moving interface between clear water and the sedimented packed bed as a function of angle of the receiver from the vertical. The transmitter, operating at  $ka = 1.05$ , is aligned at  $45^\circ$  from the vertical in the left-hand quadrant. The reflection is seen to be essentially specular for the range of particle velocities considered.

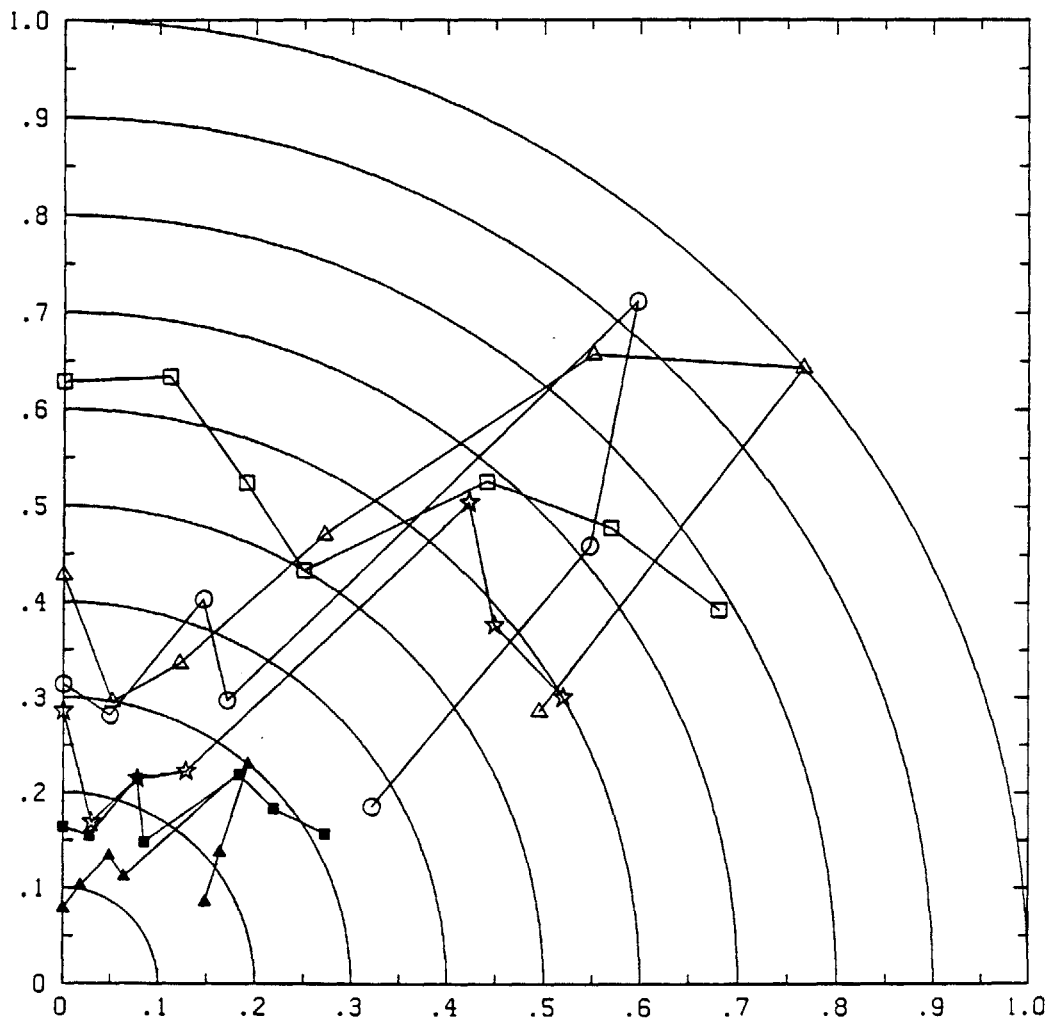


**Figure 5.8** Intensity of the reflected wave as in Figure 5.7 for the case  $ka = 2.10$ . The reflection can be seen to be essentially diffuse, as the wavelength is somewhat smaller than the surface features of the interface.

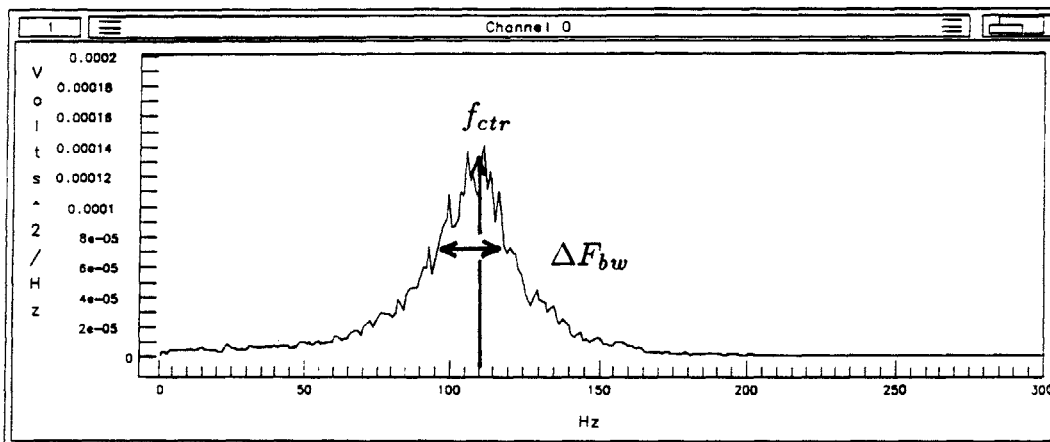


**Figure 5.9** Doppler frequency spectrum measured at the moving surface of the water/packed bed interface. The spectrum shows a distinct intensity peak at the center frequency  $f_{ctr}$  with a reasonably broad frequency bandwidth  $\Delta F_{bw}$ .

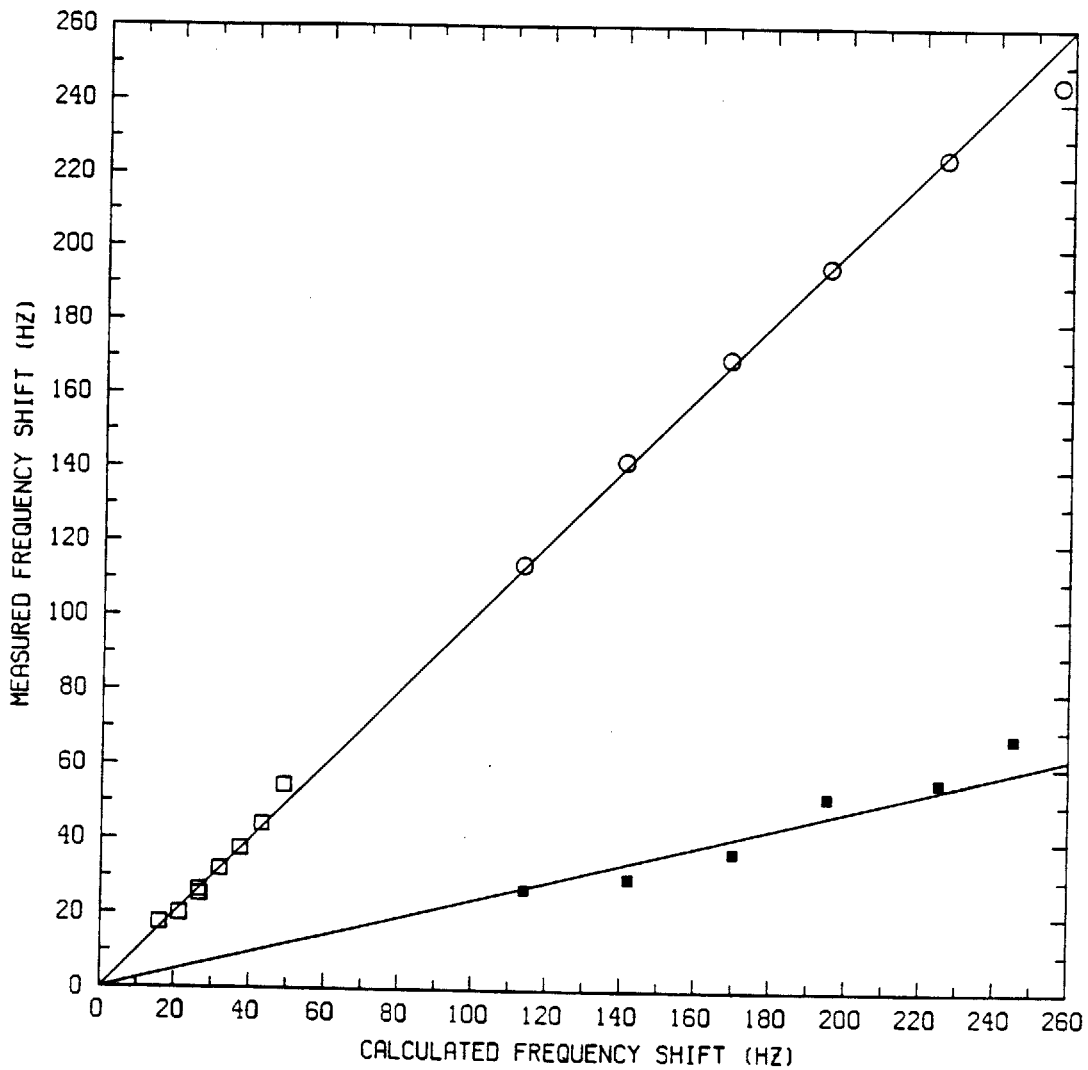


**Figure 5.10** Surface velocity measurements. The measured Doppler frequency shift is plotted against the shift calculated from the actual particle velocity. The frequency bandwidth (the lower data points) is shown as a function of the calculated frequency shift.

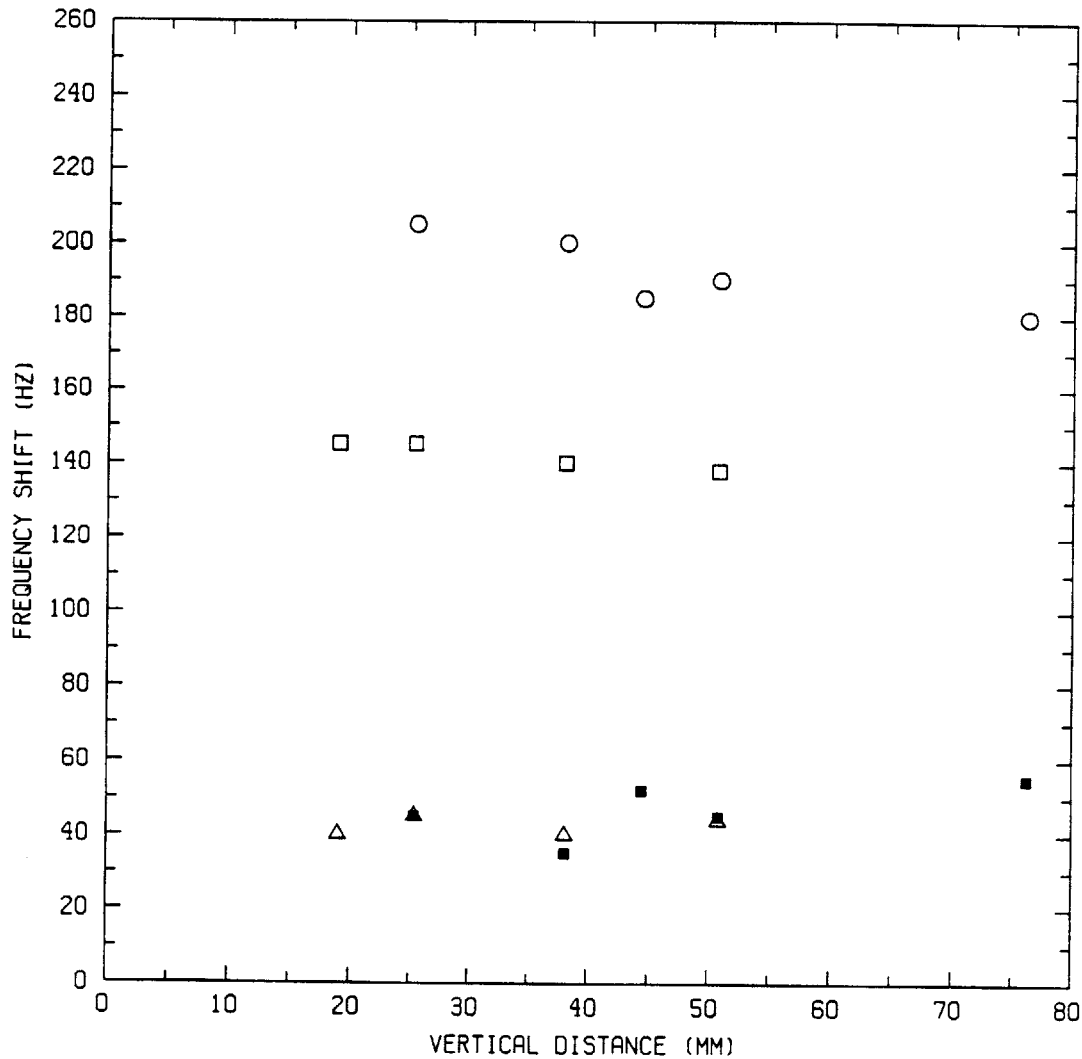


**Figure 5.11** Velocity profile (as represented by the frequency shift) and fractional bandwidth (the -6 dB bandwidth as a fraction of the center frequency of the Doppler shift) as a function of depth of penetration of the focal regions of the transmitter and receiver into the rotating packed mixture (in mm, the bed/water interface is at 40 mm and the bottom of the silica particle bed is at 0 mm). The velocity profile can be seen to be quite invariant with depth into the mixture. The frequency bandwidth is given by the lower points ( $\Delta$  ■).

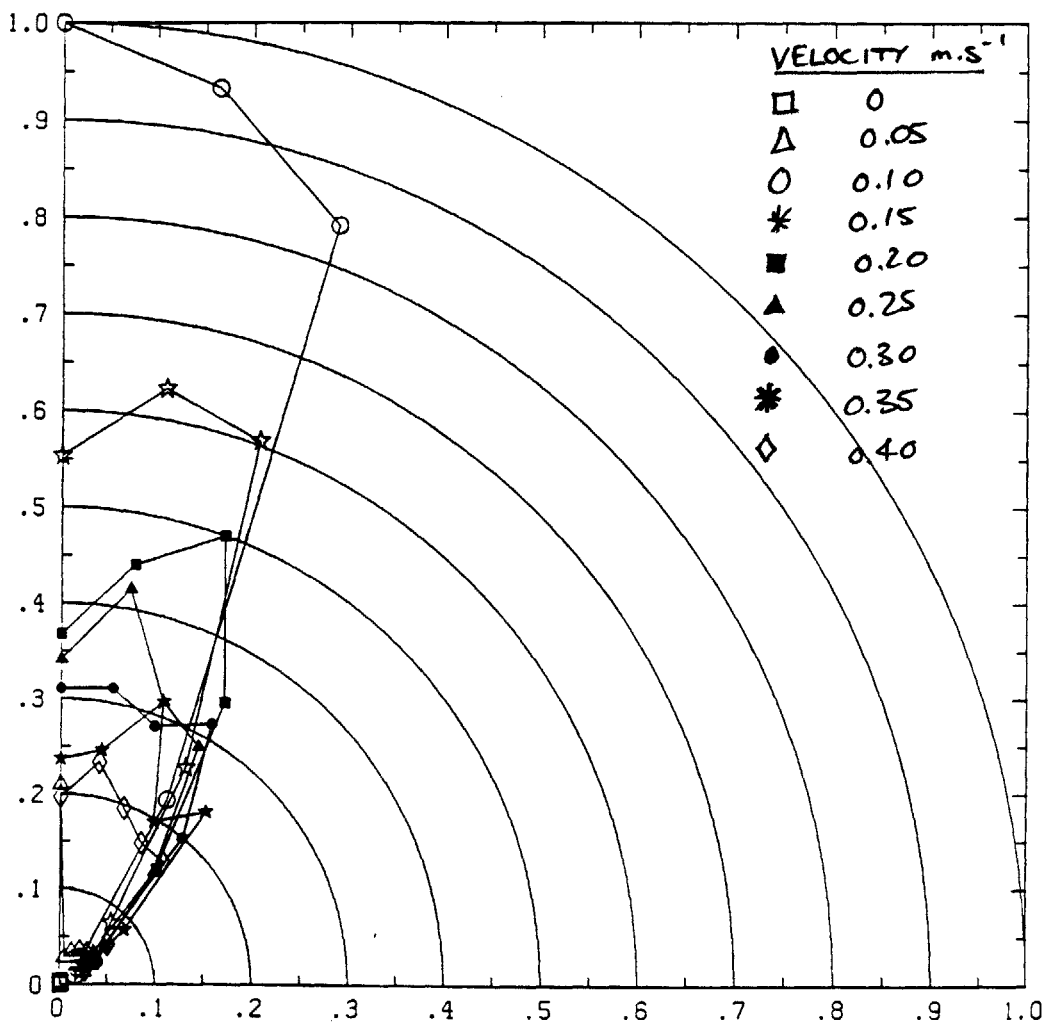


**Figure 5.12** Polar diagram of the scattered intensity as a function of angle of the receiver for sound scattered from a depth of 25 mm below the surface of a sedimented bed of 1 mm silica particles in water. The transmitter is positioned at  $45^\circ$  from the vertical in the left-hand quadrant. The preferred angle of scattering is approximately the vertical which shows good agreement with the prediction of Böstrom (1980) in Figure 5.3.

## CHAPTER 6

### CONCLUSIONS

Acoustic wave propagation in highly concentrated suspensions of elastic solid particles in Newtonian fluids has been considered from both an experimental and an analytical point of view. The motivation for this work has been the development of non-intrusive instrumentation for highly concentrated multiphase flows. The major findings of this study are summarized below.

For acoustic wave propagation in solid-liquid mixtures at wavelengths larger than the particle radius, that is to say for  $ka < 1$ , the single phase classical Rayleigh theory (O'Neil, 1949) describing the acoustic field intensity produced by an oscillating transducer has been shown to accurately predict the geometrical beam characteristics of non-focussed circular disc transducers. The substitution of a modified complex wavenumber, which takes into account the attenuation behavior of the medium, allows the beam geometry of a disc transducer in an arbitrary attenuating medium to be predicted. This is of importance, for example, in evaluating the performance of an instrument that determines the concentration of the dispersed phase in a two phase mixture by measuring the attenuation of sound in the medium. Beam geometry effects, which are strongly influenced by the medium sound speed and frequency of operation, are not typically considered in non-intrusive acoustic instrumentation, but have been shown in this study to be important in some cases. Typically, for acoustic wave propagation in a highly concentrated mixture of 1.0 mm silica particles in water, the focal region for focussed transducers is of the order of 10 particle diameters on each side. In the same mixture due to attenuation, the intensity decreases by a factor of  $1/e$  in a distance of approximately 500 particle diameters and this results in a useful range of penetration of tens of centimeters.

The attenuation of sound in both packed and fluidized beds of spherical particles has been shown experimentally and analytically in this study to be dominated by viscous effects for frequencies such that  $ka < 1$  and for high dynamic particle Reynolds number  $R$ . Moreover, for the high  $R$  regime, the attenuation has been shown both experimentally and analytically to vary with  $(ka)^{3/4}$ . The frequency dependence of the Biot model (Biot, 1956) most widely used in predicting attenuation in porous media is  $(ka)^{1/2}$ , but experimental results have shown a somewhat greater functional dependence than this (Salin and Schön, 1981). For low  $R$  or below about 25 Hz for 1 mm silica beads in water, the attenuation is predicted to exhibit a  $\frac{3}{2}$  power dependence on frequency.

The present study confirms previous experimental results for attenuation in porous media, and provides new data for the fluidized case, as a function of solids' concentration. For  $ka > 1$ , highly non-linear attenuation occurs — this is presumed to be due to multiple scattering effects not considered in this study.

A comprehensive theory for viscous attenuation in solid-liquid mixtures, including viscous, inertial and history effects between the phases, has been proposed and has been shown to predict accurately sound speed and attenuation as a function of particle and fluid properties, and both frequency and solids' fraction. Through a perturbation analysis of the continuity and momentum equations for the two phases, the complex wavenumber  $\mathbf{k}$  has been shown to depend on the unsteady particle Reynolds number,  $R$  (related to the thickness of the unsteady viscous boundary layer surrounding each particle), the particle added mass coefficient, the dispersed phase concentration and the frequency of excitation. The dissipation around an oscillating particle in an incident sound wave has been shown to be dominated by Basset or history forces at high frequencies.

The sound speed of a compressional wave in a highly concentrated solid-

liquid mixture has been shown to be a weak function of  $ka$ , and it has been shown that the sonic velocity may in some cases (for  $ka \rightarrow 0$ ) be a non-monotonic function of particle concentration. For  $ka \sim 1$  the speed of sound in a mixture of silica beads and water increases monotonically with the dispersed phase concentration. For three to four orders of magnitude in  $ka$ , the sound speed variation is of the order of 5-10%.

In addition, for  $ka \sim 1$  the attenuation has been shown to be a non-monotonic function of concentration, with a maximum occurring at intermediate solids' fractions. This, along with the frequency dependence of attenuation, has important implications for the use of ultrasonic instrumentation in concentrated suspensions as prohibitively low penetration can occur at high frequencies and intermediate concentrations. It has been shown that there exists a compromise between maximizing  $ka$  with respect to the physical dimensions of the system being interrogated for better spatial resolution of the measurement technique, and minimizing  $ka$  for better beam penetration into the mixture.

The theory developed in this study to model viscous attenuation losses in the propagation of an infinitesimal pressure perturbation through a two phase mixture has been modified to predict the dynamic permeability associated with the flow of a fluid through a porous medium of spheres under the influence of an infinitesimal oscillatory pressure perturbation. It has been previously postulated that the variation of dynamic permeability with frequency of oscillation of the flow would provide valuable insights into the pore geometry of such media (Johnson *et al.*, 1987) — indeed the model developed here shows that the permeability is a function of the mean hydraulic radius of the interstitial pores of the medium, as well as the added mass coefficient of the particles, both of which are strong functions of the microstructure of the mixture.

The application of ultrasonic instrumentation to the measurement of dispersed phase velocity in highly concentrated suspensions has been shown in the use of an ultrasonic Doppler velocimeter for the measurement of sedimentation velocities in the hindered settling regime, and in measuring surface and interior velocities in a packed mixture in a Dynamic Shear Cell. Particle velocities have been measured accurately at up to the maximum packing concentration, although the finite beam width of the transducers used and the velocity profiles in the latter system are shown to adversely affect the frequency bandwidth. The accuracy of the measurement of the velocities of particles in unsteady motion has been shown to be governed by the length of the Doppler burst  $\tau$  and the magnitude of the Doppler shift  $\Delta f_D$ , and the minimum resolution of the measurement is limited to  $\frac{1}{\tau \Delta f_D}$ . In the case of laser Doppler velocimetry this is less of a restriction, as the Doppler shifts measured can be of the order of megahertz. For ultrasonic Doppler measurements in contrast, with a Doppler shift of say 100 Hz and a required temporal resolution of 0.1 seconds, the best resolution possible is 10% of the total frequency shift.

It has been shown, however, that for the case of steady particle velocities at least, accurate measurements of dispersed phase velocity are quite feasible in highly concentrated solid-liquid particulate mixtures at up to the maximum packing concentration.

## APPENDIX

**Figure 1** Steady Velocity Measurements In the Dynamic Shear Cell.

**Figure 2** Unsteady Velocity Measurements In the Dynamic Shear Cell.

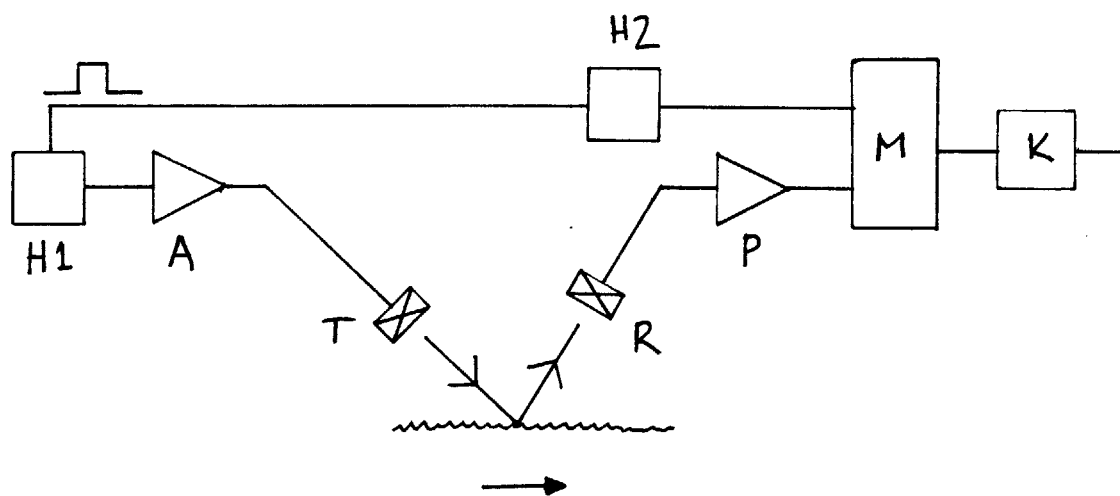
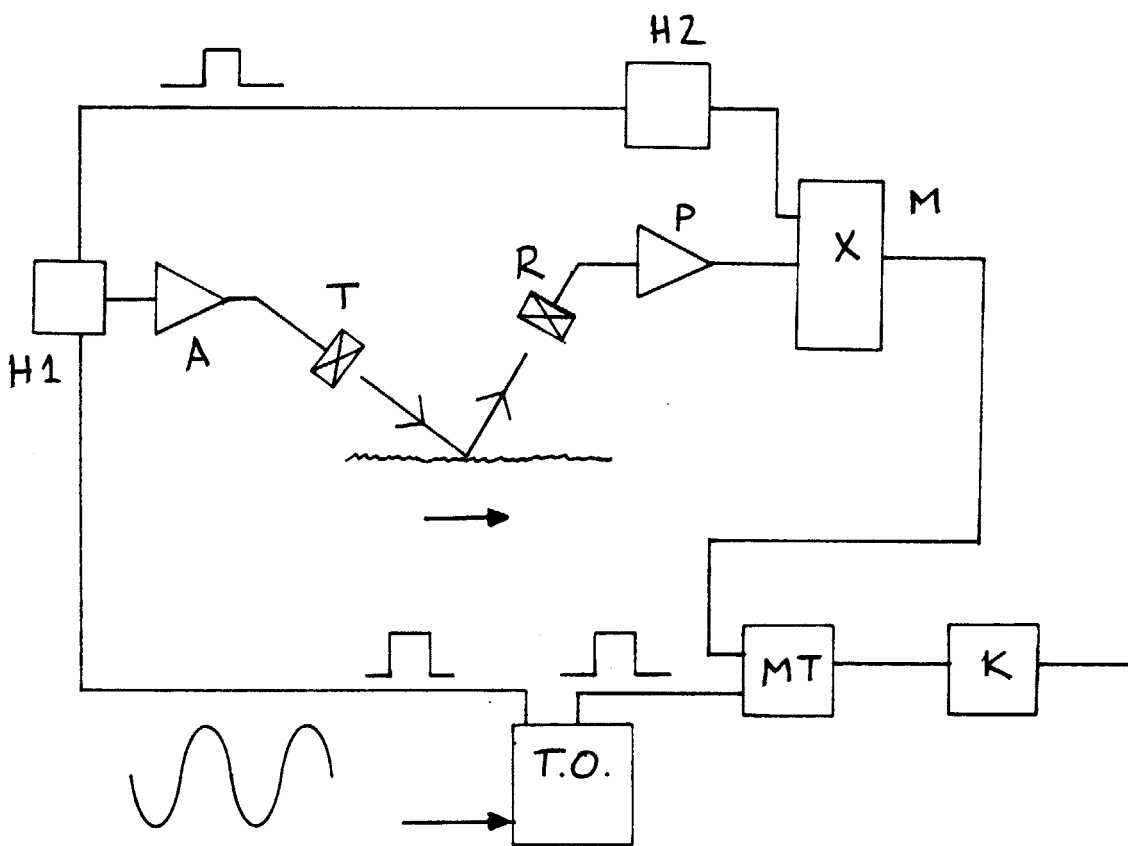


Figure 1 Steady Velocity Measurements In the Dynamic Shear Cell.

**Figure 1** Steady Velocity Measurements In the Dynamic Shear Cell.

A tone burst of frequency  $f_0$  and several waveforms in duration generated by the Hewlett-Packard 3314A Function Generator (H1) and amplified by the Amplifier Research RF Amplifier (A), is transmitted by the transmitter (T). The signal from the receiver (R) at a frequency  $f_0 \pm \Delta f_D$  is amplified by the Panametrics 5055PR receiver (P). The first function generator triggers a second identical unit (H2) which operates at some small frequency shift from the original, namely  $f_0 - \Delta f_{dec}$ . This offset frequency is multiplied by the received signal in a double balanced mixer (M) and the resultant signal is low pass filtered (K). The final signal has the frequency  $\Delta f_{dec} + |\Delta f_D|$  if the velocity of the particles is towards the transmitter and  $\Delta f_{dec} - |\Delta f_D|$  if the velocity is away from the transmitter.



**Figure 2** Unsteady Velocity Measurements In the Dynamic Shear Cell.

## Figure 2 Unsteady Velocity Measurements In the Dynamic Shear Cell.

The Hewlett-Packard 3314A Function Generator (H1) is triggered by a rotational position measurement from the oscillating bottom plate of the Dynamic Shear Cell. The rotational transducer output is used to trigger a Tektronix 465B oscilloscope, which has two TTL outputs. The first (Gate A) is used to trigger H1. It in turn generates a tone burst of frequency  $f_0$  and several waveforms in duration, which in turn is amplified by the Amplifier Research RF Amplifier (A). The signal from the receiver (R) at a frequency  $f_0 \pm \Delta f_D$  is amplified by the Panametrics 5055PR receiver (P). The first function generator triggers a second identical unit (H2) which operates at some small frequency shift from the original, namely  $f_0 - \Delta f_{dec}$ . This offset frequency is multiplied by the received signal in a double balanced mixer (M). The Tektronix Oscilloscope (TO) has a second, delayed TTL output (Gate B), which is used to operate a Matec RF Switch (MT). The RF switch is used to gate the received output to ensure that only information from the desired portion of the oscillatory cycle of the rotation of the shear cell is analyzed. The resultant signal is then low pass filtered (K). The final signal has the frequency  $\Delta f_{dec} + |\Delta f_D|$  if the velocity of the particles is towards the transmitter and  $\Delta f_{dec} - |\Delta f_D|$  if the velocity is away from the transmitter, as in the steady case. Sampling and frequency selection considerations are given in Section 5.3.3.

## REFERENCES

- Adach, J. and R. Chivers, 1990, "A detailed investigation of effective geometrical parameters for weakly focussed ultrasonic transducers. Part I: Optimisation of experimental procedures", *Acustica*, Vol. 70, pp. 12-22.
- Adach, J. and R. Chivers, 1990, "A detailed investigation of effective geometrical parameters for weakly focussed ultrasonic transducers. Part II: A systematic study including an absorbing medium", *Acustica*, Vol. 70, pp. 135-145.
- Aindow, J., A. Markiewicz and R. Chivers, 1985, "Quantitative investigation of disk ultrasonic sources", *J. Acoust. Soc. Am.*, Vol. 78, pp. 1519-1529.
- Allegra, J.R., and S. A. Hawley, 1972, "Attenuation of sound in suspensions and emulsions: Theory and Experiments", *J. Acoust. Soc. Am.*, Vol. 51, pp. 1545-1564.
- Anson, L., and R. Chivers, 1989, "Ultrasonic propagation in suspensions — a comparison of a multiple scattering and an effective medium approach", *J. Acoust. Soc. Am.*, Vol. 85, No. 2, pp. 535-540.
- Attenborough, K., 1983, "Acoustical characteristics of rigid fibrous absorbents and granular materials", *J. Acoust. Soc. Am.*, Vol. 73, pp. 785-799.
- Beltran, N., C. Haindl, and E. Taylor, 1989, "Design of low cost instrumentation to measure flow and concentration of a copper metallurgical slurry", *IEEE Trans. Instr. and Meas.*, Vol. 38, No. 6, pp. 1127-1131.
- Biot, M., 1956, "Theory of propagation of elastic waves in a fluid saturated porous solid. II: Higher Frequency range", *J. Acoust. Soc. Am.*, Vol. 28, pp. 179-191.
- Böstrom, A., 1980, "Scattering of stationary acoustic waves by an elastic obstacle immersed in a fluid", *J. Acoust. Soc. Am.*, Vol. 67, pp. 390-398.
- Burridge, R., and J. B. Keller, 1981, "Poroelasticity equations derived from microstructure", *J. Acoust. Soc. Am.*, Vol. 70, pp. 1140-1146.
- Charlaix, E., A. P. Kushnick, and J. P. Stokes, 1988, "Experimental study of dynamic permeability in porous media", *Physical Review Letters*, Vol. 61, pp. 1595-1598.
- Chivers, R., and J. Aindow, 1983, "Ultrasonic propagation studies in suspension systems", *J. Phys. D.: Appl. Phys.*, Vol. 16, pp. 2093-2102.
- Colwell, J., C. Shook, R. Gillies and M. Small, 1988, "Ultrasonic flowmeter tests with slurries", *Journal of Pipelines*, Vol. 7, pp. 127-140.
- Del Grosso, V., and C. Mader, 1972, "Speed of sound in pure water", *J. Acoust. Soc. Am.*, Vol. 52, pp. 1442-1446.

- Drew, D., 1983, "Mathematical modelling of two-phase flow", *Ann. Rev. Fluid Mech.*, Vol. 15, p. 261.
- Erk, P., 1990, "Digital Signal Processing Methods in Laser Doppler Anemometry", MSME Thesis, Massachusetts Institute of Technology.
- Foscolo, P., and L. Gibilaro, 1985, "Fluid dynamic stability of fluidised suspensions: the particle bed model", *Chem. Eng. Sci.*, Vol. 42, pp. 1489-1500.
- Gibson, R. L., and M. Toksöz, 1989, "Viscous attenuation of acoustic waves in suspensions", *J. Acoust. Soc. Am.*, Vol. 85, pp. 1925-1934.
- Goldstein, R. J., 1983, *Fluid Mechanics Measurements*, Hemisphere Publishing Co., New York.
- Goodsitt, M., E. Madsen and J. Zagzebski, 1982, "Field patterns of pulsed focussed radiators in attenuating and nonattenuating media", *J. Acoust. Soc. Am.*, Vol. 71, pp. 318-329.
- Hampton, L., 1967, "Acoustic properties of sediments", *J. Acoust. Soc. Am.*, Vol. 42, pp. 882-890.
- Happel, J., 1958, "Viscous flow in multiparticle systems: slow motion of fluids relative to beds of spherical particles", *AIChE J.*, Vol. 4, pp. 197-201.
- Harker, A., and J. Temple, 1988, "Velocity and attenuation of ultrasound in suspensions of particles in fluids", *J. Phys. D.: Appl. Phys.*, Vol. 21, pp. 1576-1588.
- Harris, G., 1981, "Review of transient theory for a baffled planar piston", *J. Acoust. Soc. Am.*, Vol. 70, pp. 10-20.
- Hilgert, W., and H. Hofmann, 1986, "Characterization of gas phase flow in bubble columns at low superficial gas velocities with the aid of the ultrasonic Doppler technique", *Ger. Chem. Eng.*, Vol. 9, pp. 180-190.
- Hsu, F., R. Turian, and T. Ma, 1989, "Flow of non-colloidal slurries in pipelines", *A.I.Ch.E. Jour.*, Vol. 35, pp. 429-442.
- Jenkins, F. and H. White, 1957, *Fundamentals of Optics*, McGraw-Hill, New York.
- Johnson, D. L., T. J. Plona, C. Scala, F. Pasierb and H. Kojima, 1982, "Tortuosity and acoustic slow waves", *Physical Review Letters*, Vol. 49, pp. 1840-1844.
- Johnson, D. L., K. Koplik and R. Dashen, 1987, "Theory of dynamic permeability and tortuosity in fluid-saturated porous media", *J. Fluid Mechanics*, Vol. 176, pp. 379-402.
- Joy, R., 1984, "Ultrasonic vortex flowmeters", *Proc. 30th. International Instrumentation Symp.*, ISA, pp. 219-230.

- Kadambi, J., S. Bhunia and A. Dybbs, 1988, "A refractive index matched test facility for solid-liquid flow studies using laser velocimetry", *Third International Symposium on Liquid-Solid Flows*, M.C. Roco, ed., ASME, New York, pp. 91-99.
- Karplus, H., and A. Raptis, 1979, "Investigation leading to the development of an acoustic Doppler slurry flowmeter", Argonne National Laboratory, IL.
- Kobayashi, H., T. Kimura and M. Negishi, 1991, "A study of a vehicle ground speed sensor using the ultrasonic wave doppler effect", *J. Acoust. Soc. Am.*, Vol. 89, No. 1, pp. 191-195.
- Kuster, G., and M. Toksöz, 1986, "Velocity and attenuation of seismic waves in two phase media: Part II. Experimental results", *Geophysics*, Vol. 39, pp. 607-618.
- Landau L.D., and E. M. Lifshitz, 1959, *Fluid Mechanics*, Pergamon Press.
- Lynnworth, L., 1989, *Ultrasonic Measurements for Process Control: Theory, Techniques, Applications*, Academic Press, San Diego, CA.
- Machado, J., R. Sigelmann, and A. Ishimaru, 1983, "Acoustic wave propagation in randomly distributed spherical particles", *J. Acoust. Soc. Am.*, Vol. 74, No. 5, pp. 1529-1534.
- Marcus, M., H. Schelbert, D. Skorton and G. Wolf, (eds.), 1991, *Cardiac Imaging*, Saunders Co., Philadelphia.
- Maxwell, J. C., 1881, *A Treatise on Electricity and Magnetism*, 2nd. ed., Clarendon Press, Oxford.
- McLeod, F., 1967, "A directional Doppler flowmeter", *Int. Conf. Med. Biol. Eng.*, Stockholm, p. 213.
- Morse, P., and K. Ingard, 1978, *Theoretical Acoustics*, McGraw-Hill, New York.
- O'Neil, H., 1949, "Theory of focussing radiators", *J. Acoust. Soc. Am.*, Vol. 21, pp. 516-526.
- Ong, K., and M. Beck, 1975, "Slurry flow velocity, concentration and particle size measurement using flow noise and correlation techniques", *Measurement and Control*, Vol. 8, pp. 453-463.
- Onoda, G. Y., and E. Liniger, 1990, "Random loose packings of uniform spheres and the dilatancy onset", *Physical Review Letters*, Vol. 64, pp. 2727-2730.
- Penner, S., C. Wang and M. Bahadori, 1984, "Nonintrusive diagnostic techniques for measurements on coal-combustion systems", *Prog. Energy Combust. Sci.*, Vol. 10, pp. 209-212.
- Plona, T.J., 1980, "Observation of a second bulk compressional wave in a porous medium at ultrasonic frequencies", *Appl. Phys. Lett.*, Vol. 36, pp. 259-261.

- Poutiatine, A. I., 1990, "Dynamic shear cell for transient liquefaction and solidification of highly concentrated two-phase flows", MSME Thesis, Massachusetts Institute of Technology.
- Probstein, R. F., 1989, *Physicochemical Hydrodynamics*, Butterworths, Boston.
- Raptis, A., and T. Lau, 1981, "State-of-the-art acoustic instrumentation for coal-conversion plants", Argonne National Laboratory, Argonne IL.
- Raptis, A., 1984, "Acoustic instrumentation", *Prog. Energy Combust. Sci.*, Vol. 10, pp. 213-227.
- Ricker, N., and F. Forster, 1985, "Pulse Doppler ultrasonic velocity measurement in aqueous pulp fiber suspensions", *TAPPI Journal*, Vol. 68, pp. 79-82.
- Salin, D., and W. Schön, 1981, "Acoustics of water saturated packed glass spheres", *J. Physique - Lettres*, Vol. 42, p. L477-L480.
- Sheng, P., and M. Zhou, 1988, "Dynamic permeability in porous media", *Physical Review Letters*, Vol. 61, pp. 1591-1594.
- Shook, C., R. Gillies, D. Haas, W. Husband and M. Small, 1982, "Flow of coarse and fine slurries in pipelines", *J. Pipelines*, Vol. 3, pp. 13-21.
- Temkin, S., 1981, *Elements of Acoustics*, John Wiley & Sons, New York.
- Turner, J. C. R., 1976, "Two-phase conductivity: the electrical conductance of liquid-fluidized beds of spheres", *Chem. Eng. Sci.*, Vol. 31, p 487.
- Twersky, V., 1978, "Acoustic bulk parameters in distributions of pair-correlated scatterers", *J. Acoust. Soc. Am.*, Vol. 64, pp. 1710-1714.
- Urick, R.J., 1947, "A sound velocity method for determining the compressibility of finely divided substances", *J. Acoust. Soc. Am.*, Vol. 18, pp. 983-987.
- Urick, R.J., 1948, "The absorption of sound in suspensions of irregular particles", *J. Acoust. Soc. Am.*, Vol. 20, pp. 283-289.
- Wallis, G. B., 1989, "Inertial coupling in two-phase flow: macroscopic properties of suspensions in an inviscid fluid", *Multiphase Science and Technology*, Vol. 5, p. 274.
- Waterman, P., 1969, "New foundations of acoustic scattering", *J. Acoust. Soc. Am.*, Vol. 45, pp. 1417-1429.
- Waterman, P., and R. Truell, 1961, "Multiple scattering of waves", *J. Math. Phys.*, Vol. 2, pp. 512-540.
- Zhou, M., and Sheng, P., 1989, "First principles calculations of dynamic permeability in porous media", *Physical Review B*, Vol. 39, No. 16, pp. 12027-12039.